Study of Nanocrystal Formation in Finemet Metallic Glasses and Their Magnetic Properties

By

SIBA PADA MONDAL
Roll No: 0755502
Session: January - 2007

A THESIS SUBMITTED TO THE DEPARTMENT OF PHYSICS,
KHULNA UNIVERSITY OF ENGINEERING & TECHNOLOGY, KHULNA-9203
IN PARTIAL FULFILLMENT OF THE REQUIREMENT FOR THE DEGREE OF
MASTER OF PHILOSOPHY

DEPARTMENT OF PHYSICS
KHULNA UNIVERSITY OF ENGINEERING & TECHNOLOGY
KHULNA-9203, BANGLADESH
NOVEMBER-2008

KHULNA UNIVERSITY OF ENGINEERING & TECHNOLOGY
DEPARTMENT OF PHYSICS

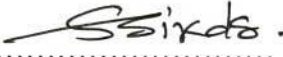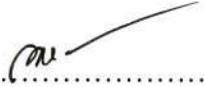**CERTIFICATION OF THESIS WORK**

A THESIS ON

Study of Nanocrystal Formation in FINEMET Metallic Glasses and their Magnetic Properties

By
SIBA PADA MONDAL

has been accepted as satisfactory in partial fulfillment for the degree of Master of Philosophy in Physics and certify that the student demonstrated a satisfactory knowledge in the field covered by his thesis in an oral examination held on December 27, 2008

Board of Examiners

1. Prof. Dr. Shibendra Shekher Sikder
    Department of Physics
    Khulna University of Engineering & Technology

    Supervisor & Chairman

2. Head
    Department of Physics
    Khulna University of Engineering & Technology

    Member

3. Dr. A. K. M. Abdul Hakim
    Chief Engineer & Head
    Materials Science Division
    Atomic Energy Division, Dhaka

    Co-Supervisor & Member

4. Prof. Dr. Md. Mahbub Alam
    Department of Physics
    Khulna University of Engineering & Technology

    Member

5. Prof. Dr. Md. Abu Hashan Bhuiyan
    Department of Physics
    Bangladesh University of Engineering & Technology
    Dhaka-1000, Bangladesh

    Member (External)

DECLARATION

This is to certify that the thesis work entitled as "**Study of Nanocrystal Formation in Finemet Metallic Glasses and Their Magnetic Properties**" has been carried out in partial fulfillment of the requirement for M. Phil degree in the department of Physics, Khulna University of Engineering & Technology, Khulna-9203, Bangladesh. The above research work or any part of this work has not been submitted anywhere for the award of any degree or diploma. No other person's work has been used without due acknowledgement.

1. Supervisor   Candidate

-----------------------------------   -----------------------------------
(Prof. Dr. S. S. Sikder)   (Siba Pada Mondal)

2. Co-Supervisor

(Dr. A. K. M. Abdul Hakim)

This Noble Work Has Been

Dedicated

To

My Father and Mother

Acknowledgements

Abstract

This thesis is based on the experimental investigation of nanocrystal formation from Finemet type of amorphous ribbons subjected to controlled thermal treatment and evolution of unique soft magnetic properties that are microstructure dependent. The samples with nominal compositions $Fe_{75.5}Cu_1Nb_1Si_{13.5}B_9$ (sample-A) and $Fe_{74}Cu_{0.5}Nb_3Si_{13.5}B_9$ (sample-B) have been prepared by rapid solidification technique and their amorphous nature has been confirmed by X-ray diffraction (XRD). The crystallization behavior and the nanocrystal formation have been studied by Differential Thermal Analysis (DTA) and XRD. Magnetic permeability and magnetization measurements have been carried out using inductance analyzer and vibrating sample magnetometer (VSM).

Crystallization onset temperature T_{x_1} corresponding to primary crystallization of bcc Fe(Si) due to which the excellent soft magnetic properties develops is higher for the sample-B (504°C) than that for sample-A (470°C) and the temperature difference between the primary and secondary crystallization peak is higher for sample-B. Therefore sample-B obviously show higher thermal stability. The crystallization onset temperatures determined by XRD are in good agreement with DTA results. The grain sizes determined on annealed samples are from 13 nm to 22 nm for sample-B compared with 17 nm to 27 nm for sample-A.

Magnetic permeability sensitively depends on the annealing temperature for both the samples, which increases sharply with the increase of annealing temperature having substantial higher value for sample-B. Maximum permeability corresponding to optimal annealing temperature were observed at $T_a = 425$°C for sample-A and $T_a = 575$°C for sample-B. This is due to more refined grain structure of 13-22 nm for sample-B. A sharp deterioration of permeability at higher T_a is observed for both the samples and is due to boride phase formation which has been confirmed by μ' vs. T and XRD experiments. Saturation magnetization M_s, increases with T_a for both the samples and finally decreases for annealing at a temperature much higher than peak crystallization temperature. The Curie temperature T_c is higher for sample-A (421°C)

1

than that of sample-B (360°C). The Curie temperature of sample-A is found to increase gradually with T_a up to initiation of crystallization beyond which it decreases. Further increase of T_a, an enhancement of T_c is noticed which may be attributed to the compositional variance resulting in a distribution of Curie temperatures. The high permeability of the optimum nanocrystallized sample in both the cases has been achieved due to drastic decrease of effective anisotropy resulting from nanometric grain size effect and strong magnetic coupling. The results show that amount of Cu and Nb is very important for the soft magnetic properties of Finemet alloys.

CONTENTS

CHAPTER-IV
THEORETICAL ASPECTS

CHAPTER-V
EXPERIMENTAL DETAILS

List of Figures

iv

List of Tables

List Symbols

a_0	Lattice parameter
B	Magnetic induction
D_g	Grain size
DTA	Differential Thermal Analysis
DSC	Differential Scanning Calorimetry
d	Average diameter
FWHM	Full Width at Half Maximum
H	Magnetic field
H_c	Coercivity
H_a	Applied magnetic field
[hkl]	Miller Indices
k	Magnetic hardness parameter
K_{eff}	Effective magnetic anisotropy constant
L	Self inductance of the sample core
L_o	Inductance of the winding coil without sample
L_{ex}	Ferromagnetic exchange length
M	Magnetization
M_s	Saturation magnetization
nm	nano meter
NM	Nobel metal
RAM	Random anisotropy model
TTT	Temperature, time & transformation
T_a	Annealing temperature
T_c	Curie temperature
T_g	Glass transition temperature
T_x	Crystallization temperature
T_m	Melting point
T_{x_1}	Primary crystallization temperature
T_{x_2}	Secondary crystallization temperature
T_{p_1}	Primary crystallization peak temperature
T_{p_2}	Secondary crystallization peak temperature

$\tan\delta$	Loss factor or loss tangent
VSM	Vibrating Sample Magnetometer
XRD	X-ray diffraction
μ	Permeability
μ_i	Initial permeability
μ'	Real part of the complex permeability
μ''	Imaginary part of the complex permeability
μ_m	Maximum permeability
μ_o	Vacuum magnetic permeability
λ	Wave length
θ	Scattering angle
t_o	Time constant
β	Heating rate
ρ	Electrical Resistivity
ω	Frequency
σ	Effective stress
Q	$1/\tan\delta$ (quality factor)
$\mu'*Q$	Relative quality factor
$<K>$	Average anisotropy
T_c^{am}	Curie temperature of residual amorphous matrix
$\|Y\|$	Absolute value of admittance
$\|Z\|$	Absolute value of impedance
ΔH	Enthalpy of crystallization

CHAPTER – 1

INTRODUCTION

Introduction

1.1 General Introduction

Nanocrystalline materials designate a novel type of interface-controlled solids that are characterized by a structural modulation on the length scale of several nanometers. Considering the highly attractive application potentials e.g., ductility of nanocrystalline ceramics at low temperatures, high strength of nanostructured ceramic-metal composites, soft magnetic behavior of nanocrystalline alloys, or a tailoring of new types of alloys, the synthesis and structural studies of nanocrystalline materials have developed rapidly into a challenging field of materials science [1.1-1.3]. The modified properties of nanocrystalline materials are considered as a consequence of the microscopic length scale of the crystal dimensions and in particular of the large number of interfaces.

Nanocrystalline ferromagnetic materials offer a new possibility for tailoring advantageously a variety of phenomena including soft, hard and superparamagnetic behavior. The detailed properties depend upon the interaction mechanism and on the ratio between structural and magnetic correlation lengths. Over the past several decades, amorphous and more recently nanocrystalline materials have been investigated for application in magnetic devices requiring magnetically soft material such as transformers, inductive devices, etc. Research interest in the study of soft magnetic nanostructured materials has been increasing at an accelerating rate, stimulated by recent advances in materials synthesis and characterization techniques and the realization that these materials exhibit many unique and interesting physical, optical, magnetic and chemical properties with a number of potential technological applications [1.4-1.9]. Nanocrystalline soft magnetic materials were first reported in 1988 by Yoshizawa *et al.* [1.10] through controlled crystallization of Fe-Si-B amorphous alloys with the addition of Copper (Cu) and Niobium (Nb). The material was cast as an amorphous ribbon by rapid solidification. Exploitation of this novel material in practical applications started shortly after the discovery and manufactured by Hitachi Co. Ltd. under the trade names FINEMET [1.11] and VITROPERM [1.12]. The originally proposed composition was $Fe_{73.5}Cu_1Nb_3Si_{13.5}B_9$.

1

The nanocrystalline state is achieved by subsequent heat treatment from their as cast amorphous precursor above the primary crystallization temperature. It is characterized by a homogeneous ultra fine grain structure of bcc Fe-Si with grain sizes, D_g of typically 10 to 15 nm and random orientation, embedded in an amorphous minority matrix.

The basic requirements for attaining the soft magnetic properties of the materials are (i) that the grains are exchange coupled and (ii) that the structural correlation length is smaller than the ferromagnetic exchange length. These requirements are connected with the size, distribution of the nanometric grains, their composition, interfaces of the constituent phases, vanishing average magnetic anisotropy $[< K > = 0]$, vanishing magnetostriction $[< \lambda > = 0]$, strong intergrain magnetic coupling and reduced magneto- elastic energy. The best soft magnetic properties are still found around the originally proposed composition i.e. $Fe_{\sim 74}$ Cu_1 Nb_3 Si_{13-16} B_{6-9}. The advantages, however, are a higher saturation induction of 1.2 to 1.3 Tesla and a significantly better thermal stability for the soft magnetic properties.

The novel nanocrystalline soft magnetic materials are basically a two-phase material having various volume fraction of nanocrystalline α-Fe (Si) phase and remaining amorphous phase. The crystallization of bcc Fe (Si) solid solution from amorphous state takes place according to the basic scheme characteristic of the hypo-eutectic glasses [1.13]: $am_1 \rightarrow Fe$ (Si) + am_2, where am_1 and am_2 are the initial amorphous precursor and the remainder amorphous phase respectively. Though this reaction takes place within few seconds as thermal effect, the excellent soft magnetic properties evolve only gradually until the final volume fraction and the appropriate concentration and distribution of the components between the nanograins and the intergranular amorphous shell is reached. There are mainly two phases in the alloys with optimum magnetic properties: a bcc Fe-Si solid solution and some residual amorphous phase. The addition of Cu and Nb results in the formation of ultra fine grain structure. An appropriate thermal treatment above the crystallization temperature of this alloy gives rise to extraordinary soft magnetic properties. A heat treatment around 555°C [1.14] i.e. above the crystallization temperature of the amorphous state, produces a homogeneous, ultra fine grain structure of α-Fe (Si) with

2

bcc structure having a typical grain diameter $D_g = 10 \sim 20$ nm and random texture. The formation of these nanocrystalline structures is ascribed to the combined addition of Cu and Nb, which both are not soluble in α-Fe. Hereby Cu is thought to increase the nucleation of α-Fe grains, where as Nb hinders its growth rate [1.15].

One of the important features of Finemet system is that one can play with different compositions, annealing temperatures and time to control the grain size and their distribution upon which the magnetic properties of these new materials strongly depend. In choosing the composition one has to consider the magnetic components like Fe, Co, Ni etc., the crystallization component e.g. Cu and the component Nb for stabilizing the nanocrystal growth by inhibiting the grain growth and glass forming materials like Si, C, B etc. Amorphous ferromagnetic materials based on Fe-Si-B show good magnetic properties when they are heat-treated below their crystallization temperature. While the Fe-Cu-Nb-Si-B alloys exhibit extraordinary high permeability, two orders of magnitude higher than their conventional Fe-Si-B alloys due to the heat treatment just above the crystallization temperature for a specific time. The great scope of technical applications of this material $Fe_{73.5} Cu_1 Nb_3 Si_{13.5} B_9$ aries from this freedom of tailoring the magnetic properties [1.16-1.19].

The pioneer alloy composition $Fe_{73.5}Cu_1Nb_3Si_{13.5}B_9$ known as FINEMET, has been thoroughly studied due to its novel magnetic properties. Yoshizawa et $al.$ [1.20] and Noh et $al.$ [1.21] studied the effect of Cu on the crystallization behavior in $Fe_{74.5-x}Cu_xNb_3Si_{13.5}B_9$ for x = 0 and x = 1. The Crystallization behavior of this x = 0 alloy is quite different and leads to a severe degradation of the soft magnetic properties compared to the original amorphous state. They also found that the average grain size just after the onset of crystallization is relatively large, up to about 60 nm with a broad scatter, and show a distinct variation with the annealing temperature. This indicates the significantly lower nucleation rate than in the Cu-doped alloy whose finer grain size is almost constant in a wide range of annealing temperature. Furthermore, annealing of the Cu-free alloy leads to the simultaneous or sequential formation of several crystalline phases. A small Cu addition yields two clearly separated crystallization peaks corresponding to the primary crystallization of bcc Fe at T_{x_1} and subsequently to the precipitation of Fe-B compound at T_{x_2}.

3

Cu addition effect is considerably promoted by the simultaneous presence of Niobium (Nb). Nb enhances the crystallization temperatures and retards the grain growth by limiting diffusion. In particular, the Nb addition significantly increases the separation between the two crystallization stages, which promotes the primary crystallization of bcc Fe and stabilizes the residual amorphous matrix against the precipitation of Fe-B compounds. All together this leads to an increased number of simultaneously growing and completing crystals resulting in the nanoscaled microstructure upon alloying at least about 2-3 at. % Nb.

Nb can be substituted by other group V or VI group refractory elements, like Cr, V, Mo, W or Ta which act similarly on the crystallization process and on the magnetic properties [1.22]. Like Nb, the atomic volume of these refractory elements are larger than that of Fe which reduces the diffusion coefficients and, thus stabilizes the amorphous matrix and slows down the kinetics of grain coarsening [1.23, 1.24]. Accordingly the efficiency of these elements for grain size refinement increases in the order of their atomic volumes, i.e., Cr < V < Mo ≈ W < Nb ≈ Ta. Thus, finest grain structures and superior magnetic properties in practice require at least a certain amount of the elements Nb or Ta.

Ayer's *et al.* [1.25] reported that the presence of Nb promotes the formation of Cu-rich clusters on a much finer scale than in an Nb free alloy composition. Small grain size is required for good soft magnetic properties, but at the same time needs to maintain the absence of boron compounds. Herzer [1.26] reported that the separation between the primary crystallization of bcc Fe and the precipitation of Fe-B compounds decreases with increasing boron content. So, it is necessary to keep the boron concentration at a law or moderate level in order to obtain an optimum nanoscales structure. Kubaschewski [1.27] showed that in thermodynamical equilibrium, boron is practically insoluble in bcc Fe (<< 0.01 at. %); the solubilities of Cu and Nb are low: < 0.2 at. % Cu, < 0.1 at. % Nb.

M. A. Hakim *et al.* [1.28] and S. Manjura Hoque *et al.* [1.29] found that magnetic initial permeability and nanocrystalline / amorphous ribbon strongly depends on annealing temperature and exhibits superferromagnetic behavior at T >

T_c^{am}. When $T > T_c^{am}$, the grain coupling is largely but not completely interrupted above T_c^{am} and still persists to higher value of permeability compared to annealed temperature at $T > T_c^{am}$ exhibiting the magnetic coupling between particles is significant. The precise coupling mechanism for this type of behavior at $T > T_c^{am}$ may be explained in terms of exchange penetration through thin paramagnetic intergranular layer and / or dipolar interactions.

The effect of annealing temperature on Saturation Magnetization (M_s) has been reported by Lovas *et al.* [1.30] and Berkowitz [1.31]. M_s is increased with annealing temperature up to initial stage of crystallization temperature and then decreases correspond to the optimum nanocrystallized state with high volume fraction of Fe (Si) nanograins. The influences of Cr-content with higher percertage of Cr on the magnetization behavior of $Fe_{73.5-x}Cr_xCu_1Nb_3Si_{13.5}B_9$ alloy have been studied [1.32-1.33].

1.2   Aim of the present research work

The main purpose of this thesis is to study the crystallization behavior; formation of nanocrystallites and their effect on the magnetic properties of $Fe_{75.5}Cu_1Nb_1Si_{13.5}B_9$ (Sample-A) and $Fe_{74}Cu_{0.5}Nb_3Si_{13.5}B_9$ (Sample-B) herein after would be used as sample-A and sample-B respectively.

The objectives are as follows:
- Synthesis of the FINEMET alloys in the form of ribbon with varying amount of Cu and Nb in the amorphous state by rapid solidification technique.
- Growth of nanocrystals on amorphous matrix by thermal treatment.
- Characterization of nanostructured phases such as the size of the nanograins, Composition of the nanograins.
- Correlation of the evaluation of nanograins with the magnetic properties.
- Optimization of annealing temperature corresponding to the good magnetic properties.

Explain the results using existing theoretical models in the literature.

5

1.3   Organization of the Thesis Work

An overview of nanocrystalline materials are describe in Chapter-II. Chapter-III describes the preparation procedure. The theoretical aspects of the stability of amorphous alloys, Theories of X-ray diffraction, Permeability and Magnetization are described in chapter-IV. Chapter-V contains the experimental details including Differential Thermal Analysis (DTA), X-ray Diffraction (XRD), Impedance Analyzer and Vibrating Sample Magnetometer (VSM).

The details of the results regarding DTA, XRD method after heat treatment of the samples at different temperatures, annealing effects on frequency dependence of initial complex permeability and temperature dependence of initial permeability, annealing effects on magnetization curve are discussed in chapter-VI. It also contains comments on the suitability of the specimens studied, in respect of relative quality factor, loss factor and the frequency range in which these materials are suitable for applications. Chapter-VII contains conclusions, achievement of the works and future suggestions in connection with this research work.

CHAPTER – 2

AN OVERVIEW OF NANOCRYSTALLINE MATERIALS

An Overview of Nanocrystalline Materials

2.1   History of amorphous and nanocrystalline materials

The nanotechnology has its roots date back to a 1959 talk given by Richard Feynman (http:/nano, Xerox.com/nanotech/feynman.html) in which he said, "The principles of physics, as far as I can see, do not speak against the possibility of maneuvering things atom by atom. It is not an attempt to violate any laws; it is something in principle, that can be done; but in practice it has not been done because we are too big". But with the tremendous advancement of science and technology for the last two decades the idea that we should be able to economically arrange atoms in most of the ways permitted by physical law has gained fairly general acceptance. The recent advances in materials synthesis, characterization techniques and methods of advance measurement facilities on the nanometer scale have greatly assisted the expansion of nanotechnology.

These are various methods of preparing nanoparticles and / or nanostructured materials which include: (i) Plasma Processing [2.1, 2.2] (ii) desposition technique [2.3, 2.4] and (iii) rapid quenching and subsequently crystallized to nanometric grains embedded in a remaining amorphous matrix [2.5]. In the present work nanocrystalline alloys have been prepared by the last method.

Amorphous soft magnetic alloys are now well accepted and mature materials. At first the great interest in amorphous metals stems from reports by Duwaz *et al.* [2.6] on the preparation and properties of amorphous metallic alloys. Simpson and Brandley [2.7] appear to have been the first to point out that the amorphous alloys are expected to have no magnetocrystalline anisotropy and should have very low coercivity. Progress in this field is often characterized by further improvement according to specific requirements of particular applications. The first example for soft magnetic behavior in the nanocrystalline state was given by O' Handley *et al.* [2.8] for a devitrified glassy Co-based alloy. However, the soft magnetic properties were inferior than their amorphous counterpart. The most promising properties so far have been found in Fe-based alloys. Therefore, the Co-based alloys after

nanocrystallization by thermal treatment failed to show promising soft magnetic properties.

Amorphous alloys have enormous scientific and technological interest because they do not have any long-range atomic order. As a result these materials have high resistivities, low magnetocrystalline anisotropy and no microstructural inhomogeneities. As a result, these materials are observed to have small hysteretic and eddy current losses. Amorphous alloys are typically formed by rapid solidification processing rules; though more conventional solidification rules are possible for bulk amorphous alloys. The study of metallic glasses dates back to the pioneering work of Pol Duwez at Caltech in the 1950s. Duwez employed atomization [2.9] and gun techniques [2.10] prior to splat quenching [2.11-2.12]. Ferromagnetic amorphous alloys were first reported by Mader and Nowik [2.13]. Soon after, Tsuei and Duwez [2.14] reported splat quenched amorphous ferromagnets with interesting soft magnetic properties. Rapid solidification processing is reviewed only in a cursory manner here, citing techniques, which have been employed to produce materials.

2.2   Review of nanocrystalline soft magnetic materials

2.2.1 Kinds of nanocrystalline alloys

Nanocrystalline amorphous ribbons can be considered as an off-shoot of amorphous materials. Infact nanocrystalline amorphous ribbons are composite materials where nanocrystals are embedded in an amorphous matrix. Nanocrystalline materials represent one of the most active research areas in recent times for the atomic tailoring of materials with specific properties and property combinations. However, it is still in its infancy since its emergence as potential materials has just begun at this stage of development.

Nanocrystalline alloys can be described in general as TL_{1-x} [TE, M, NM]$_x$, where TL denotes a late ferromagnetic transition metal element, TE is an early transition metal element, M is a metalloid and NM is a noble metal. This composition usually has $x < 0.20$ i.e. with as much late ferromagnetic transition metals (TL of Co, Ni, or Fe) as possible. The remaining early transition metals (TE = Zr, Nb, Hf, Ta

8

etc.) and metalloids (M = B, P, Si etc.) are added to promote glass formation in the precursor. The noble metal elements (NM = Cu, Ag, Au etc.) serve as nucleating agents for the ferromagnetic nanocrystalline phase. The compositions are limited by where glass formation can occur prior to the nanocrystalline route. These alloys may be single phase (Type-I) but are generally two-phase materials with a nanocrystalline ferromagnetic phase and a residual amorphous phase at the grain boundaries (Type-II). The Type-II nanocrystalline alloys might have general properties:

    (i)   Relatively high resistivity (50-80 $\mu\Omega$-cm)

    (ii)   Low magnetocrystalline anisotropy and

    (iii)   Increase mechanical strength. With properties such as these, nanocrystalline alloys have great potential as soft magnetic properties.

Nanocrystalline Fe-Cu-Nb-Si-B alloys have been patented by Yoshizawa *et al.* under the trade name FINEMET @^{TM} [2.15, 2.16]. Soft materials based on Fe-M-Cu-B have been patented by Kojima *et al.* [2.17] under the trade name NANOPERM @$^{(TM)}$. This Fe-M-Cu-B [M = Zr, Nb, Hf …] nanocrystalline alloys have all been optimized to achieve small magnetostrictive coefficients and concomitant large permeabilities. More recently (Fe,Co)-M-Cu-B [M = Nb, Hf or Zr] nanocrystalline alloys, called HITPERM have been shown to have attractive induction (1.6-2.1 Tesla) combined with high permeabilities and high Curie temperature. In FINMENTS α-FeSi nanoparticles with a DO_3 structure are observed and in NANOPERM α-Fe particles with bcc structures are formed. In HITPERM alloys nanocrystalline α-bcc and $\acute{\alpha}$-bcc, B2-FeSi (B2)-FeCo are formed with significantly improved high temperature magnetic properties than in the former two.

Nanocrystalline soft magnetic alloys have received considerable attention due to their excellent soft magnetic properties [2.18]. Small addition of Cu and Nb into Fe-Si-B amorphous materials changes considerably their crystallization process, which is executed under appropriately controlled conditions and the specific purpose of these addition are:

- The element Cu is used for helping the formation of nuclei of ultra fine grains and

- The element Nb is used to impede the growth of the crystallites.

In this material, the nanocrystalline state is composed of a fine structure of α-Fe(Si) and is usually around 10 nm. For such an average grain size the exchange interaction dominates the magnetic behavior of randomly oriented crystallites guided by random anisotropy [2.19].

2.2.2 Formation of Nanocrystalline State

A typical nanocrystalline structure with good soft magnetic properties occurs if the amorphous state is crystallized provided the primary crystallization of bcc Fe takes place prior to the formation of secondary inter metallic phases like Fe-B. Both an extremely high nucleation rate and slow growth of the crystalline precipitates are needed in order to obtain a nanoscaled microstructure. Such crystallization characteristic seems to be rather an exception case than the conventional rule. Thus, crystallization of conventional metallic glasses optimized for soft magnetic applications usually yield a relatively coarse grained microstructure of several crystalline phases and correspondingly, deteriorates the soft magnetic properties.

It has been established that controlled crystallization of the amorphous alloys in the form of their ribbons prepared by rapid solidification technique using melt-spinning machine appeared to be the most suitable method available until now to synthesize nanocrystalline alloys with attractive soft magnetic properties. The basic principle for the crystallization method from amorphous solids is to control the crystallization kinetics by optimizing the heat treatment conditions such as annealing temperature and time, heating rate, etc. The nanocrystalline state is achieved by annealing at temperatures typically between about 500°C and 600°C, which leads to primary crystallization of bcc Fe. Fig 2.1 summarizes the evolution of the microstructure and the soft magnetic properties with the annealing temperature. The resulting microstructure is characterized by randomly oriented, ultra fine grain of bcc Fe-Si, 20 at. % with typical grain size of 10-15 nm embedded in a residual amorphous matrix which occupies about 20-30 % of the volume and separates the crystallites at a distance of about 1-2 nm. These features are basis of the excellent soft magnetic properties indicated by the high values of the initial permeability of about 10^5 and corresponding low coercivities of less than 1 A/m. The nanocrystalline microstructure

10

and the accompanying soft magnetic properties are rather insensitive to the precise annealing conditions within a wide range of annealing temperature $(T_a) = 525°C \sim 580°C$ which covers a temperature range $\Delta T_a = 50°C - 100°C$. This developes in a relatively short period of time (about 10-15 minutes) and do not improve much even after prolonged heat treatment of several hours [2.20]. A typical heat treatment like 1h at 540°C in most cases yields a nanocrystalline microstructure to the quasi-equilibrium state and characteristic for the individual alloy composition.
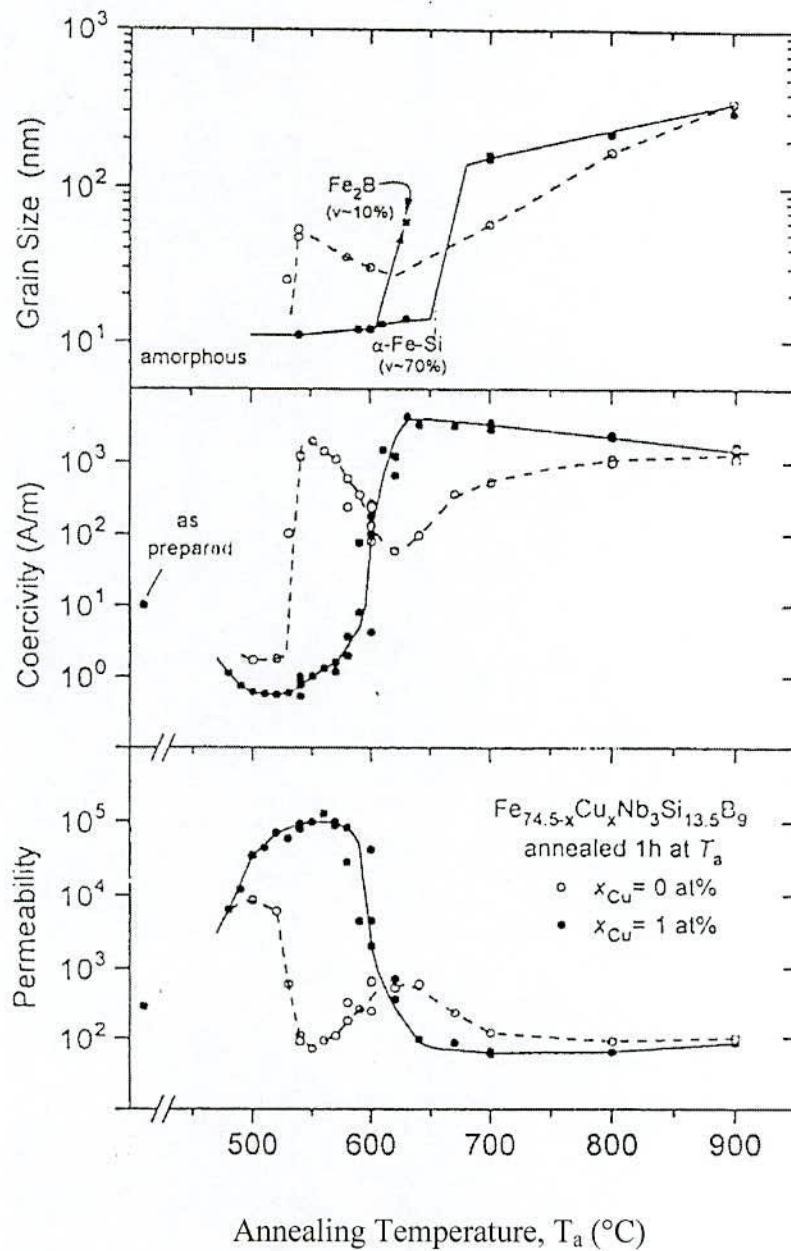
Fig. 2.1 Microstructure and soft magnetic properties with the annealing temperature

Only annealing at more elevated temperature above about 600°C leads to the precipitations of small fractions of boride compounds like Fe_2B or Fe_3B with typical dimensions of 50 nm to 100 nm, while the ultra fine grain structure of bcc Fe-Si still persists. Further increase of the annealing temperature above about 700°C finally yields grain coarsening. Both the formation of Fe borides and grain coarsening deteriorates the soft magnetic properties significantly. The evolution of microstructure during annealing is depicted schematically in Fig. 2.2 and summarized as follows according to Hono *et al.* [2.21-2.22].
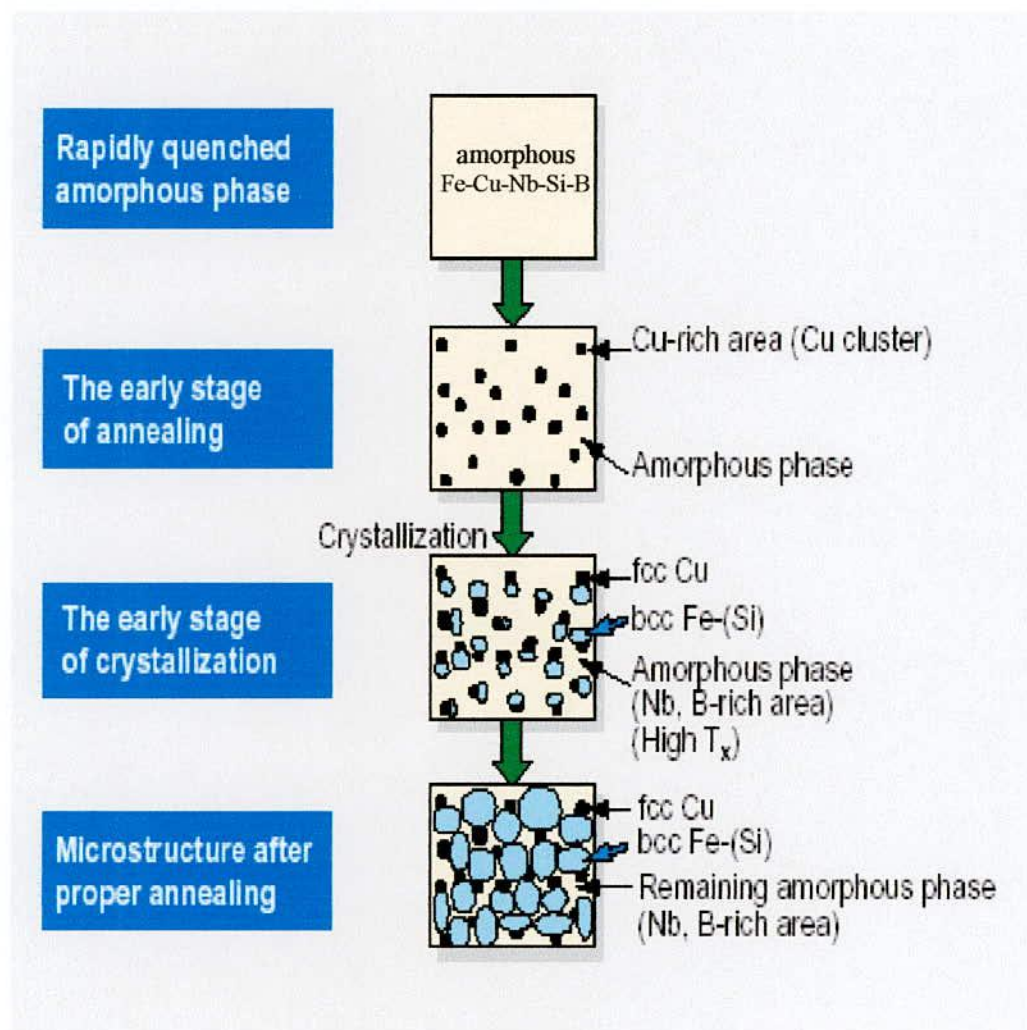
Fig. 2.2 Schematic illustration of the formation of the nanocrystalline structure in Fe-Cu-Nb-Si-B alloys

12

At the initial stage of the annealing, Cu rich clusters are formed by either a spinodal process or nucleation in the amorphous state. Each cluster formation causes a concentration fluctuation of Fe also, since Cu substitutes for Fe. Because of this concentration fluctuation, the density for the nuclei of the bcc crystalline phase is increased significantly although the evidence of concentration fluctuation in the fully amorphous state has not been observed because the investigators [2.23] observed the Cu clusters and bcc phase simultaneously at the early stage of the nanocrystallization. Annealing slightly at higher temperature at the initial stage of crystallization α - Fe(Si) phase forms. At this stage Nb and B are excluded from α-Fe(Si) and are enriched in the remaining amorphous phase, because they are insoluble in the α-Fe(Si) phase. This happens when the annealing treatment is carried out at around 550°C when Cu clusters are formed with a few nanometer diameters.

Thus the regions in between the Cu rich clusters provide a significantly increased density of nucleation sites for the crystallization of bcc Fe. The consequence is an extremely fine nucleation of bcc Fe-Si crystallites at a high rate, which subsequently grow in a diffusion-controlled process [2.23] as the annealing proceeds furthers. As annealing goes on the grain size of the α-Fe (Si) increases. At the same time the Si content of this phase keeps increasing since Si tends to be partitioned to the bcc α-Fe(Si) phase. Since the Nb and B enrichment in the amorphous phase stabilizes the remaining the amorphous phase, the grain growth of the bcc phase eventually stops. The presence of Nb at the same time inhibits the formation of Fe-B compounds. The Cu concentration of the clusters also increases as the crystallization proceeds.

At the optimum stage, three distinct phases are present based on the chemical compositions. As the bcc Fe-Si phase forms, Nb and B are excluded from the crystallites because of their low solubility in bcc Fe and are enriched in the residual amorphous matrix. At the same time effectively all Si tends to be partitioned into the bcc Fe-Si phase [2.24-2.25]. The enrichment with B and in particular, with Nb increasingly stabilizes the residual amorphous matrix and, thus, hinders coarsening of the bcc grains. The presence of Nb at the same time inhibits the formation of Fe boride compounds. The transformation finally ceases in a metastable two-phase

microstructure of bcc Fe-Si embedded in an amorphous Fe-Nb-B matrix. The significance of the Cu addition becomes apparent from Fig. 2.1.

2.3   Advantages of Soft Nanocrystalline Alloys

Nanocrystalline amorphous ribbons are produced by melt-spinning technique to produce an amorphous metal and then heat-treating this alloy at temperature higher than its crystallization temperature. Choice of soft magnetic materials for applications has been guided by recent developments in the field of soft magnetic materials. Amorphous and nanocrystalline magnetic materials, in terms of combined induction and permeabilities are now competitive with Fe-Si bulk alloys and the Fe-Co alloys. In Fig. 2.3 [2.26], figures of merit for Fe-based amorphous alloys, Co-based amorphous alloys and nanocrystalline alloys are summarized. Co-based amorphous alloys, Fe-based amorphous alloys and Nanocrystalline alloys have evolved over the past decades with soft magnetic properties which now exceed those of the bulk alloys based on Fe, Co and Fe-Co.
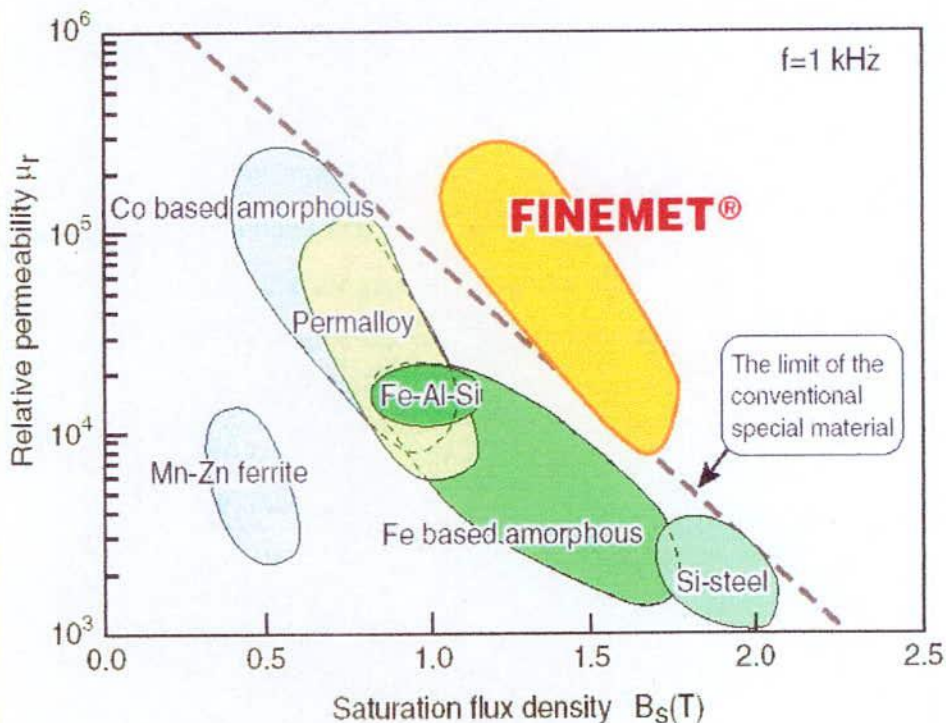
Fig. 2.3 FINEMET is superior compared to conventional materials

14

This FINEMET material is still in its immaturity since its emergence, although much research work has been carried out for the potential utility of this unique material.

At this stage of development, this material has the following advantages:

- High saturation magnetic flux density, more than 1 Tesla or 10 kOe.
- High permeability over $\mu_i \approx 10,000$ at 100 kHz.
- Excellent temperature characteristics.
- Less affected by mechanical stress.
- Very low audio noise emission, lower magnetostriction significantly reduces audible noise emission when the voltage and current is applied to the core at audible frequency range.
- Flexibility to control magnetic properties, "B-H curve shape" during annealing and three types of B-H curve square ness, high, middle and low remanence ratio, corresponding to various applications.

2.4 Viscosity condition for the Formation of Metallic glass

In terms of viscosity and diffusion co-efficient we find the condition for formation of glass:

1. The metals atomic bonding is metallic; the viscosity is lower than the diffusion co-efficient and mobility is high.
2. In the amorphous state viscosity become high and the diffusion co-efficient decreases. Atomic bonds tend to be covalent as in the case of silicate (SiO_2).

2.5 Conditions for the formation of Nanocrystalline alloys

The essential conditions for preparing nanocrystalline materials are:

(i) The magnetic properties are highly dependent on grain size; if the grain size is larger; the magnetic anisotropy would be very high, which in turn will have diverse effect on the soft magnetic properties specially the permeability.

(ii) There should be nucleation centers initiated for the crystallization process to be distributed throughout the bulk of amorphous matrix.

(iii) There must be a nucleation for stabilizing the crystallites.

(iv) Nanocrystalline materials obtained from crystallization must be controlled so that the crystallites do not grow too big. The grain growth should be controlled so that the grain diameter is within 15-20 nm.

(v) The size of the grains can be limited to nanometer scale by doping group-II metals are

$$\rightarrow \text{Cu (Au........)}$$
$$\rightarrow \text{Nb,W, Mo, Cr, Ta etc.}$$

(vi) The stability must be lower and the crystallization must be higher.

In addition to the understanding of the unusual properties possessed by nanophase materials, there are three other associated areas, which need serious attention:

- Identification and development of suitable preparation methods, especially those, which are capable of providing large industrial quantities of nanometer scale materials.

- Development of processing methods for manufacturing these materials into useful size and shapes without losing their desirable nanometer size feature and

- Identification of proper characterization methods, where the nanometer size range of these materials falls just below or at the resolution limit of the conventional tools.

2.6 Grain Size and Coercive force of Nanocrystalline alloys

In the conventional soft magnetic materials, "whose grain size is far larger than 1μm", it is well known that soft magnetic properties become worse and coercive force increases when crystal grain size becomes smaller. For example, coercive force is thought to be inversely proportional to D_g. Therefore, main efforts to improve the soft magnetic properties are directed to make the crystal grain size larger and / or to make the magnetic domain size smaller by annealing and working.

16
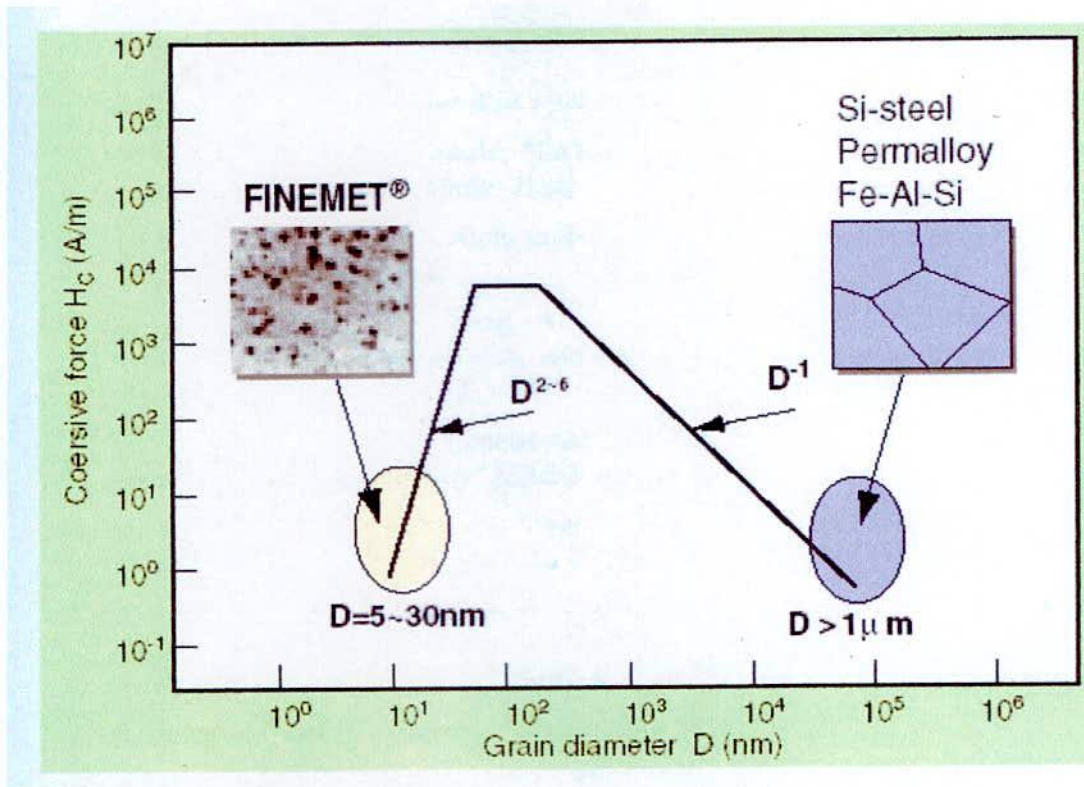
Fig. 2.4 Relation between grain diameter (D_g) and coercive force (H_c)

However, FINEMET demonstrated a new phenomenon; reduction of grain size, "to a nano-meter level", improves the soft magnetic properties significantly. In this nano-world, the coercive force is directly proportional to grain size, D_g on the order of D_g^2 to D_g^6.

CHAPTER – 3

PREPARATION OF NANOCRYSTALLINE ALLOY

Preparation of Nanocrystalline Alloy

3.1   Methods used for Preparation of Nanocrystalline Alloy

There are various techniques in use to produce a metallic alloy in an amorphous state whose the atomic arrangement have no long-range periodicity. The methods are generally classified into two groups

(i)   The atomic deposition methods

(ii)   The fast cooling of the melt.

As we know, controlled crystallization from the amorphous state is the only method presently available to synthesize nanocrystalline alloys with superior soft magnetic properties. In this thesis work amorphous ribbons have been prepared by fast cooling of the melt.

3.1.1 The Fast Cooling of the Melt

The molten alloy must be cooled through the temperature range from the melting temperature (T_m) to the glass transition temperature (T_g) very fast allowing no time for crystallization. The factors controlling T_g and crystallization are both structural and kinetic. Atomic arrangement, bonding and atomic size effect are related in the structural factors. The structural factors as discussed by Turnbull [3.1] are the nucleation, crystal growth rate and diffusion rate compared to the cooling rate. The methods using the principle of fast cooling of melt techniques are:

(i)   The gun techniques

(ii)   Single roller rapid quenching techniques

(iii)   Double roller rapid quenching techniques

(iv)   Centrifuge and rotary splat quenching techniques

(v)   Torsion catapult techniques

(vi)   Plasma-jet spray techniques

(vii)   Filamentary casting techniques

(viii)   Melt extraction techniques

(ix)   Free-jet spinning techniques

(x)   The melt spinning techniques

Among the techniques, the single roller rapid quenching technique is widely used to prepare amorphous ribbons.

3.2   Sample Preparation

3.2.1 Master alloy Preparation

Amorphous ribbons with the nominal composition $Fe_{75.5} Cu_1 Nb_1 Si_{13.5} B_9$ and $Fe_{74} Cu_{0.5} Nb_3 Si_{13.5} B_9$ were prepared in an arc furnace on a water-cooled copper hearth under an atmosphere of pure Ar. Their purity and origin of the constituent elements were Fe (99.9 %), Nb (99.9 %), Si (99.9 %), Cu (99.9 %) and B (99.9 %) as obtained from Johnson Mathey (Alfa Aesar Inc.). The required amounts of constituent elements were taken from pure metal bars or flakes, weighed carefully with a sensitive electronic balance and placed on the copper hearth inside the arc furnace. Before melting the furnace chamber was evacuated (10^{-4} torr), and flashed with Ar gas. The process was repeated several times to get rid of residual air and finally the furnace chamber were kept in an Ar atmosphere.

Fig. 3.1 Vacuum arc Melting Machine

A substantial amount of pure Titanium getter, placed inside of the chamber on the side of the copper hearth was melted first in order to absorb any oxygen present in the furnace chamber. The constituent elements were then melted in the shape of

19

buttons. The arc melting facilities used to prepare the samples are installed at the Centre for Materials Science, National University of Hanoi, Vietnam. The arc furnace used in the preparation of master alloy is shown in Fig. 3.1.

3.2.2 Preparation of ribbon by Melt Spinning Technique

Melt-Spinning is a widely used production method for rapidly solidifying materials as well as preparing amorphous metallic ribbon [3.2-3.3]. In order to prepare amorphous of $Fe_{75.5} Cu_1 Nb_1 Si_{13.5} B_9$ and $Fe_{74} Cu_{0.5} Nb_3 Si_{13.5} B_9$ alloys, a melt spinning facilities was used at the Centre for Materials Science, National University of Hanoi, Vietnam. The arc melted master alloy was crashed into small pieces and put inside the quartz tube crucible for re-melting by induction furnace using a medium frequency generator with a maximum power of 25 kW at a nominal frequency of 10 kHz.

Fig. 3.2 Melt-Spinning Machine

Fig. 3.2 shows the pictorial view of the melt-spinning machine. The quartz crucible has in its bottom part a rectangular nozzle tip of 8 mm length and 0.7 mm

20

width. The position of the nozzle tip can be adjusted with respect to the copper wheel surface, so that the molten alloy was perpendicularly ejected onto the wheel surface from a distance of about 0.3 mm. The small pieces of the master alloy samples were inductively remelted inside the quartz tube crucible followed by ejecting the molten metal with an over pressure of 250 mbar of 99.9 % pure Ar supplied from an external reservior through a nozzle onto a rotating copper wheel with surface velocity of 30 m/sec. The temperature was monitored by an external pyrometer from the upper surface of the molten alloy through a quartz window. The metal alloys were ejected at a temperature of about 150-250 K above the melting point of the alloy. The resulting ribbon samples had thickness of about 20-25 μm and width of ~ 6 mm. Processing parameters such as the thermal conductivity of the rotating quench wheel, wheel speed, ejection pressure, thermal history of the melt before ejection, distance between nozzle of quartz tube and rotating wheel, as well as processing atmosphere have influence on the microstructure and properties of melt-spun ribbons.

The lower pressure of 250 mbar as mentioned above stabilizes the turbulence between melt pull and rotating copper wheel enhancing the heat transfer resulting in a more uniform quenching. As a result, a more uniform ribbon microstructure can be obtained at relatively low wheel speed. With increasing wheel speeds for a given ejection rate, the increasing extraction rate results in thinner ribbons.

3.3 Important Factors to Control the Thickness of Ribbons

(i) Rotating speed:
- Angular velocity ω = 2000 rev/min
- Surface velocity V = 20 m/s to 30 m/s

(ii) Gap between nozzle and rotating copper drum h = 200 to 30 μm

(iii) Oscillations of rotating copper drum both static and dynamic have maximum displacement 1.5 to 5 μm.

(iv) Pressure = 0.2 to 0.3 bar argon atmosphere.

(v) Temperature of molten metals $T_m \cong 1500°C$; other wise quartz tube would be melted.

(vi) A steady flow of the molten metal on the surface of the rotating drum needs to be ensured.

3.4 Confirmation of Amorphousity of Ribbons

The amorphousity of the two ribbons has been checked by X-ray diffraction using Cu-K$_\alpha$ radiation using Philips (PW 3040) X 'Pert PRO XRD System located at Materials Science Division, Atomic Energy Centre, Dhaka (AECD).
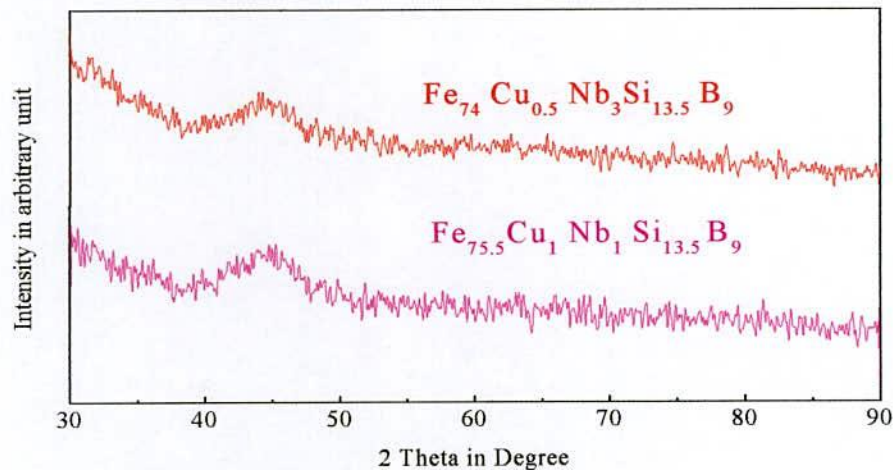
Fig. 3.3 X-ray diffraction of as-cast nanocrystalline amorphous ribbons with compositions $Fe_{74} Cu_{0.5} Nb_3 Si_{13.5} B_9$ and $Fe_{75.5} Cu_1 Nb_1 Si_{13.5} B_9$ alloys

From the XRD pattern of the ribbon samples in Fig-3.3, no peaks are observed within the scanning range. Although there is a small hump is shown in diffraction pattern around $2\theta = 45°$, but it cannot be regarded due to the crystalline effects. So from the over all pattern of the X-ray diffraction it is confirmed that both the samples are in amorphous state.

CHAPTER – 4

THEORETICAL ASPECTS

Theoretical Aspects

4.1 Nature and Formation of Amorphous Alloys

It is very difficult to get pure metals in the amorphous state. It is necessary to add glass forming materials to pure metals or alloys to get the amorphous state and to bring the cooling rate within a reasonable rate. Usually around 20 % of glass forming materials like B, Si, P, C etc which have atomic radii comparatively small compared to those of metallic atoms and the glass forming atoms occupy the voids left between the bigger atoms of metals when they are closely packed. It can be showed that when there is random close packing of hard spheres, there is about 20% voids created between these atoms. The glass forming materials which have smaller atoms occupy these voids which explain the importance of the glass forming material in the preparation of an amorphous ribbon.

The term "amorphous" defines a non-crystalline body while a "glass" refers to a molten mass that is cooled rapidly to prevent crystallization. By analogy, the term "metallic glass" usually refers to a metallic alloy rapidly quenched in order to "freeze" its structure from the liquid state.

The expression "glass" in its original sense refers to an amorphous or nanocrystalline solid formed by continuous cooling of a liquid while a solid is defined somewhat arbitrary as object having a viscosity grater than 10^{14} Pa.s [4.1]. A glass lacks three- dimensional atomic periodicity beyond a few atomic distances. It is characterized by limited number of diffuse halos in X-ray, electron and neutron diffraction and no sharp diffraction contrast in high- resolution electron microscopy. Glasses have been found in every category of materials and of various bond types: covalent, ionic, Vander Walls, hydrogen and metallic.

Glasses are generally formed if upon cooling of a melt, crystal nucleation and/or growth are avoided. At a temperature called glass transition temperature (T_g) the liquid freezes to a rigid solid, however without crystalline order. Thus, glasses and amorphous solids in general are structurally characterized by the absence of long-

range translational order. But a short-range order is still present and may be similar to that found in the crystalline counterpart.

Synthesizing amorphous alloys requires rapid solidification, in order to by-pass the crystallization [4.2]. The metastable structure thus achieved nevertheless may possess a short-range order (SRO) that resembles the equilibrium crystal structure [4.3]. This indicates that the thermodynamic forces that drive crystallization in metals are extremely strong and in most cases, overpowering. Thus the search for alloy systems that allow formation of amorphous structures is of keen technological importance.

Fig-4.1 shows schematically, the time taken for a small amount of crystalline phase to form in an undercooled liquid as a function of temperature. The Temperature-Time-Transformation (TTT) diagram shows a characteristic C curve behavior. At the temperature close to melting point T_m, there is little driving force for crystallization, so that the crystal nucleation and growth rates are small, and the crystallization onset time t_0 is large. As the temperature decreases, the crystallization onset time reaches a minimum value t_0^* at a temperature T_n, and then increases again as the thermal energy becomes insufficient for atomic motion.
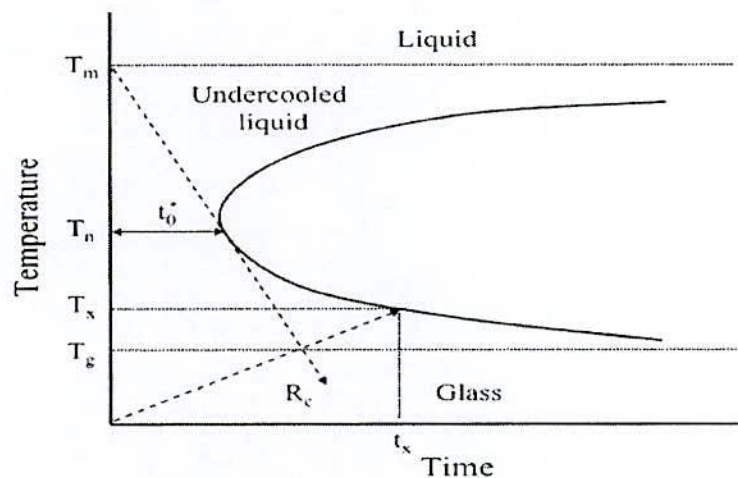
Fig. 4.1 Schematic TTT diagram for the onset of crystallization

24

Close to the glass transition temperature (T_g) atomic motion is completely suppressed and the amorphous structure is frozen in, so that the crystallization onset time t_o, becomes large. Therefore, critical cooling rate R_c to avoid crystallization is given below:

$$R_c = \frac{T_m - T_n}{t_o^*} \tag{4.1}$$

The absence of long-range order (LRO) is easily determined using XRD. In XRD for example, broad diffuse halo peaks are observed with $2\theta \approx 10°$ broadness with Cu-K_α instead of the sharp Bragg peaks shown by crystalline state.

4.2 Factors Contributing to Glass Transition Temperature

There are three inter related factors that determine glass forming tendency. These are thermodynamic conditions that favour the liquid phase relative to the crystalline phase, the kinetic condition that inhibit crystallization and the processing factors that arise due to experimental conditions. The thermodynamic factors for glass formation are liquidus temperature (T_m) at which the alloy melts, the heat of vaporization and the free energy of all the phases that arise or could potentially arise during solidification process. Viscosity of the melt, the glass transition temperature (T_g) and the homogeneous nucleation rate belong to kinetic parameters. The glass transition temperature is defined as the temperature at which the super-cooled liquid takes on the rigidity of a solid or more specifically at which the viscosity approaches 15 poise.

When a liquid is cooled, one of the following two events may occur; either crystallization may take place at the melting point T_m or the liquid will become super cooled below T_m. If the liquid is supercooled sufficiently, its density gradually falls and its viscosity gradually rises. Thus microscopic flow of the liquid becomes progressively more difficult. These changes can be observed by monitoring the volume of the supercooled liquid as a function of temperature and a typical result is shown in Fig. 4.2 [4.4].

The crystallization process is manifested by an abrupt change in volume at T_m, where glass formation is characterized by a gradual break in slope. The region over which the change of slope occurs is termed the glass transition temperature (T_g).
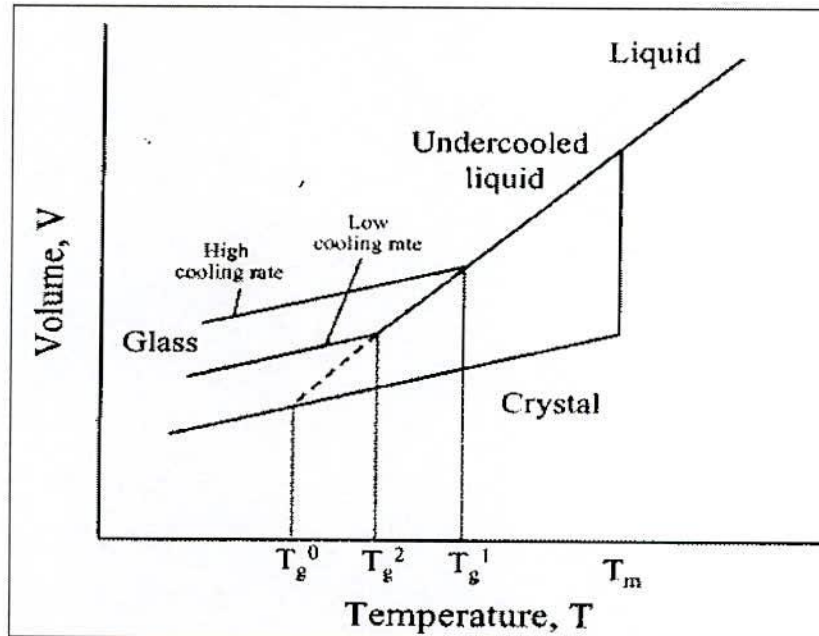
Fig. 4.2 Volume-Temperature relationship in solid, liquid and glassy state

The glass transition temperature is the point at which the alloy finally solidifies with frozen-in amorphous atomic structure. Freezing the amorphous structure at the glass transition temperature (T_g) is a kinetic rather than a thermodynamic transition. Decreasing the cooling rate gives more time for atomic motion, allowing the liquid to maintain its equilibrium structure to lower glass transition temperature (T_g), with a denser, lower entropy structure. The temperature of the glass transition (T_g) is not a constant of the material, but is a function of experimental conditions. The volume (ΔV) and entropy (ΔS) difference between the liquid and the crystal decrease progressively as the temperature falls, and approach zero at a temperature called the ideal glass transition temperature (T_g^o).

Kauzmann [4.5] was the first to point out that an amorphous structure with higher density and lower entropy than the corresponding crystal is impossible, so T_g^0 is the natural lower limit of the range of possible glass transition temperatures (T_g),

26

corresponding to a condition of an infinitely slow cooling rate. In general the glass transition temperature, T_g is defined as the temperature at which an amorphous solid, such as glass or a polymer, becomes brittle on cooling, or soft on heating. More specifically, it defines a pseudo second order phase transition in which a supercooled melt yields, on cooling, a glassy structure and properties similar to those of crystalline materials e.g. of an isotropic solid material [4.6]. The glass transition temperature can be measured by using Differential Thermal Analysis (DTA).

4.3   Stability of the Amorphous Nanocrystalline Materials

Amorphous materials are always in a metastable state, which tend to transform into more stable crystalline phases. There are three kinds of stability of significance for amorphous magnetic alloys: their resistance to the initiation of crystallization, structural relaxation effects and the relaxation or reorientation of directional order. Controlled crystallization from the amorphous state seems to be the only method presently available to synthesize nanocrystalline alloys with attractive soft magnetic properties. The formation and resultant stability of amorphous alloys are important topics both theoretically and technologically. The theoretical analyses of the factors controlling the ease of formation and the stability of the resultant amorphous alloys have been extensively reviewed [4.7-4.8]. From the thermodynamic view point [4.9-4.10], the ability of an alloy to be quenched into the glassy state is generally measured by the magnitude of the quantity.

$$\Delta T_g = T_m - T_g,$$
(4.2)

where T_m and T_g are the melting and glass transition temperature respectively. In a similar manner the stability of the glass after formation is generally measured by the magnitude of the quantity.

$$\Delta T_x = T_x - T_g,$$
(4.3)

where T_X is the temperature for the onset of crystallization. As the temperature decreases from T_m the rate of crystallization will increase rapidly and then fall rapidly as the temperature decreases below T_g. The amorphous alloy composition most favorable for glass formation is near eutectic i.e. the composition in which the

27

transformation from the liquid state to solid state takes place instantaneously without passing through liquid plus solid mixed phase. The deeper the eutectic the better is the glass formation ability [4.11]. There have been three approaches to relating the stability of the glass, i.e., its microstructure:

[i]   Bernal's model of randomly packed hard sphere's [4.12] . The metal atoms are assumed to form a random network of close packed hard spheres and the smaller metalloid atoms fill the holes inherent in such a structure.

[ii] The effect of atomic sizes and interatomic interactions [4.13], i.e. chemical bonding and suggested that it is chemical bonds which are the dominating factors in glass formation and stability.

[iii] The third approach [4.14] is based on the role of the electron gas and showed that under certain circumstances a nearly free electron gas will produce a barrier against crystallization.

The transition to the glassy state and the crystalline state is accompanied by an exothermic heat effect giving rise to a sharp peak in temperature dependence of the heat flow. Therefore, differential thermal analysis (DTA) is a widely used technique to study thermally induced transformations in amorphous alloys and to determine T_g and T_x. The magnitude of T_g and T_x are very different for amorphous materials and depend strongly on composition. The activation energy ranges typically between 2 and 6 eV. [4.15].

4.4 Structure and Microstructure of Amorphous and Nanocrystalline alloys

An amorphous solids is one in which the atomic positions do not have crystalline periodic order. The amorphous structure is postulated to be that of the frozen liquid. The local structure in amorphous metallic materials is distinct from that of window glass. A periodically spaced atom does not exist in amorphous alloys. Therefore XRD does not show any diffraction pattern. If one performs an X-ray scattering experiment on amorphous material, one does observe one or more broad

28

peaks in the scattered intensity shown in Fig. 4.3 at angles similar to those where one or more diffraction peaks would occur in a crystalline alloy of the same composition.

Scherrer analysis of the breadth of the X-ray scattering peak(s), one would conclude that the 'crystallite size' was on the order of atomic dimensions. This is a good argument for only short-range atomic correlations being present in amorphous metals. Scattering experiments on amorphous alloys can be used to determine the so-called radial distribution function that is derived from an appropriate Fourier transform of a normalized scattered intensity expressed as a function of scattering angle.

The atoms in an amorphous solid are not periodically arranged and therefore the concept of a lattice is not appropriate for describing their positions. Thus in an amorphous solid there is not an equivalent concept to that of a lattice and a basis of region to describe atomic positions in a more probabilistic sense using the concept of a pair correlation function, g(r). The pair correlation function is defined as the probability that two atoms in the structure are separated by a distance, r. To define g(r) further begin by considering N atoms in a volume, Ω, letting R_1, R_2, R_3,...., R_N denote the positions of the N atoms with respect to an arbitrary origin. The distance r denotes the magnitude of the vector connecting two atoms i and j,

$$\text{i. e.} \quad r = R_i - R_j \tag{4.4}$$

Two additional atomic distribution functions related to the pair correlation function are the spatially dependent atomic density, $\rho(r)$, which is defined as;

$$\rho(r) = \frac{Ng(r)}{\Omega} , \tag{4.5}$$

and the radial distribution function, RDF(r), which is defined in terms of the pair correlation function as:

$$RDF(r) = 4\pi r^2 \rho(r) \tag{4.6}$$
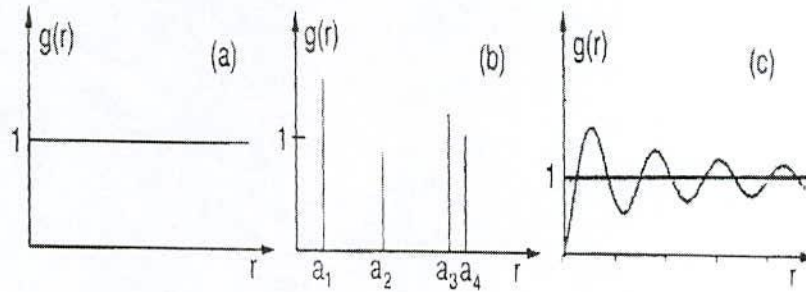
Fig. 4.3 Typical pair correlation function for (a) a completely disordered, (b) a crystalline completely ordered, and (c) an amorphous short-range ordered material

Fig. 4.3 illustrates schematically the distinction between the pair correlation functions for a completely disordered, a crystalline completely ordered and an amorphous short range ordered material. A completely disordered material, like a gas has a uniform unit probability of finding neighboring atoms at all possible distances which leads to a uniform, featureless g(r). On the other hand, a crystalline solid has a set of discrete distances between atomic positions and therefore the pair correlation function in a set of discrete δ-like functions, the amplitude of which reflects the particular coordination number for nearest neighbor, next nearest neighbor,.......etc. pairs of atoms. This is consistent with Bragg scattering (diffraction). In amorphous alloys g(r) is neither discrete nor featureless; instead broad peaks reflect the short-range order in these materials.

4.5   Determination of Nanometric Grain Size by X-ray Diffraction

Nanocrystalline alloys are basically crystalline, and because of their crystallinity they exhibit Bragg scattering peaks in X-ray diffraction experiments. However, due to their small size, significant fine particle broadening is observed in the Bragg peaks. The X-ray scattering from a crystalline solid is given by Bragg's law:

$$2d \sin \theta = n\lambda \qquad (4.7)$$

This equates the path difference of X-rays scattered from parallel crystalline planes spaced $d = d_{hkl}$ apart to an integral number (n) of X-ray wavelength λ. Here θ is the X-ray angle of incidence (and of diffraction) measured with respect to the crystalline planes. For an infinite crystal Bragg scattering occurs at discrete values of 2θ satisfying the Bragg condition, i.e. Bragg peaks are δ-functions. For finite sized crystals the peaks are broadened over a range of angles as shown in fig. 4.4.
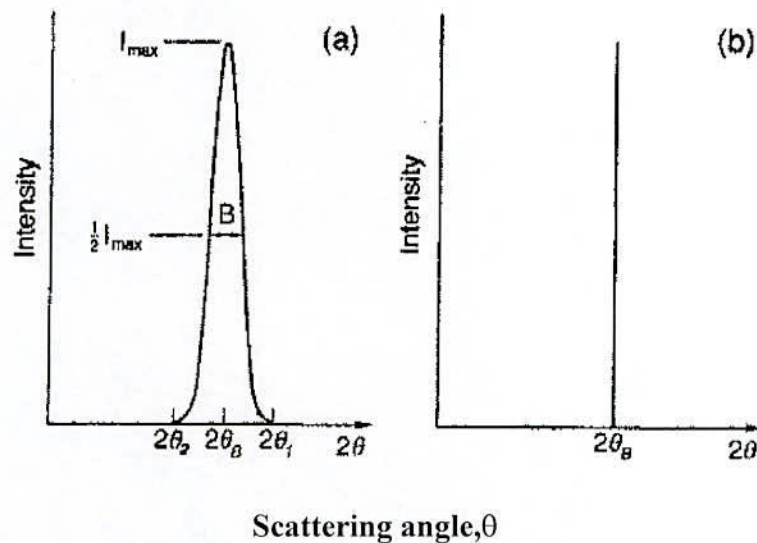
Fig. 4.4 Effect of fine particle broadening in XRD (a) fine particles and (b) perfect crystal

To better understand the phenomenon of fine particle broadening following the arguments of Cullity, [4.16], is out lined below. We consider a finite crystal of thickness, $D_g = md$, where m is an integer, and d is the distance between crystalline planes, i.e., there are m planes in D_g. Considering Fig. 4.4, if the broadened Bragg peak begins at an angle $2\theta_2$ and ends at $2\theta_1$, the breadth of the peak or full width at half maximum is given as:

$$\beta = \frac{1}{2}(2\theta_1 - 2\theta_2) = \theta_1 - \theta_2 \qquad (4.8)$$

Now consider the path differences for each of the two angles θ_1 and θ_2, for X-rays traveling through the full thickness of the crystal. The width β is usually measured in radians, an intensity equal to half the maximum intensity. As a rough

31

measure of β, we can take half the difference between the two extreme angles at which the intensity is zero, which amounts to assuming that the diffraction line is triangular in shape. We now write path difference equations for these two angles, related to the entire thickness of the crystal rather to the distance between adjacent planes.

$$2D_g \, \sin\theta_1 = (m+1)\lambda \qquad (4.9)$$

$$2D_g \, \sin\theta_2 = (m-1)\lambda \qquad (4.10)$$

By subtraction we find:

$$D_g \, (\sin\theta_1 - \sin\theta_2) = \lambda \qquad (4.11)$$

$$D_g \, 2\cos\left(\frac{\theta_1 + \theta_2}{2}\right)\sin\left(\frac{\theta_1 - \theta_2}{2}\right) = \lambda \qquad (4.12)$$

But θ_1 and θ_2 are both very nearly equal to θ, so that $\theta_1 + \theta_2 \approx 2\theta$ and $\sin\left(\frac{\theta_1 - \theta_2}{2}\right) \approx \left(\frac{\theta_1 - \theta_2}{2}\right)$ so that equation (3.12) can be written as:

$$2D_g \, \cos\theta\left(\frac{\theta_1 - \theta_2}{2}\right) = \lambda \qquad (4.13)$$

From equation (4.8) and equation (4.13) we get:

$$\beta . D_g \, \cos\theta = \lambda$$

$$D_g = \frac{\lambda}{\beta \cos\theta} \qquad (4.14)$$

A more exact empirical treatment yields:

$$D_g = \frac{0.9\lambda}{\beta \cos\theta}, \qquad (4.15)$$

which is known as the Scherrer's formula. It is used to estimate the particle size of very small crystals from the measured width of their diffraction curves.

4.6   Random Anisotropy Model (RAM)

The soft magnetic properties of Finemet type of nanocrystalline materials are based on Random Anisotropy Model (RAM) proposed by Herzer [4.17]. Soft magnetic properties of nanocrystalline alloys are strongly dependent on the grain size

32

and grain boundary structure. In order to interpret the behavior of the magnetic properties for atomic scale grains, the RAM was originally proposed by Alben *et al.* [4.18] for amorphous ferromagnets. The basic idea is sketched in fig 1.1 and starts from an assembly of ferromagnetically coupled grains of size D_g with magneto-crystalline anisotropies K_1 oriented at random.
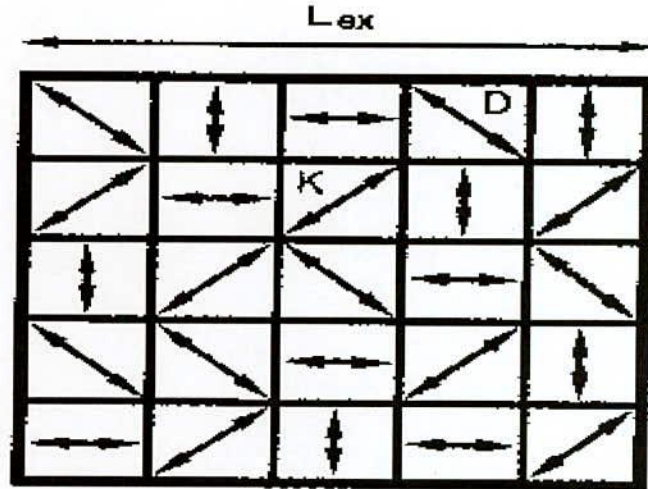
Fig.4.5: Schematic representation of the random anisotropy model. The arrows indicate the randomly fluctuating magnetocrystalline anisotropies

The concept of a magnetic exchange length (L_{ex}) and its relationship to the domain wall width (δ_w) and nano domain size is important in the consideration of magnetic anisotropy in nanocrystalline soft magnetic materials [4.19]. These can be defined by appealing to a Helmholz free energy function as described by Coey [4.20]. These length scales are:

$$\delta_w = \pi\sqrt{\frac{A}{K_1}} \quad \text{and} \quad L_{ex} = \sqrt{\frac{A}{4\pi M_s^2}} \tag{4.16}$$

Herzer considers a characteristic volume whose linear dimension is the magnetic exchange length, $L_{ex} \sim \left(\frac{A}{K_1}\right)^{\frac{1}{2}}$, where K_1 is the magnetocrystalline anisotropy. Given the discussion above, the unstated constant of proportionality should be $\left(\frac{k}{\pi}\right)$ which for materials with very small K_1 can in fact be quite large. Ignoring this constant of proportionality, the Herzer's argument considers N grains, with random

easy axes, within a volume of L_{ex}^3 to be exchange coupled. Since the easy axes are randomly oriented, a random walk over all N grains will yield an effective anisotropy which is reduced by a factor of $\left(\frac{1}{N}\right)^{\frac{1}{2}}$ from the value K_1 for any one grain, thus $K_{eff} \approx \frac{K_1}{\sqrt{N}}$. Now the number of grains in this exchange coupled volume is just $N \approx \left(\frac{L_{ex}}{D_g}\right)^3$, where D_g is the average diameter of individual grains. The ferromagnetic correlation volume $V = L_{ex}^3$ is determined by the exchange length L_{ex}. Relevant to the magnetization process, results from averaging over the $N = V_{cr}\left(\frac{L_{ex}}{D_g}\right)^3$ grains, volume fraction V_{cr}, with magneto crystalline anisotropy oriented at random.

Treating the anisotropy self-consistently then;

$$K_{eff} = V_{cr}\frac{K_1}{\sqrt{N}} = V_{cr}{}^{\frac{1}{2}} K_1 \left(\frac{D_g}{L_{ex}}\right)^{\frac{3}{2}} \tag{4.17}$$

The ferromagnetic exchange length, $L_o = \sqrt{\dfrac{A}{K_1}}$

The exchange length L_{ex}, has to be normalized by substituting $4\pi M_s{}^2 = K_{eff}$ in equation (4.16) i.e. L_{ex} is self-consistently related to the average anisotropy by

$$L_{ex} = \left(\frac{A}{K_{eff}}\right)^{\frac{1}{2}} \tag{4.18}$$

The combination of equation (4.17) and equation (4.18) then

$$K_{eff} = \sqrt{V_{cr}} \; K_1 \left[\frac{D_g}{\sqrt{\frac{A}{K_{eff}}}}\right]^{\frac{3}{2}}$$

$$= \sqrt{V_{cr}} \; K_1 \left[\frac{D_g \sqrt{K_{eff}}}{\sqrt{A}}\right]^{\frac{3}{2}}$$

$$= \sqrt{V_{cr}} \; K_1 \left[\frac{D_g \sqrt{K_{eff}}}{L_o \sqrt{K_1}}\right]^{\frac{3}{2}}$$

$$K_{eff}^{4} = V_{cr}^{2} K_{1}^{4} \frac{D_{g}^{6} \left(\sqrt{K_{eff}} \right)^{6}}{L_{o}^{6} \left(\sqrt{K_{1}} \right)^{6}}$$

$$= V_{cr}^{2} K_{1}^{4} \frac{D_{g}^{6}}{L_{o}^{6}} \frac{K_{eff}^{3}}{K_{1}^{3}}$$

$$K_{eff} = V_{cr}^{2} K_{1} \left(\frac{D_{g}}{L_{o}} \right)^{6}$$

$$K_{eff} = V_{cr}^{2} K_{1} \frac{D_{g}^{6}}{\left(\sqrt{\frac{A}{K_{1}}} \right)^{6}}$$

$$= V_{cr}^{2} K_{1} \frac{D_{g}^{6}}{A^{3}} K_{1}^{3}$$

$$= V_{cr}^{2} D_{g}^{6} \frac{K_{1}^{4}}{A^{3}}$$

$$K_{eff} = \frac{V_{cr}^{2} D_{g}^{6} K_{1}^{4}}{A^{3}} \qquad (4.19)$$

Since the coercivity can be taken as proportional to the effective anisotropy, this analysis leads to Herzer's prediction that the effective anisotropy and therefore the coercivity should grow as the 6th power of the grain size:

$$H_{c} \sim D_{g}^{6} \qquad (4.20)$$

For such a reduction in the coercivity to be realized, Herzer noted that the nanocrystalline grains must be exchange coupled. This to be contrasted with uncoupled particles that have an exchange length, comparable to the particle diameter are susceptible to super paramagnetic response.

The most significant feature predicted by the RAM is the strong variation K_{eff} with the 6th power of the grain size. Thus for $D_{g} \approx \frac{L_{o}}{3}$, i.e. grain sizes in the order of 10-15 nm, the magneto crystalline anisotropy is reduced by three order of magnitude towards a few J/m^{3}, i. e., small enough to enable superior soft magnetic behavior .

The K_{eff}, essentially determines the magnetic softness' since H_c and inverse of initial permeability (μ_i) are proportional to K_{eff}. Therefore it is expected that these quantities have similar dependence on grain size and have been confirmed experimentally [4.21]. Herzer explained the grain size dependence of the H_c based on RAM considering the nanocrystalline materials as single-phase magnetic system. Hernando et al. [4.22] extended this model for two-phase materials and were able to explain the thermal dependence of the coercivity [4.23-4.24]. Hernando has generalized RAM [4.21], taking into account the two phase character of nanocrystalline materials, and it explained the previously maintained hardening as well as other features which could not be understood without the generalization. Since the dimensions of the crystallites dictate the unique properties by controlling the annealing temperature of the specimens, the magnetic softness or hardness in respect of permeability is determined by the grain size, grain distribution and the volume fraction, which are developed on the amorphous matrix in the nanostructure system.

4.7 Theories of Permeability

The initial permeability (μ_i) is defined as the derivative of induction **B** with respect to the initial field **H** in the demagnetization state.

$$\mu_i = \frac{dB}{dH}\bigg|\ H \to 0, B \to 0 \tag{4.21}$$

In electromagnetism, permeability is the degree of magnetization of materials that responds linearly to an applied magnetic field. Permeability is defined as the proportionality constant between the magnetic field induction **B** and applied field intensity **H**;

$$B = \mu H \tag{4.22}$$

This definition needs modification when magnetic material is subjected to an ac magnetic field as given below

$$H = H_0 e^{i\omega t} \tag{4.23}$$

36

In such a field the magnetic flux density (**B**) experience a delay with respect to **H**. The delay is caused due to the presence of various losses and is thus expressed as,

$$B = B_0 e^{i(\omega t - \delta)} \qquad (4.24)$$

where δ is the phase angle and marks the delay of B with respect to H, the permeability is then given by

$$\mu_i = \frac{B}{H}$$

$$= \frac{B_0 e^{i(\omega t - \delta)}}{H_0 e^{i\omega t}}$$

$$= \frac{B_0 e^{-i\delta}}{H_0}$$

$$= \frac{B_0}{H_0} \cos\delta - i\frac{B_0}{H_0}\sin\delta$$

$$\mu_i = \mu' - i\mu'' \quad , \qquad (4.25)$$

$$\text{where } \mu' = \frac{B_0}{H_0}\cos\delta \text{ and } \mu'' = \frac{B_0}{H_0}\sin\delta \qquad (4.26)$$

The real part μ' of complex permeability μ_i as expressed in equation (4.25) represents the component of B which is in phase with H, so it corresponds to the normal permeability. If there are no losses, we should have $\mu_i = \mu'$.

The imaginary part μ'' corresponds to that part of B, which is delayed by phase angle ranging up to 90° from H. The presence of such a component requires a supply of energy to maintain the alternating magnetization, regardless of the origin of delay.

It is useful to introduce the loss factor or loss tangent $(\tan\delta)$. The ratio of μ'' to μ', from equation (4.26), gives

$$\frac{\mu''}{\mu'} = \frac{\dfrac{B_0}{H_0}\sin\delta}{\dfrac{B_0}{H_0}\cos\delta} = \tan\delta \qquad (4.27)$$

This $\tan \delta$ is called the Loss factor or Loss tangent. The Q-factor or quality factor is defined as the reciprocal of this loss factor, i.e.

$$Q = \frac{1}{\tan \delta} \qquad (4.28)$$

and the relative quality factor $= \frac{\mu_i}{\tan \delta}$. The behavior of μ' and μ'' versus frequency is called the permeability spectrum. The initial permeability of a ferromagnetic substance is the combined effect of the wall permeability and rotational permeability mechanism.

4.7.1 Relative Permeability

At microwave frequency, and also in low anisotropic amorphous materials, dB and dH may be in different directions, the permeability thus as tensor character. In the case of amorphous materials containing a large number of randomly oriented magnetic atoms the permeability will be scalar. As we have

$$B = \mu_o (H + M) \qquad (4.29)$$

and Susceptibility

$$\chi = \frac{dM}{dH} = \frac{d}{dH} \left[\frac{B}{\mu_o} - H \right] \qquad (4.30)$$

$$\chi = \frac{1}{\mu_o} \left(\frac{dB}{dH} \right) - 1 = \frac{\mu}{\mu_o} - 1 \qquad (4.31)$$

Relative permeability, sometimes denoted by μ_r, is the ratio of the permeability of a specific medium to the permeability of free space μ_o.

$$\mu_r = \frac{\mu}{\mu_o} \qquad (4.32)$$

In terms of relative permeability, the magnetic susceptibility is

$$\chi_m = \mu_r - 1 \qquad (4.33)$$

38

4.7.2 High frequency Behavior and Losses

The frequency dependence of the absolute value of complex permeability and its imaginary part μ'' are expressed in terms of the relative loss factor $\dfrac{\mu''}{|\mu|^2}$. The later is directly related to the cycle losses at constant induction amplitude B by

$$\frac{p}{f} = \frac{\pi B^2 \mu''}{\mu_o |\mu|^2} \qquad (4.34)$$

Fig. 4.6. shows the core losses of the nanocrystalline Fe-Cu-Nb-Si-B alloys are comparable to those of amorphous Co-based alloys and pass by the properties of conventional materials, even that of ferrites, over the whole frequency range up to several 100 kHz.
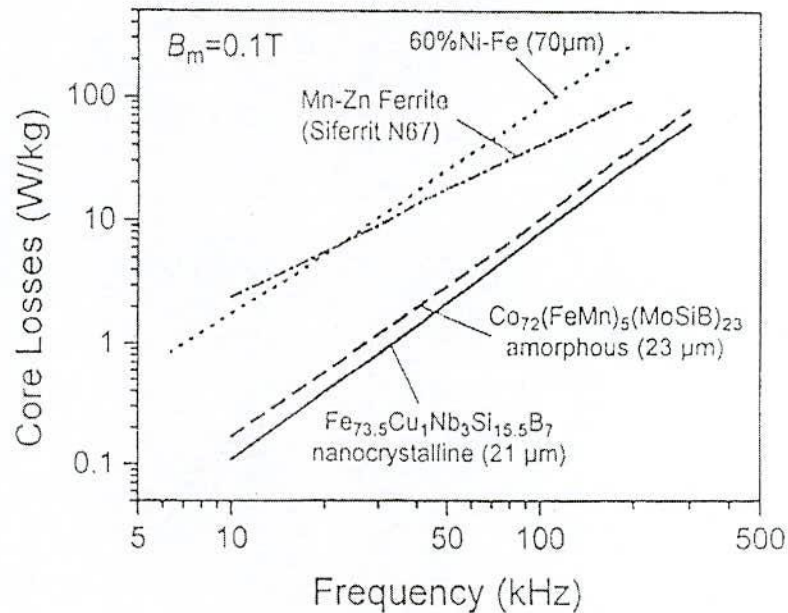
Fig. 4.6 Low core losses of Fe-based nanocrystalline alloy at high frequency

The favorable high frequency behavior is essentially related to (i) the thin ribbon gauge of $d \approx 20\,\mu m$ inherent to the production technique and (ii) to a relatively high electrical resistivity of typically $\rho \approx 115\,\mu\Omega - cm$ related to the high Si-content

in the bcc grains [4.25] and the intergranular amorphous phase. Both parameters are comparable to amorphous metals and yield low eddy current losses p_e, which in thin sheets at a frequency f and a induction level B are given per volume by [4.26]

$$p_e = \left(\frac{3\sinh x - \sin x}{x\cosh x - \cos x} \right) \frac{(\pi d f B)^2}{6\rho}$$

$$\left. |p_e| \right|_{x \angle \angle 1} = \frac{(\pi d f B)^2}{6\rho} \tag{4.35}$$

$$\text{with } x = 2\sqrt{\frac{f}{f_w}}, \quad \text{where } f_w = \frac{4\rho}{\pi \mu_o \mu_i d^2}, \tag{4.36}$$

is the limiting frequency above which the exciting magnetic field no longer fully penetrates the specimen and, accordingly, the permeability decreases as a function of the frequency.

4.8   Magnetic dipole moments and Magnetization

The majority of soft magnetic materials have one or more of the ferromagnetic transition metal elements, Fe, Co or Ni, or the rare earth metal Gd as a majority component. The magnetic dipole moments of element and alloy magnets are almost completely understood through the band theory of solids [4.27]. The band theory of solids considers the broadening of localized atomic states with discrete eigen values into a continuum of states for more itinerant electrons over a range of energies. The theory allows for calculation of energy dispersion (i.e. energy as a function of wave vector) and orbital angular momentum specific and spin-resolved densities of states. The calculation of spin-resolved energy bands and densities of states allows for the description of atom resolved magnetic dipole moments and, therefore, spontaneous magnetization of element and alloy magnetic solids. Among the successes of the band theory descriptions of magnetic properties are:

- The prediction of non-integral or half integral atomic dipole moments and resulting ground state magnetization in metals and alloys.

- The prediction that band widths and exchange splitting (energy differences between spin up and spin down bands) are intimately dependent on magnetic coordination number and atomic volume.

The number of spin up, n_+ and spin down, n_- electrons in each band can again be calculated by integrating these densities of state:

$$n_+ = \int_0^{E_F^+} g_+(E)dE \qquad (4.37)$$

$$\text{and } n_- = \int_0^{E_F^-} g_-(E)dE, \qquad (4.38)$$

where the Fermi energies E_F, are the same and the Zero's of energy are different for the two spin bands. The atom resolved (i.e. Fe on Co) magnetic dipole moments can be calculated as:

$$\mu_m = (n_+ - n_-)\mu_B \qquad (4.39)$$

Knowledge of atomic volumes of alloy density, then allows for the direct calculation of the alloy magnetization.

4.9 Ferromagnetic ordering (Curie) Temperatures

Ferromagnetism is a collective phenomenon since individual atomic moments interact so as to promote alignment with one another. This collective interaction gives rise to the temperature dependence of the magnetization. Two models have explained the interaction between atomic moments. Mean Field Theory considers the existence of a non-local internal magnetic field, called the Weiss field, which acts to align magnetic dipole moments even in the absence of an applied field H_a. Heisenberg Exchange Theory considers a local (usually nearest neighbor) interaction between atomic moments (spins) which acts to align adjacent moments even in the absence of a field.

The basic assumption of the mean field theory is that this internal field is non-local and is directly proportional to the sample magnetization.

$$H_{INT} = \lambda_W M, \qquad (4.40)$$

41

where the constant of proportionality, λ_W, is called the Weiss molecular field constant.

To consider ferromagnetic response in applied field, H_a, as well as the randomizing effects of temperature, we consider the superposition of the applied and internal magnetic fields. By analogy with the problem of paramagnetic moments, the average atomic dipole moment can be expressed in terms of the Brillouin function

$$< \mu_m > = \mu_m^{atom} B_J (\alpha') , \tag{4.41}$$

where $\alpha' = -\left(\dfrac{\mu_0 \mu_m^{atom}}{K_B T} \right)(H + \lambda_W M)$ for a collection of classical dipole moments. The saturation magnetization

$$M_S = N_m < \mu_m^{atom} > \tag{4.42}$$

$$\frac{M}{N_m \mu_m^{atom}} = \frac{M}{M_s} = B_J \left[H + \lambda_w M \right] \tag{4.43}$$

Under appropriate conditions, this leads to solutions for which there is a non-zero magnetization (spontaneous magnetization) even in the absence of an applied field.

For $T > T_c$, the ferromagnetic Curie temperature the only solution to equation (4.43) is $M = 0$, i.e., no spontaneous magnetization and thus paramagnetic response. For $T < T_c$, we obtain solutions with a non-zero, spontaneous magnetization, the defining feature of a ferromagnet.

Ferromagnetic exchange interactions set the scale for Curie temperatures in ferromagnetic alloys. Interatomic exchange couplings can be calculated from first principles by considering the energy change associated with rotation of individual spins in the host material. These exchange interactions can be used within a mean field theory to estimate the Curie temperature. An empirical description of the variations of the exchange energy with interatomic spacing called the Bethe-Slater curve is instructive in describing the effect of alloying on ferromagnetic Curie temperatures. The interplay between electron-electron Coulomb interactions and the constraints of the Pauli Exclusion Principle determine the sign of the exchange interaction.

In transition metal solids a measure of the overlap between nearest neighbor d-orbital is given by the ratio of the atomic to the 3d ionic (or nearest neighbor) radius. In mean field theory the Curie temperature can be related to the exchange energy as follows:

$$T_C = \frac{2S(S+1)}{3K_B}\sum_{ij}T_{ij} \, ,$$

(4.44)

where S is the total spin angular momentum, K_B is the Boatman's constant and T_{ij} is the exchange interaction between atoms at the position r_i and r_j.

In first case, a unique constant exchange interaction between the magnetic atoms is assumed and the amorphous nature of the alloy is taken into account by calculating a random distribution of the local anisotropy field [4.26]. In the second approach is treating this problem of distribution of exchange integrals assumed in order to reflect the structural fluctuations in the amorphous alloy [4.28]. Both approaches predict that M vs. T curve will flat below that for the crystalline counter part.

CHAPTER – 5

EXPERIMENTAL DETAILS

Experimental Details

5.1   Thermal Analysis Techniques

Thermal analysis comprises of a group of techniques in which a physical property of a substance is measured as a function of temperature, while the substance is subjected to a controlled temperature programme. In differential thermal analysis (DTA), the temperature difference that develops between a sample and an inert reference material is measured, when both are subjected to identical heat treatments. The related technique of differential scanning calorimetry relies on difference in energy required to maintain the sample and reference at an identical temperature.

5.1.1 The Principle of Differential Thermal Analysis

The DTA technique was first suggest by Le Chatelier [5.1] in 1887 and was applied to the study of clays and ceramics. DTA involves heating or cooling a test sample and inert reference under identical conditions, while recording any temperature difference between the sample and reference. This differential temperature is then plotted against time, or against temperature. When a sample and reference substance are heated or cooled at a constant rate under identical environment, their temperature differences are measured as a function of time or temperature as shown by the curve in Fig.5.1 (a).
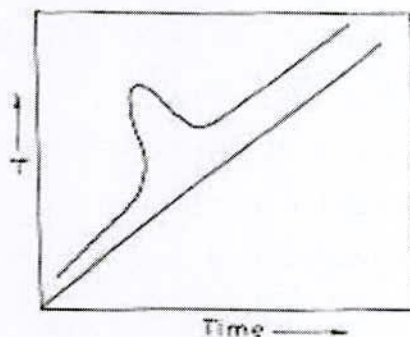
Fig. 5.1(a) Heating curve of sample and reference substance

44

The temperature of the reference substance, which is thermally inactive, rises uniformly when heated, while the temperature of the sample under study changes anomalously when there is physical or a chemical change of the active specimen at a particular temperature. When there is an exothermic reaction there is a peak in the temperature versus time curve, heat supplied from outside is consumed by the reaction. And when the reaction is over, the sample temperature gradually catch up the temperature of the inactive specimen. The temperature difference ΔT is defined, amplified and recorded by a peak as shown in Fig. 5.1 (b).
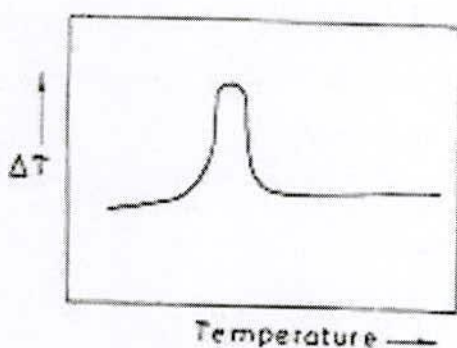
Fig.5.1 (b) DTA Curve

For any endothermic reaction or change the active specimen absorbs heat which is reflected in the corresponding the trough in temperature versus time curve. Changes in the sample, which leads to the absorption or evolution of heat, can be detected relative to the inert reference. Differential temperatures can also arise between two inert samples when their response to the applied heat treatment is not identical. DTA can therefore be used to study thermal properties and phase changes which do not lead to a change in enthalpy. The baseline of the DTA curve showed then exhibit discontinuities at the transition temperatures and the slope of the curve at any point will depend on the microstructural constitution at that temperature. The area under a DTA peak can be related to the enthalpy change and is not affected by the heat capacity of the sample. DTA may be defined formally as a technique for recording the difference in temperature between a substance and a reference material against either time or temperature as the two specimens are subjected to identical temperature regimes in an environment either heated or cooled at a controlled rate.

45

5.1.2 Apparatus

The key features of a DTA kit are as shown in Fig. 5.2: sample holder comprising thermocouples, sample containers and a ceramic or metallic block, a furnace, temperature programmer, recording system. The essential requirements of the furnace are that it should provide a stable and sufficiently large hot-zone and must be able to respond rapidly to commands from the temperature programmer. A temperature programmer is essential in order to obtain constant heating rates. The recording system must have a low inertia to faithfully reproduce variations in the experimental set-up.
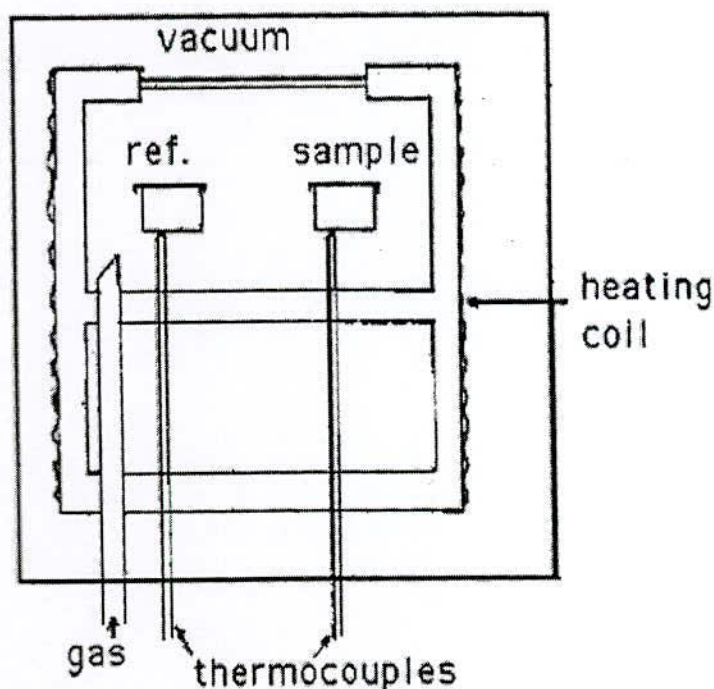
Fig.5.2: Schematic illustration of a DTA cell

The sample holder assembly consists of a thermocouple each for the sample and reference, surrounded by a block to ensure an even heat distribution. The sample is contained in a small crucible designed with an indentation on the base to ensure a snug fit over the thermocouple bead. The crucible may be made of materials such as pyrex, silica, nickel or platinum, depending on the temperature and nature of the tests involved. The thermocouples should not be placed in direct contact with the sample to

avoid contamination and degradation, although sensitivity may be compromised. Metallic blocks are less prone to base-line drift when compared with ceramics which contain porosity. On the other hand, their high thermal conductivity leads to smaller DTA peaks.

The sample assembly is isolated against electrical interference from the furnace wiring with an earthed sheath, often made of platinum-coated ceramic material. The sheath can also be used to contain the sample region within a controlled atmosphere or a vacuum.

During experiments a temperature problems are encountered in transferring heat uniformly away from the specimen. These may be mitigated by using thermocouples in the form of flat discs to ensure optimum thermal contact with the now flat-bottomed sample container, made of aluminium or platinum foil. To ensure reproducibility, it is then necessary to ensure that the thermocouple and container are consistently located with respect to each other.

5.1.3 Experimental Factors

Care is necessary in selecting the experimental parameters. For example, the effects of specimen environment, composition, size and surface to volume ratio all affect powder decomposition reactions, whereas these particular variables may not affect solid state phase changes. Experiments are frequently performed on powders so the resulting data may not be representative of bulk samples, where transformations may be controlled by the build up of strain energy. The packing state of any powder sample becomes important in decomposition reactions and can lead to large variations between apparently identical samples.

In some circumstances, the rate of heat evolution may be high enough to saturate the response capability of the measuring system; it is better than to dilute the test sample with inert material. For the measurement of phase transformation temperatures, it is advisable to ensure that the peak temperature does not vary with sample size. The shape of a DTA peak does depend on sample weight and the heating

47

rate used. The influence of heating rate on the peak shape and disposition can be used to advantage in the study of decomposition reactions, but for kinetic analysis it is important to minimize thermal gradients by reducing specimen size or heating rate.

5.1.4 Interpretation and Presentation of DTA

There are difficult with the measurement of transition temperatures using DTA curves. The onset of the DTA peak in principle gives the start-temperature, but there may be temperature lags depending on the location of the thermocouple with respect to the reference and test samples or the DTA block. It is wise to calibrate the apparatus with materials of precisely known melting points. The peak area (A), which is related to enthalpy changes in the test sample, is that enclosed between the peak and the interpolated baseline. When the differential thermocouples are in thermal, but not in physical contact with the test and reference materials, it can be shown that A is given by,

$$A = \frac{mq}{gk} \quad , \tag{5.1}$$

where m is the sample mass, q is the enthalpy change per unit mass, g is a measured shape factor and k is the thermal conductivity of sample.

With porous, compacted or heaped samples, the gas filling the pores can alter the thermal conductivity of the atmosphere surrounding the DTA container and lead to large errors in the peak area. The situation is made worse when gases are evolved from the sample, making the thermal conductivity of the DTA-cell environment different from that used in calibration experiments. The DTA apparatus is calibrated for enthalpy by measuring peak areas on standard samples over specified temperature ranges. The calibration should be based upon at least two different samples, conducting both heating and cooling experiments.

In the present work, SEIKO TG/DTA 6300 has been used for thermal analysis. The TG/DTA is a simultaneous measurement instrument combining TG, which utilizes a horizontal differential type balance beam, with the highly flexible DTA feature. This instrument is used for reaction velocity and acceleration

degradation tests, as well as analysis of the water and ash content in samples, and evaluation of decomposition, oxidation and heat resistance of samples.

The features are:

(i)   As a forerunner in the balance beam mechanism, this instrument utilizes a horizontal differential type balance beam. The lightweight structure of the balance beam mechanism provides the following strong points: stability in regards to temperature fluctuations, buoyancy reduction and highly sensitive balance, as well as the ability of the differential balance to deal with disturbances such as oscillation.

(ii) Through the utilization of an automatic cooling unit, the instrument is now automatically cooled to a set temperature after measurements, which raises the effectiveness of measurements.

(iii) As with the DSC, the auto sampler is easily attached to the TG/DTA.

Temperature range is ambient to 1773 K; balance method is horizontal differential type; TG measurement range is ± 200 mg; DTA measurement range is ± 1000 µV; program rate is 0.01 to 100 K/min; gas flow rate is 0 to 1000 ml/min; cooling rate is less than 15 minutes from 1273 to 323 K.

5.2   X-ray Diffraction (XRD)

The German Physicist Wilhelm Roentgen discovered X-rays in 1895. X-rays are electromagnetic waves of short wavelengths in the range of 10^{-2} to 10^2 Å. Unlike ordinary light, these rays are invisible, but they travel in straight lines and affect photographic film in the same way as light. On the other hand, they were much more penetrating than light and could easily pass through the human body, wood, quite thick pieces of metal and other "opaque" objects.

The XRD provides substantial of information on the crystal structure. XRD is one of the oldest and effective tools for the determination of the atomic arrangement in a crystal. The wavelength (1Å) of an X-ray is the same order of magnitude as the lattice constant of crystals and it is this which makes X-rays so useful in structural

49

analysis of crystal. When ever X-rays are incident on a crystal surface, they are reflected from it. The reflection abides by the Bragg's Law as given below

$$2d \sin \theta = n\lambda ,$$ (5.2)

where d is the distance between crystal plane, θ is the incident angle, λ is the wavelength of the X-ray and n is a positive integer. Bragg's Law also suggested that the diffraction is only possible when $\lambda < 2d$.
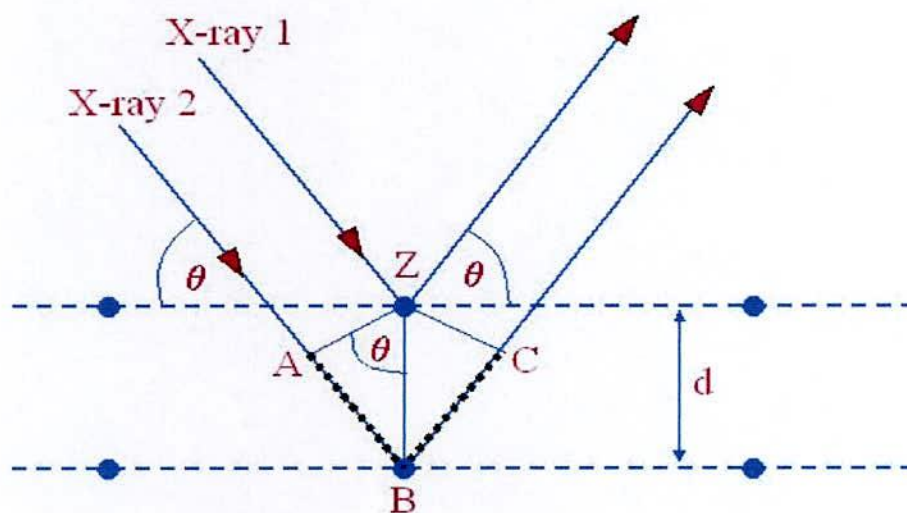
Fig. 5.3: Bragg's diffraction pattern.

X-ray diffractograms of all the samples were recorded using monochromatic Cu-K_α radiation ($\lambda = 1.54053$ Å) to ensure the formation of single-phase nature of the sintered product. XRD patterns information are: scanning speed 2°, chart speed 20 mm, starting from 25° and ending at 95°. Peak intensities are recorded corresponding to their 2θ values. The inter planner distance d was calculated from these 2θ values of the diffraction peaks using the Bragg's Law (In Fig. 5.3).

5.2.1 X-ray powder method

Powder method is perhaps the most widely used X-ray diffraction technique for characterizing materials. The term 'powder' really means that the crystalline domains are randomly oriented in the sample. Therefore, when the 2-D diffraction pattern is recorded, it shows concentric rings of scattering peaks corresponding to the various d spacing in the crystal lattice. The positions and the intensities of the peaks are used for identifying the underlying structure (or phase) of the material. Powder diffraction data can be collected using either transmission or reflection geometry, as shown in Fig. 5.4 below.
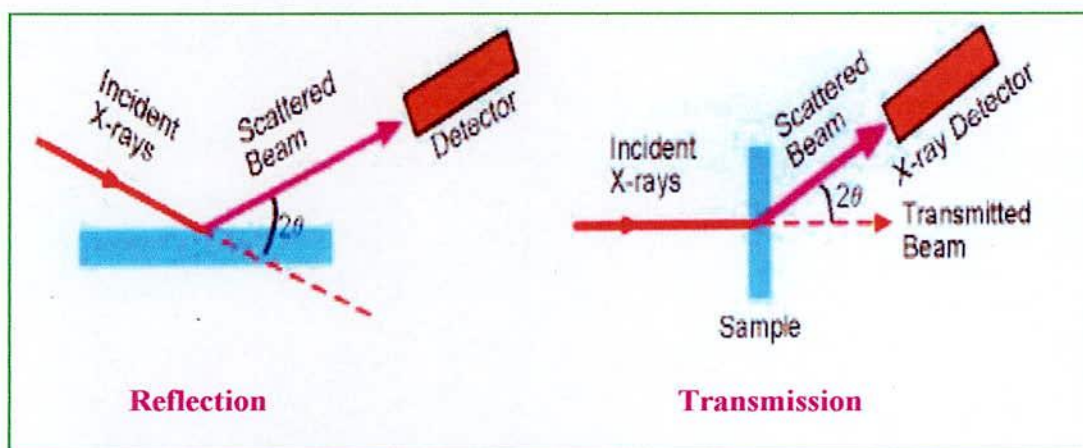
Fig. 5.4 Reflection and Transmission geometry of powder diffraction

Because the particles in the powder sample are randomly oriented, these two methods will yield the same data. Powder diffraction data are measured using the Philips X'PERT MPD diffractometer, which measures data in reflection mode and is used mostly with solid samples, or the custom built 4-circle diffractometer, which operates in transmission mode and is more suitable for liquid phase samples.

51

5.2.2 Experimental Technique for X-ray diffractometer

X-ray diffraction (XRD) is a versatile non-destructive analytical technique for identification and quantitative determination of various crystalline phases of powdered or solid samples of any compouned. For each set of composition, ribbons are cut into several pieces; each of length 20 mm. Heat treatment was performed on the amorphous ribbons using a naber muffle furnace, where each piece of ribbon was wrapped by aluminum foil separately. After heat treatment, samples were removed from the aluminum foil carefully and kept separately for XRD experiment. For XRD experiment each sample was set on a glass slids and fixed the sample by putting adhesive tape at the two ends of the sample.

After the pattern is obtained the value of 2θ is calculated for each diffraction line; set of 2θ values is the raw data for the determination of the lattice parameters of the unit cell. Fig. 5.5: Shows the block diagram of Phillips PW 3040 X'Pert PRO X-ray diffractometer.
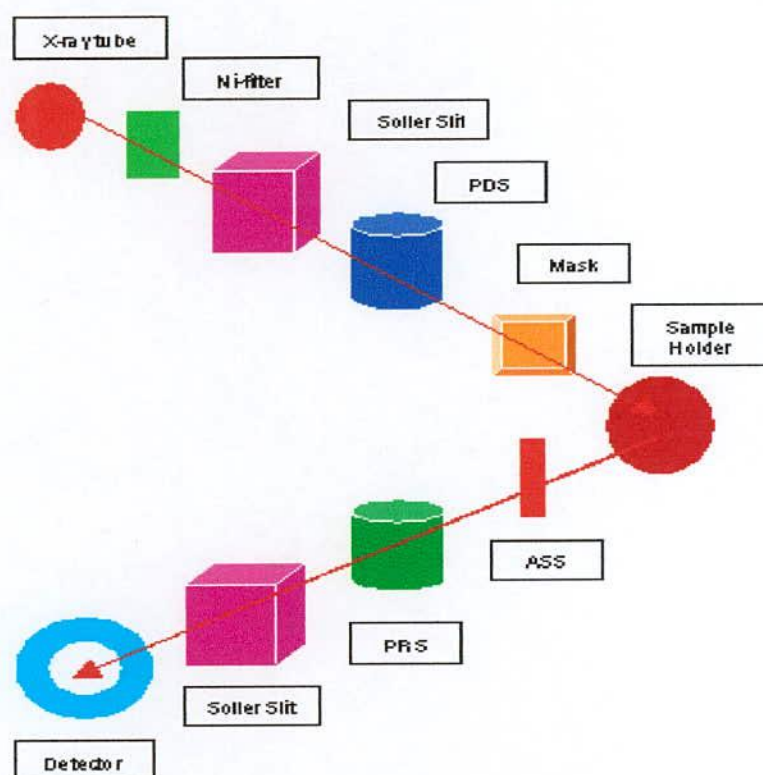
Fig. 5.5 Block diagram of the PHILIPS PW 3040 X'Pert PRO XRD system

A PHILIPS PW 3040 X'Pert PRO X-ray diffractometer was used for the lattice parameter determination in the Materials Science Division, Atomic Energy Centre, Dhaka. Fig. 5.6 shows the inside view of the X'Pert PRO XRD system. The X'Pert Pro diffraction system utilizes a modular system approach to provide performance for application ranging from routine characterization to in-depth research investigation. The powder diffraction technique was used with a primary beam power of 40 kV and 30 mA for Cu radiation. A nickel filter was used to reduce Cu-K$_\alpha$ radiation and finally Cu-K$_\alpha$ radiation was only used as the primary beam. A (θ- 2θ) scan was taken from $30°$ to $90°$ to get possible fundamental peaks of the sample with the sampling pitch of $0.02°$ and time for each step data collection was 1.0 sec. Both the programmable divergence and receiving slits were used to control the irradiated beam area and output intensity from the sample, respectively. An anti scatter slit was used just after the sample holder to reduce air scattering. Two solar slits were used just after the tube and in front of the detector to get parallel beam only. All the data of the samples were stored in the computer memory and later analyzed those using computer software "X PERT HIGHSCORE".
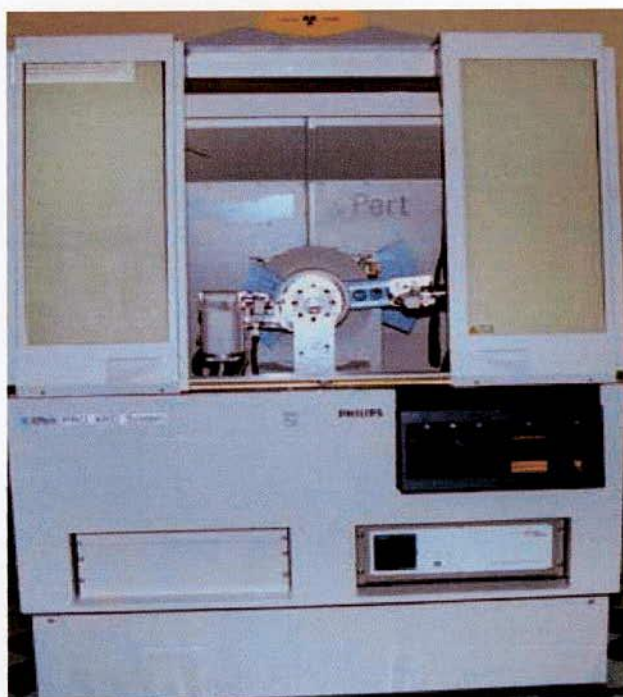
Fig.5.6 A Philips PW 3040 X'Pert PRO X-ray diffractometer

The Specifications of Philips X'Pert Pro Multipurpose X-ray Diffractometer systems are as follow:

- **X-ray Sources:** 3 kW Copper tube and 2 kW Cobalt tube
- **Optics:** Focussing and parallel PreFix optics, programmable slits, tunable diffracted beam monochromator.
- **Detectors:** Xe proportional counter and solid state X'cellerator
- **Sample stages:** Single sample holder, 15-sample changer, sample spinning capability
- **Variable temperature capability:** Anton-Paar 77 to 725 K and 300 to 1475 K cameras
- **Software and databases:** ICDD PDF-2 database (2002). Hi-Score search-match software, X'Pert Plus crystallographic analysis software with Rietveld capability, ProFit line profile analysis software.
- **Instrument statistics:** The system uses Cu-K_α radiation that has a wavelength of 1.54Å. Analysis are commonly run using a 40 kV 45mA X-ray tube voltage, a 0.04° solar slits, 1° divergence and antiscatter slits, and ½° (for powder) or ¼° (for clays) receiving slit.

5.2.3 Analysis of XRD data

The XRD data consisting of θ_{hkl} and d_{hkl} values corresponding to the different planes from which the following structural information of the nanocrystalline ribbon sample was evaluated.

(i)   Identification of phases
(ii)   Lattice parameter determination
(iii) Average grain size determination
(iv)   Si- content determination in nanograins

(i) Identification of phases

X-ray diffractometer has become a very popular and useful instrument for routine X-ray analysis of ribbon samples. In fact the diffractometer technique is often preferred to Debye-Scherrer technique owing to its several inherent merits. The most striking difference between the two methods is in the use of different intensity

54

detection and measuring devices. XRD pattern of as-cast indicates just amorphous pattern of said composition. The XRD patterns are identified as bcc α-Fe(Si) solid solution, which are developed on the amorphous ribbon after heat treatment. The peak pattern is observed for all the samples at different heat treatment temperatures indicating the bcc α-Fe(Si) phase, which is developed on amorphous ribbons after heat treatment. Present experiment revels that 450°C is not sufficient temperature to start forming of crystalline nanograins of bcc Fe(Si) on the amorphous ribbon of the studied alloy composition.

(ii) Lattice Parameter Determination

Lattice parameter of crystalline bcc Fe-Si nanograins has been determined for all the two different amorphous compositions at different heat treatment temperatures. Normally, lattice parameter of an alloy composition is determined by the Debye-Scherrer method after extrapolation of the curve. In this method, at least five fundamental reflections are required to determine lattice parameter. In the present case, only one reflection (110) is prominent in all XRD patterns and we would like to understand how the value of lattice parameter changes with annealing temperature. We have, therefore, determined the lattice parameter using only that particular reflection using equation $2d\sin\theta = \lambda$ and $a_0 = d\sqrt{2}$, where $\lambda = 1.54178\,\text{Å}$ for $Cu - K_\alpha$ radiation and a_0 is the determined lattice parameter within an error estimated to be $\pm 0.0001\,\text{Å}$.

(iii) Grain Size Determination

The main aim (vital point) of the present study is to determine the nanocrystalline grain size for all the heat treated samples of the alloy composition by using Scherrer method. The XRD pattern of (110) reflection for different steps of heat treatment temperature of the alloy composition is used to calculate grain size. Grain size is determined using the following formula,

$$D_g = \frac{0.9\lambda}{\beta\cos\theta},$$
(5.3)

where $\lambda = 1.54178 \text{Å}$ for $Cu - K_\alpha$ radiation and β = FWHM (full width at half maximum) of the peak in radian. Considering β in degree we get the following relation

$$D_g = \frac{79.5}{\beta \cos \theta} \qquad (5.4)$$

All the values of grain size for every steps of heat treatment temperature of the alloy composition were determined. The FWHM of the peak is large at the early heat treatment temperature and with the increase of heat treatment temperature the value of FWHM becomes smaller which means that the grain size is increasing gradually.

(iv) Si-content in Nanograins

Crystalline nanograins were formed on the amorphous matrix of the ribbon in the process of heat treatment having the composition of Fe-Si. It is, therefore important to determine the concentration of Fe and Si in the nanograin. As because the alloy consists of Fe and Si and we have experimentally determined the lattice parameter of the alloy nanograin for the two compositions at different temperatures. It is easy to calculate the Si content in the nanograins from the data of Pearsons who was established the relationship between the lattice parameter as dependent on Si content in Fe-Si alloys covering a wide range of composition [5.2]. From the relationship, we have constructed a simple equation to calculate Si content from lattice parameter. The equation is

$$X = \frac{(a_0 - 2.8812)}{0.0022}, \qquad (5.5)$$

where X is at.% Si in the nanograins, a_0 is the determined lattice parameter of nanograins. Si-contents for the nanograins develop during the isothermal annealing at various temperatures have been calculated.

5.3   Thermal Treatment of the amorphous ribbon

In order to study nanocrystallization behavior by XRD and magnetic properties upon evaluation of nanocrystalline phase on amorphous matrix thermal treatment i.e. annealing is required to perform. For XRD, as prepared amorphous ribbon were cut into small pieces of about 2 cm lengths and for magnetic measurement such as permeability toroidal core were wound for annealing treatment. A laboratory built vacuum system made by quartz tube capable of evaluating up to 10^{-5} torr was used for their purpose. The samples were put into the quartz tube and evaluated (10^{-5} torr) before it had been put inside the tabular furnace heated to a present temperature and kept for the time required to complete the annealing. In this way all the isothermal annealing as a function of time were performed.

5.4   Impedance Analyzer

The Hewlett Packard 4192A LF Impedance Analyzer can measure eleven impedance parameters absolute value of impedance ($|Z|$), absolute value of admittance ($|Y|$), phase angle (θ), resistance (R), reactance (X), conductance (G), susceptance (B), inductance (L), capacitance (C), dissipation factor (D) and quality factor (Q). Measurement range of $|Z|$/R/X is 0.1 mΩ; to 1.2999 MΩ; $|Y|$/G/B is 1ns to 12.999s; θ is -180.00° to +180.00°; L is 0.01 mH to 1.000 kH; C is 0.1 pF to 100.0 mF; D is 0.0001 to 19.999; Q is 0.1 to 1999.9. All have a basic accuracy of 0.1% and resolution of $4^{1/2}$ digits. Number of display digits dependence on measuring frequency and OSC level setting.

The 4192A can provide measuring frequency, OSC level, and dc bias voltage equivalent to actual operating conditions. The sweep capabilities of the built-in frequency synthesizer and dc bias source permits quick and accurate measurements. The built- in frequency synthesizer can be set to measuring frequency within the range from 5 Hz to 13 MHz with 1 mHz maximum resolution. OSC level is variable from 5 mV to 1.1 Vrms with 1 mV resolution. The internal dc bias voltage source provides ± 35 V in 10 mV increments. Measuring frequency or dc bias voltage can be automatically or manually swept in either direction. OSC level can be manually swept

in either direction in 1 mV increments (5 mV for levels above 100 mV). Actual test voltage across or test signal current through the device under test is also measured. Thus the 4192A can evaluate components and circuits under a wide variety of measurements conditions.

5.4.1 Preparation of the Samples for Complex Permeability Measurement

The amorphous ribbon were wound into toroidal having outer and inner diameters 13 to 15 mm and with the ratio of outer and inner diameters always kept less than 1.2 in order to improve the homogeneity of the applied field, as also to reduce the possibility of an inhomogeneous inductance response. Toroids were wound with 5 turns around to apply AC magnetic fields over a wide range of amplitudes. While measuring the permeability of the amorphous ribbon cores at high frequency, the high electric resistance of these materials generally precludes the trouble some skin effect found in ribbons. However, the cross-section of the amorphous ribbon core to be measured may have to be kept small in order to avoid dimensional resonance phenomena. To avoid an increase in resistance owing to skin effect, braided copper wire is used at frequencies higher than 100 kHz.

At higher frequencies the capacitance arising from winding gives inaccurate values of R and L_s. It is, there fore, necessary to keep the capacitance of the winding as low as possible. Frequency response characteristics were then investigated on these ring shaped specimens as a function of frequency.

5.4.2 Components of Complex Permeability Measurements

The real (μ') and imaginary (μ'') part of the complex permeability of the as-cast and annealed ribbons were measured as a function of frequency using the Hewlett Packward 4192A LF Impedance Analyzer, Atomic Energy Centre, Dhaka. From the frequency dependence of complex permeability, evolution of permeability and magnetic loss component at different stages of nanocrystallization as affected by thermal treatment at different temperatures was determined using toroids prepared from the ribbons wound with insulating Cu wire.

58

The HP 4192 A impedance analyzer directly measure the value of inductance, L and loss factor,

$$D = \tan \delta \qquad (5.6)$$

From inductance the value of real part of complex permeability, μ' can be obtained by using the relation

$$\mu' = \frac{L}{L_0} \qquad (5.7)$$

Here, L is the inductance of the toroid and L_0 is the inductance of the coil of same geometric shape in vacuum. L_0 is determined by using the relation

$$L_0 = \frac{\mu_0 N^2 S}{\pi d} \qquad (5.8)$$

Where S = $\frac{m}{\pi \rho d}$, μ_0 is the permeability of the vacuum, m is the mass of the sample, N is the number of turns, S is the cross-sectional area of the toroid, d is the average diameter and ρ is the density of the material. The imaginary part of complex initial permeability can be determined by using the relation,

$$\tan \delta = \frac{\mu''}{\mu'} \qquad (5.9)$$

and the relative loss factor is calculated with the relation $\frac{\tan \delta}{\mu'}$

5.5   Curie Temperature Measurements

Curie temperature, T_c, is the most important parameter of magnetic materials. The magnetic properties and magnetic structures are effectively changed within the Curie temperature. Curie temperature provides substantial information on magnetic states of substances in respect of the strength of exchange interaction. So the determination of Curie temperature accurately is of great importance. Curie temperature can be determined from the temperature dependence of permeability, temperature dependence of magnetization curve and Arrott plot. Sometimes an operational procedure needs to be adopted for the determination of T_c. A standard procedure for determination T_c in ferromagnetic materials is based on symmetry principle. Arrott [5.3], Belov [5.4], and Kouvel [5.5] have pioneered the use of

classical form of expression for magnetization and field near a ferromagnetic phase transition.

Temperature dependence of the initial permeability of the as-cast and annealed ribbons have been measured using a laboratory built furnace and Wayne Kerr 3255 B inductance meter with continuous heating rate of $\approx$ 5 K / min with very low applied ac field of $\approx 10^{-3}$ Oe. From this measurement, T_c of the as-cast and annealed samples have been determined. In addition to the measurement of T_c, temperature dependence of initial permeability at different stages of crystallization has been studied for Fe-Cu-Nb-Si-B soft nanocrystalline magnetic materials.

5.5.1 Inductance Analyzer

The 3255B Precision Magnetics Analyzer provides 2-terminal measurement of inductors and transformers over the frequency range 20 Hz to 500 kHz. DC resistance measurements are performed at a drive level of 100 mV. The drive level for AC measurements can be varied from 1 mV to 10 V rms. Automatic level control (ALC) can maintain the drive level at the component. During AC measurements the 3255B can supply a DC bias current which is variable between 1 mA and 1 A and when used with external 3265B DC bias units, up to 125 A DC bias current is available.
The analyzer's measurement, display and control facilities include:
- Spot frequency measurements;
- Multi-frequency measurements at a number of user-defined frequencies;
- Display of actual measurement values;
- Output of measurement results to an Epson-compatible printer;
- Strong of components into bias according to their measured value and/or minor term (option)

All the above functions can be selected via manual front panel control or remote control via the GPIB interface for fully-automated high-speed testing. Self calibration is performed to set calibration constants for signal processing elements in the measurement hardware and signal generation system, and to compensate for components, which drifted with time. To maintain full specified accuracy it should be

run at least every three months. To measure the inductance of a component the analyzer should be powered up with the test leads or fixture connected to the font panel BNC connectors. The analyzer should be operated in Measurement Mode. The component to be measured is connected to the test leads or fixture. The measurement may be performed as single short mode for single measurement or repetitive mode for continuous measurement.

5.6 Magnetization Measurement

Magnetization is defined as the magnetic moment per unit volume or mass of the substance. There are various ways of measuring magnetization of a substance. In the present thesis magnetization has been measured by using a Vibrating Sample Magnetometer (VSM) at room temperature, applying a wide range of magnetic field from $-800,000$ Am^{-1} to $+800,000$ Am^{-1}.

These measurements were carried out at Atomic Energy Research Institute, Savar. We use Hirst VSM 02 which is an automatic Vibrating Sample Magnetometer for characterization of soft and hard magnetic materials manufactured by HIRST Magnetic Instruments Ltd. A block diagram of a typical VSM system is shown in Fig. 5.7. The Hirst VSM system arrangement is shown in the Fig 5.8. The vibration and measuring unit of Hirst VSM is shown in Fig. 5.9.

5.6.1 Principle of Vibrating Sample Magnetometer

Vibrating Sample Magnetometer developed by S. Foner [5.6-5.7] is a versatile and sensitive method of measuring magnetic properties and is based on the flux change in a coil when the sample is vibrated near it. The VSM is an instrument designed to continuously measure the magnetic properties of materials as a function of temperature and field. In this type of magnetometer, the sample is vibrated up and down in a region surrounded by several pickup coils. The magnetic sample is thus acting as a time-changing magnetic flux, varying inside a particular region of fixed area. From Maxwell's Law it is known that a time varying magnetic flux is accompanied by an electric field and the field induces a voltage in pickup coils. This

alternating voltage signal is processed by a control unit system, in order to increase the signal to noise ratio. The result is a measure of the magnetization of the sample.

5.6.2 Description and brief working principle of Hirst VSM02

Vibrating Sample Magnetometers, as the name implies, Vibrate the sample as part of the measurement process. This provides the Flux meter element of the system with the dynamic component which it requires to make the measurement. The applied field is changed so, at each measurement point the field is static and hence no eddy currents to cause problems.

The object when using a VSM or any other type of magnetic characterization of the magnetization (J) on the applied field H > J (H). Once this is obtained, many useful parameters can be extracted from the data. VSM typically generate the applied field (H) using an electromagnet or a super conducting solenoid for fields greater than 2.5-3 Tesla. The magnetic driven around its hysteresis curve by changing the applied field (H) and the J signal is determined.
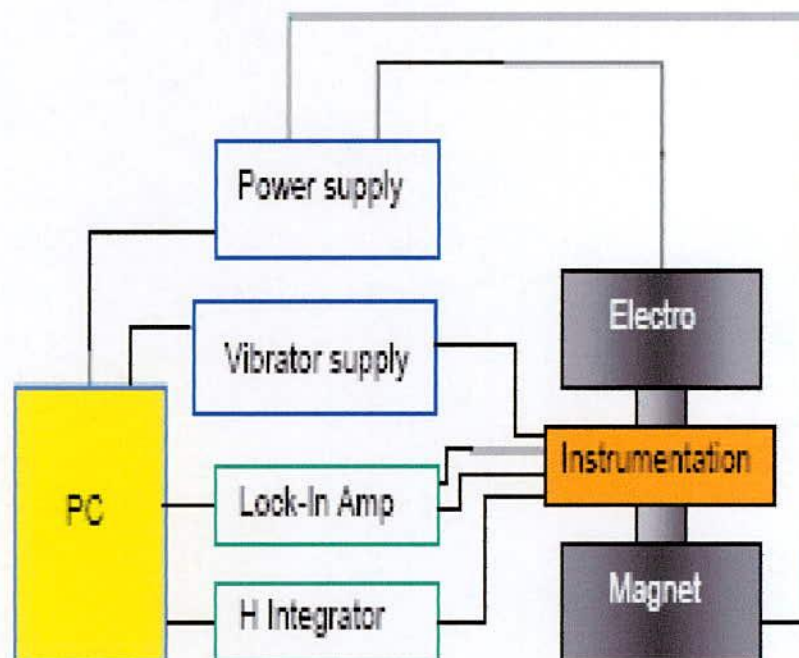
Fig. 5.7 Block diagram of a VSM system

Fig. 5.8 Hirst VSM system arrangements
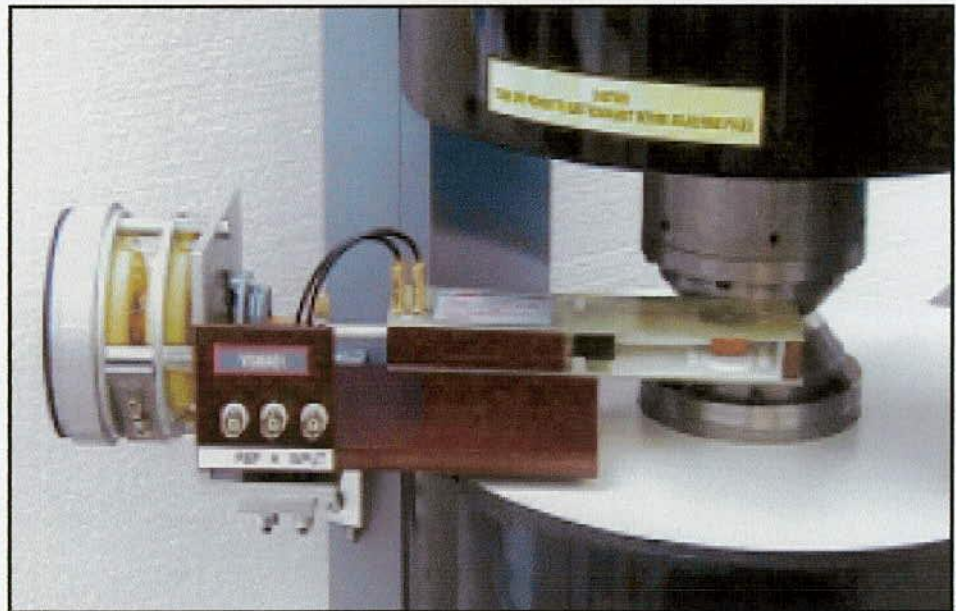
Fig. 5.9 Vibration and measurement unit

In the VSM02 a conventional electromagnet is implemented with two independent coils driven by independent 1000W amplifiers. The current control on the coils utilizes Tran's conductance to ensure that constant current is supplied for a particular demand and to ensure that resistive changes due to heading do not cause the measurement to drift. The applied field (H) is measured using a hall element connected to a Guan meter (BGMOI).

The magnetization field (J) is determined by utilizing pick up coils. As with large iron poles and light inductances d is impossible to change the field quickly without causing unwanted effects. VSM measurements are a quasi-static process where the samples J field is determined when the applied field is static. As the applied is static when J is determined, the J magnetization field is also static. Pick up coil work by Faradays Law of induction. Where e is the voltage induced, d theta is the change in magnetic flux in time t. As the J field is static there is no d-theta so a pick up coil cannot work. To overcome this problem the sample is vibrated using a sinusoidal oscillation. This vibration generates the required change in flux with respect to final and produces a signal from the pickup coils.

As the sample is vibrating at a known frequency with known phase it is possible to use a lock in amplifier to extract the J value from the pick up coils output. This is also has huge advantages as lock-in amplifiers can discriminate against noise and pick out a finy signal buried in noise. This gives VSM's the potential to have huge gain on the J measurement channel. In the VSM 02 the maximum J gain is approximately X 1,300,000. This allows very small samples, or samples with a small magnetic moment to be measured such as thin-films powders and inks.

CHAPTER – 6

RESULTS AND DISCUSSION

Results and Discussion

6.1 Differential Thermal Analysis of the samples

Calorimetric studies of amorphous alloys provide substantial fundamental information concerning the kinetics of crystallization and structural relaxation effects. The kinetics of the on set of crystallization has been studied calorimetrically by Clements and Cantor [6.1] and both calorimetrically and magnetically by Luborsky [6.2] in a variety of amorphous magnetic alloys.

If the amorphous alloy is to be used as a precursor for the production of nanocrystalline FINEMET of composition Fe-Cu-Nb-B-Si then the primary and secondary crystallization temperatures are of importance. Because the structure of the beneficial ferromagnetic nanocrystalline phase is composed of Fe(Si), which is the product of primary crystallization. The secondary crystallization product is the Fe-B phase. This phase is detrimental for the soft magnetic properties because of its high anisotropy energy.

The change of composition affects the growth kinetics in a complicated way, which can only be determined experimentally. The composition of the alloy affects both the primary and secondary crystallization phases, because the time needed for the constituent atom to have long-range order depends on their bond energies [6.3-6.4]. Good soft magnetic properties of the materials require not only small grain size but at the same time the absence of boron compound. The separation between the primary crystallization of bcc Fe(Si) and the secondary crystallization product of Fe-B compounds not only is determined by the Cu and Nb additions but also on boron content. With the increase of boron content the separation between the two products decreases [6.5]. We kept at a moderate level of boron content in the nominal composition in order to obtain an optimum nanoscaled structure.

In the present investigation DTA technique has been used to study the crystallization behavior of nanocrystalline alloys $Fe_{75.5}Cu_1Nb_1Si_{13.5}B_9$ (sample-A)

and $Fe_{74} Cu_{0.5} Nb_3 Si_{13.5} B_9$ (sample-B). DTA is a direct and effective technique for analyzing the kinetics of crystallization of amorphous materials.

6.1.1 DTA Results of Nanocrystalline amorphous ribbon Fe-Cu-Nb-Si-B as Affected by Cu and Nb

DTA trace of as-cast amorphous ribbons, sample-A and sample-B, are recorded in a nitrogen atmosphere with a heating rate of 20°C/min which are presented in Fig. 6.1 and Fig. 6.2 respectively. Two exothermic peaks are distinctly observed which correspond to two different crystallization events at temperatures T_{x_1} (primary crystallization) and T_{x_2} (secondary crystallization) respectively for both the samples. The soft magnetic properties correspond to the T_{x_1} of α-Fe (Si) phase. T_{x_2} corresponds to Fe-B phase, which causes magnetic hardening of the nanocrystalline alloy. Phase identification cannot be done from a DTA scan. XRD has been used for the identification of phases and would be discussed later on. From Fig. 6.1 and Fig. 6.2, onset (initiation) of primary and secondary crystallization temperatures T_{x_1} and T_{x_2} and the corresponding crystallization peak temperatures T_{p_1} and T_{p_2} for the sample-A and sample-B, have been determined and are shown in Table-6.1. It is clear from the data of crystallization that the crystallization temperatures for the two studied samples A and B are different.

The crystallization onset temperatures (T_{x_1} and T_{x_2}) and peak temperatures (T_{p_1} and T_{p_2}) for the sample-A is much lower than those of sample-B. Both the samples display exothermic peak, i.e. release of heat during the crystallization of Fe(Si) and Fe-B phases since the transition from amorphous solid to crystalline solid is an exothermic process. From the DTA data it is also understood that the temperature difference between the two crystallization processes is smaller for the sample-A (ΔT = 87°C) as compared with the sample-B (ΔT = 120°C). This large difference is due to higher Nb content in sample-B, which influences the shift of T_{p_2} to higher temperature. The early onset of primary crystallization temperature, T_{x_1} at

470°C of sample-A compared with that of T_{x_1} = 504°C for the sample-B can be explained as due to larger amount of Cu = 1 at. %. The decrease of the onset temperature for the first crystallization stage reflects the local clustering of Cu-atoms which obviously lowers the configurational energy of the subcritical nucleus [6.6]. The effect of copper in enhancing the nucleation density is really noteworthy. It has already been demonstrated that T_{x_1} for primary crystallization of Finemet shifted to much higher temperature when copper was absent and / or less amount [6.5].

Since Cu helps nucleation of Fe(Si) phase and Nb delays the formation of boride phase [6.7], the observed anomalies of crystallization temperatures in this studied samples are clearly understood from their compositional variation of Cu and Nb. This is to note that the whole process of crystallization takes place over a wide range of temperatures. For example, sample-A, crystallization starts at T_{x_1} = 470°C and completed at T = 500°C. This signifies that the nucleation and growth of crystallites are faster in the initial stage of crystallization, which gradually becomes sluggish with the increase of volume fraction of crystallites.

Table-6.1: Onset temperature of primary and secondary crystallization temperature, T_{x_1} Fe(Si) and T_{x_2} (boride phase), peak crystallization temperatures T_{p_1} Fe(Si) and T_{p_2} (boride phase) during continuous heating with heating rate 20°C/min

Sample	Onset Temp. of primary crystallization T_{x_1} °C	Primary crys. peak Temperature T_{p_1} °C	Onset Temp. of secondary crystallization T_{x_2} °C	Secondary crys. peak Temperature T_{p_2} °C	(ΔT) $T_{p_2} - T_{p_1}$ in °C
$Fe_{75.5}Cu_1$ $Nb_1Si_{13.5}B_9$	470	482	558	569	87
$Fe_{74}Cu_{0.5}$ $Nb_3Si_{13.5}B_9$	504	521	629	641	120
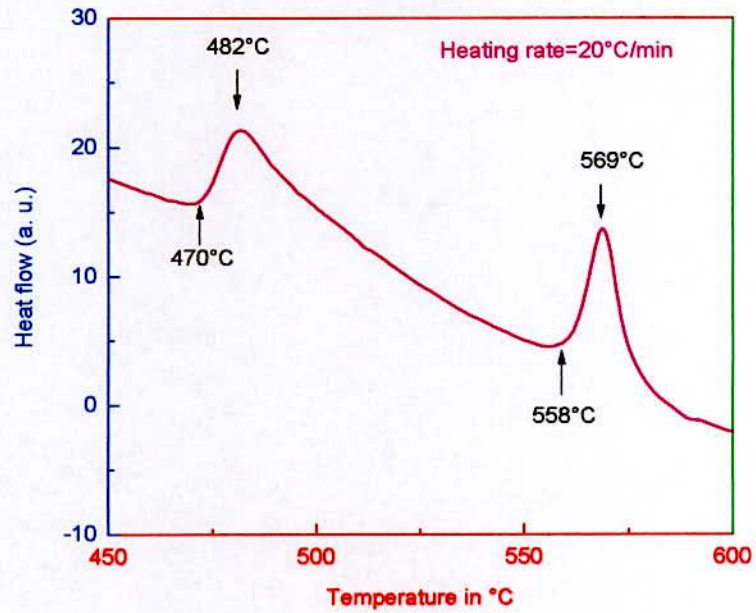
Fig. 6.1 DTA trace of the as-cast amorphous ribbon with composition $Fe_{75.5} Cu_1 Nb_1$ $Si_{13.5} B_9$ alloy (sample-A) with continuous heating
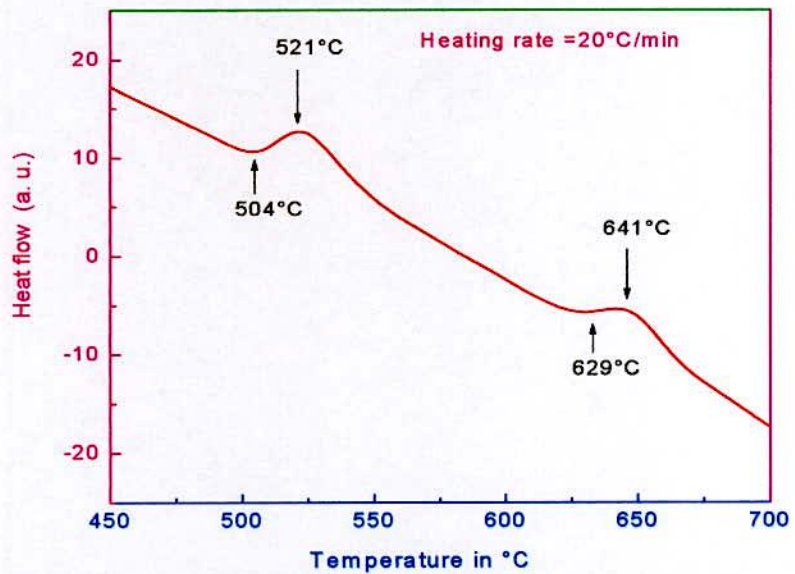
Fig. 6.2 DTA trace of the as-cast amorphous ribbon with composition $Fe_{74} Cu_{0.5} Nb_3$ $Si_{13.5} B_9$ alloy (sample-B) with continuous heating

The growth of crystallites involves diverse processes due to which the exothermic peaks are asymmetric as affected by various growth rates. As Cu helps nucleation and growth of crystallites, the exothermic peak with less copper (Cu = 0.5 at. %) is more asymmetric than that of sample-A (Cu = 1 at. %). Therefore the role of Cu on the crystallization behavior in these two studied samples is well understood.

6.1.2 Annealing effects on the kinetics of structural relaxation of Fe-Cu-Nb-Si-B nanocrystalline amorphous ribbons studied by DTA

Fig. 6.3 and Fig. 6.4 show the DTA traces of $Fe_{75.5}Cu_1Nb_1Si_{13.5}B_9$ (sample-A) alloy and $Fe_{74}Cu_{0.5}Nb_3Si_{13.5}B_9$ (sample-B) alloy in the as-cast state and annealed at different temperatures for 30 min with heating rate of 20°C/min.

It is observed from the DTA scan that the onset temperature for the sample- A annealed at $T_a = 450°C$ is almost unchanged with respect to its amorphous precursor which is quite logical since $T_a = 450°C$ is still lower than its $T_{x_1} = 470°C$. But the same sample when annealed at $T_a = 475°C$ which is slightly higher than the onset of crystallization temperature of $T_{x_1} = 470°C$, the primary crystallization peak has diminished to large extend and display quite diffused character which signifies that the substantial amount of crystallization has already be taken place.

The area under the first peak of DTA curve corresponds to the crystallization enthalpy, ΔH of Fe(Si) from which the volume fraction of crystallization (X_f) can be estimated according to the formula,

$$X_f = \frac{\Delta H_a - \Delta H_t}{\Delta H_a} \qquad (6.1)$$

where ΔH_a and ΔH_t are the crystallization enthalpy of the as-cast alloy and that of the alloy annealed for a time t, respectively.
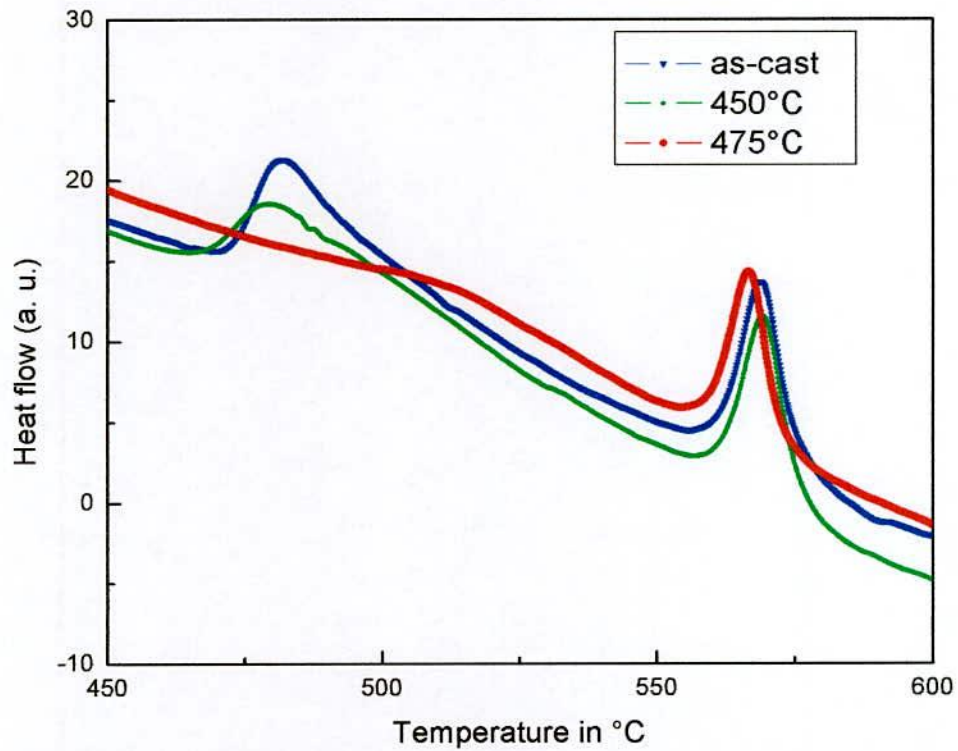
69

Fig. 6.3 Effects on DTA traces of as-cast and different annealing time on the nanocrystalline amorphous ribbon with composition $Fe_{75.5}Cu_1Nb_1Si_{13.5}B_9$
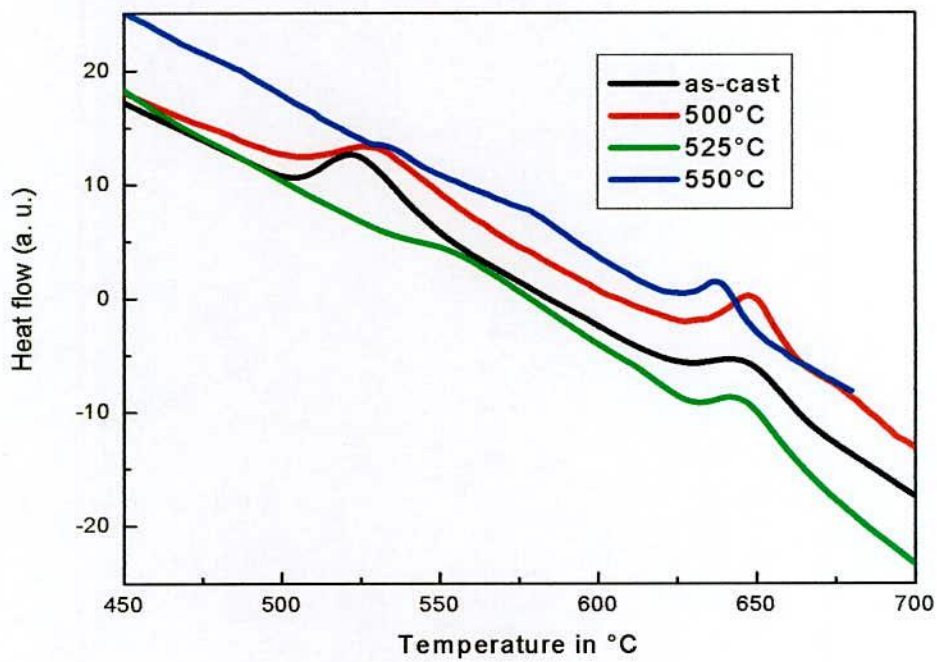

Fig. 6.4 Effects on DTA traces of as-cast and different annealing temperature on the nanocrystalline amorphous ribbon with composition $Fe_{74}Cu_{0.5}Nb_3Si_{13.5}B_9$

This shows that with increasing annealing temperature X_f is expected to increase. The effect of annealing temperature T_a on the secondary crystallization is insignificant since the T_a is very low compared to T_{x_2}. Similar situation is observed for sample-B. As-cast and annealed samples at $T_a = 500°C$ do not show any significant change of area under the 1st peak corresponding to the crystallization enthalpy, ΔH of Fe(Si). This means that at $T_a = 500°C$, no crystallization occurred which is quite obvious since $T_{x_1} = 504°C$ for this sample. This demonstrates that even annealing at $T_a = 500°C$, the material still remained amorphous.

Therefore crystallization enthalpy ΔH (area under the peak) is almost equal to that of, its amorphous state. But when annealed at $T_a = 525°C$, there is a broad diffused 1st peak meaning that substantial amount of primary crystallization, Fe(Si) has already been completed for 30 minutes at $T_a = 525°C$. For $T_a = 550°C$, 1st DTA peak is almost not visible, i.e. crystallization of Fe(Si) phase has almost completed. A critical scrutiny of 2nd peak does not show any significant change. The reason for such evidence has just bean explained earlier. The results of DTA scan on annealing of both the samples together with as-cast sample with the parameter such as T_{x_1}, T_{x_2}, T_{p_1}, T_{p_2} and ΔT are depicted in Table-6.2 and Table-6.3.

It is observed from the tables that the T_{x_1}, T_{x_2}, T_{p_1}, T_{p_2} as well as the difference between the two crystallization events are almost not affected by annealing, just below the crystallization temperatures. When the samples are annealed above the T_{p_1}, the primary crystallization as evidenced from their DTA curves are so diffused and smeared that they give signals of nearly completion of the primary crystallization of Fe(Si) crystallites. Therefore no characteristic temperatures in this range could be determined.

Table-6.2: Annealing effects on 1st and 2nd crystallization states of the nanocrystalline amorphous ribbon with composition $Fe_{75.5}Cu_1Nb_1Si_{13.5}B_9$ at constant heating rate 20°C/min

Annealing Temperature	Onset Temp. of primary crystallization T_{x_1} °C	Primary crys. peak Temperature T_{p_1} °C	Onset Temp. of secondary crystallization T_{x_2} °C	Secondary crys. peak Temperature T_{p_2} °C	(ΔT) $T_{p_2} - T_{p_1}$ in °C
As-cast	470	482	558	569	87
450°C	468	480	557	569	89
475°C	–	–	554	566	–

Table-6.3: Annealing effects on 1st and 2nd crystallization states of the nanocrystalline amorphous ribbon with composition $Fe_{74}Cu_{0.5}Nb_3Si_{13.5}B_9$ at constant heating rate 20°C/min

Annealing Temperature	Onset Temp. of primary crystallization T_{x_1} °C	Primary crys. peak Temperature T_{p_1} °C	Onset Temp. of secondary crystallization T_{x_2} °C	Secondary crys. peak Temperature T_{p_2} °C	(ΔT) $T_{p_2} - T_{p_1}$ in °C
As-cast	504	521	629	641	120
500°C	507	529	629	648	119
525°C	–	–	630	644	–
550°C	–	–	625	638	–

6.2 X-ray Diffraction Analysis

6.2.1 XRD Analysis of the Nanocrystalline ribbon with composition $Fe_{75.5} Cu_1 Nb_1 Si_{13.5} B_9$

In the present work, in order to study the crystallization onset temperature, X-ray diffraction spectra have been recorded for the nominal composition $Fe_{75.5} Cu_1 Nb_1 Si_{13.5} B_9$ annealed at 450°C to 700°C for 30 minutes. In Fig. 6.5, the XRD spectra of as-cast and annealed at 450°C to 700°C for 30 minutes have been presented. X-ray pattern of T_a = 475°C, clearly confirms the presence of crystalline phase identified as a bcc α-Fe(Si) solid solution developed in the amorphous matrix. In Fig. 6.5, the indices of the reflecting planes are shown in the parenthesis. XRD results indicate that no α-Fe phases are present in the alloys annealed at and below 450°C for 30 minutes with the appearance of a broader diffused pattern, which are characteristics of amorphous material.

Above 450°C it is clearly evident that crystallization starts with increasing annealing temperature peaks become narrower and sharper with higher intensity, which indicates that the crystallite sizes of bcc Fe(Si) are growing larger gradually. Three fundamental peaks (110), (200) and (211) at 2θ ≈ 45°, 65.5°and 83.4° correspond to bcc Fe(Si) phase. This is to be mentioned that no boride phase could be detected for the samples even annealed at T_a = 700°C. Generally boride phases are difficult to detect by X-ray as evidenced from numerous published research papers probably due to their small volume fraction.

Lattice parameters for all the annealed samples have been determined from (110) diffraction peak using formula $a_0 = d\sqrt{2}$, while grain size have been calculated using equation 4.15. The Si content in the nanograins has been calculated using the equation 5.5. Silicon content of the Fe(Si) nanograins was calculated from the established quantitative relationship between lattice parameter and Si-content in Fe-Si alloys by Bozorth [6.8]. All the results of θ, d-values, FWHM, a_0, D_g and Si-content from XRD analysis are listed in Table-6.4.
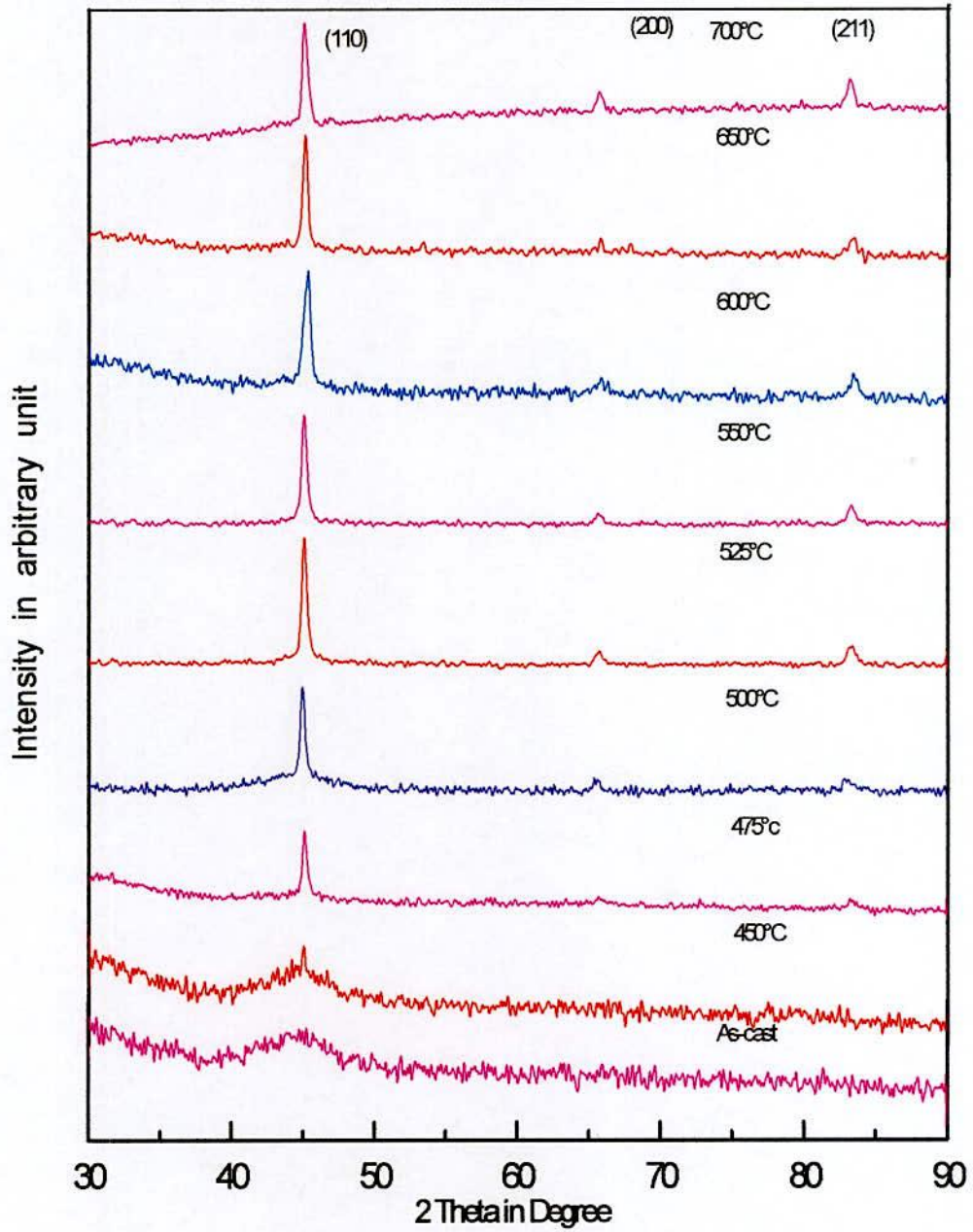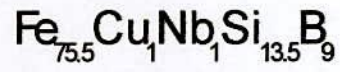
Fig. 6.5 XRD patterns of $Fe_{75.5} Cu_1 Nb_1 Si_{13.5} B_9$ alloys for as-cast and heat-treated at 450°C to 700°C for 30 minutes

Fig. 6.6 shows the variation of lattice parameter of Fe(Si) phase, Si-content and grain size of α-Fe(Si) phase with respect to the annealing temperature of the samples. With the increase of annealing temperature lattice parameter increases gradually. The lattice parameters of α-Fe(Si) phases are smaller than that of pure Fe, the value of which is 2.866Å.

It is also observed from the Fig. 6.6 and Table-6.4 that grain size increases with annealing temperature from a value of $D_g = 17$ nm for $T_a = 475°C$ to $D_g = 27$ nm for the sample annealed at $T_a = 700°C$ while Si-content decreases with T_a. This is contradictory to original Finemet alloy. Also a_0 increases with T_a which is also a similar contradiction. Such a situation may only be explained by assuming that at high temperature (T > 500°C) recrystallization of Fe(Si) grains takes place. Lower Nb content may also be the reason this deviation. The real cause is not clear and remains still an open question.

Fig.-6.6 Variation of grain size, lattice parameter and Si-content with annealing temperature for the nanocrystalline amorphous ribbon with composition $Fe_{75.5}Cu_1Nb_1Si_{13.5}B_9$

75

Table-6.4 Experimental XRD data of nanocrystalline $Fe_{75.5}Cu_1Nb_1Si_{13.5}B_9$ amorphous ribbon at different annealing temperatures
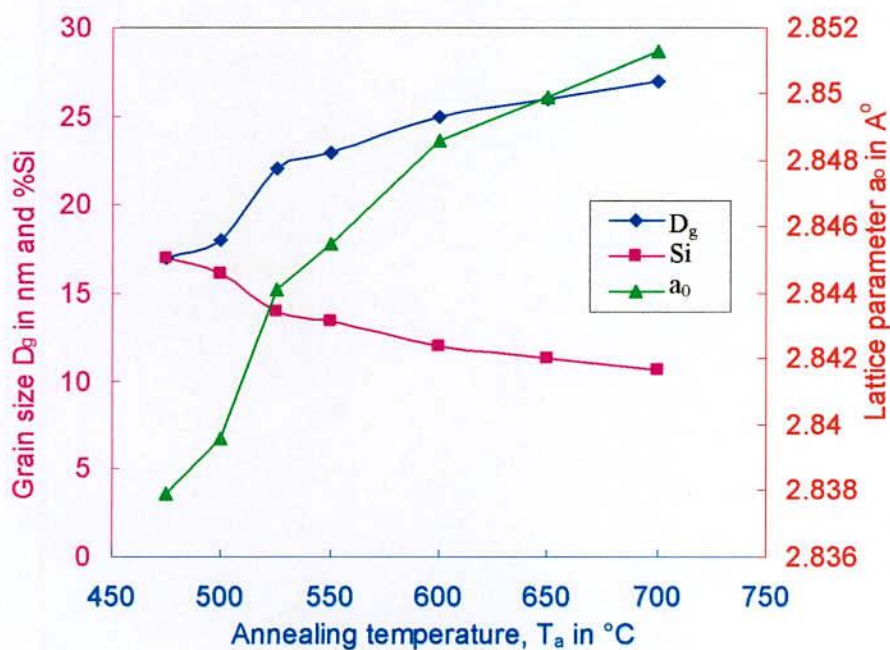
Temperature in °c	θ (°)	d (Å)	FWHM (°)	a_0 (Å)	D_g(nm)	Si (at %)
475	22.59	2.0066	0.53	2.8379	17	16.96
500	22.56	2.0110	0.52	2.8396	18	16.16
525	22.53	2.0111	0.46	2.8441	22	14.04
550	22.52	2.0121	0.43	2.8455	23	13.39
600	22.50	2.0143	0.40	2.8486	25	11.93
650	22.49	2.0152	0.38	2.8499	26	11.28
700	22.47	2.0162	0.37	2.8513	27	10.67

Enhancement of grain size with annealing temperature corresponds well with the reported results of Rubinstein *et al.* [6.9]. The formation of this particular nanostructure is ascribed to the combined effects of Cu and Nb and their low solubility in iron.

6.2.2 XRD Analysis of the nanocrystalline ribbon with composition Fe_{74} $Cu_{0.5}$ Nb_3 $Si_{13.5}$ B_9

Fig. 6.7 shows typical XRD patterns of the sample with composition $Fe_{74}Cu_{0.5}Nb_3Si_{13.5}B_9$ in the as-cast and after heat treatment (30 minutes) at different annealing temperatures. It is noticed that initiation of crystallization only takes place at T_a = 525°C. Below this annealing temperature no sharp peak indicating any crystallization event is noticed. The broad diffused peak around (110) plane necessarily signifies the amorphous state of the samples annealed at T_a = 500°C and below. XRD pattern clearly indicates the formation of bcc Fe(Si) phase above T_a = 525°C with the appearance of (110), (200) and (211) fundamental diffraction peaks. With the increasing of T_a, (110) diffraction peak becomes sharper which means that grains are growing bigger with the increase of annealing temperature.

From Fig. 6.7 it is observed that just below (110) peak, another diffraction line with small peak at $2\theta \approx 44°$ appeared for the samples annealed at $T_a = 650°C$ and 700°C. This diffraction line has been matched with $Fe_{23}B_6$ phase. Therefore the boride phase for this sample has appeared along with bcc Fe(Si).

The lattice parameter a_0, grain size D_g, and Si content of Fe(Si) nanograins have been calculated as in the case of sample-A and shown in Table-6.5. Similar trend like sample-A, i.e., a_0 and D_g increase with annealing temperature T_a, while Si-content of Fe(Si) phase decreases with T_a depicted in Fig. 6.8 similar interpretation applies in this case as for the sample-A. That means the increase of lattice parameter with subsequent decrease of Si-content in Fe(Si) phase is a case of recrystallization of α-Fe(Si) grains.
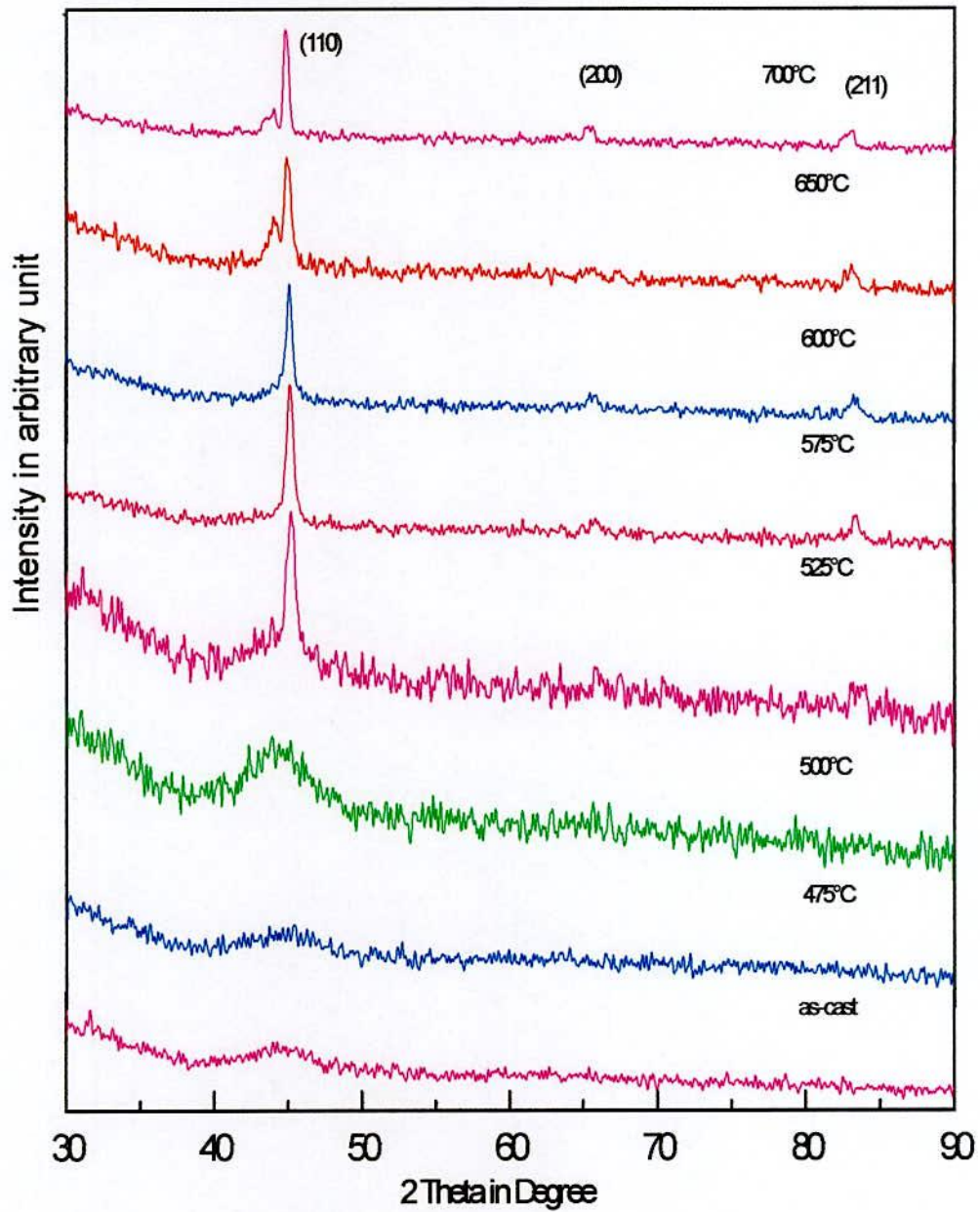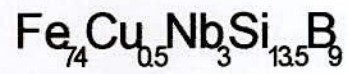
Fig. 6.7 XRD patterns of Fe_{74} $Cu_{0.5}$ Nb_3 $Si_{13.5}$ B_9 alloys for as-cast and heat-treated at 475°C to 700°C for 30 minutes

Table-6.5 Experimental XRD data of nanocrystalline $Fe_{74}\ Cu_{0.5}\ Nb_3\ Si_{13.5}\ B_9$ amorphous ribbon at different annealing temperatures

Temperature in °c	θ (°)	d (Å)	FWHM (°)	a_0 (Å)	D_g(nm)	Si (at %)
525	22.604	2.005	0.70	2.8363	13	17.68
550	22.577	2.007	0.59	2.8396	16	16.15
575	22.576	2.007	0.54	2.8396	18	16.12
600	22.547	2.010	0.46	2.8432	21	14.48
650	22.504	2.014	0.46	2.8482	21	12.10
700	22.443	2.019	0.44	2.8556	22	8.64
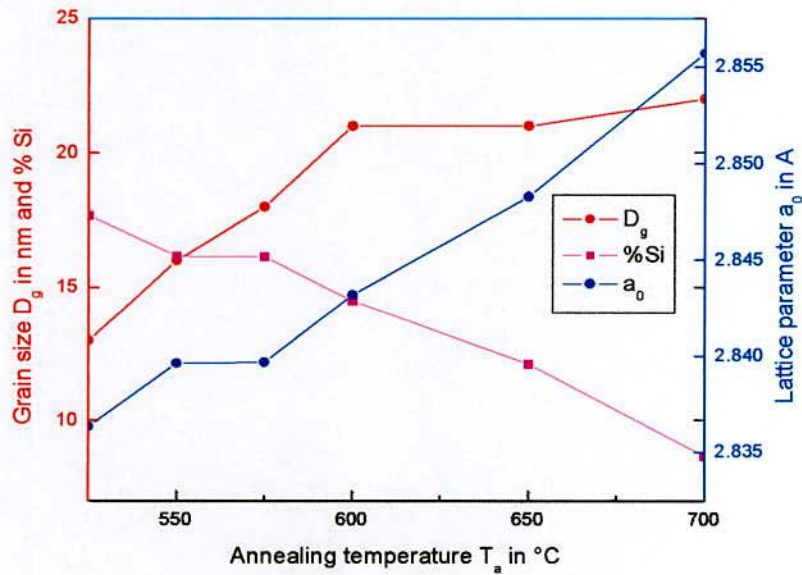
Fig.-6.8 Variation of D_g, a_0 and Si-content with T_a for the nanocrystalline amorphous ribbon with composition $Fe_{74}\ Cu_{0.5}\ Nb_3\ Si_{13.5}\ B_9$

79

6.3.1 Dynamic magnetic properties of $Fe_{75.5}Cu_1Nb_1Si_{13.5}B_9$ alloy with different annealing temperature

The dynamic magnetic measurement has been done on as-cast and also on samples annealed at 300°C to 600°C for 30 minutes at constant annealing time. In Fig. 6.9 (a,b,c), the real part of the complex initial permeability μ' up to f = 13000 kHz has been presented for as cast and annealed samples. The general characteristic of the curves is that μ' remains fairly constant and / or changes slightly up to a critical frequency characterized by the onset of resonance connected with the magnetic loss component.

Above the critical frequencies, μ' drops rapidly. The low frequency value of μ' generally increases with the increase of annealing temperature while the critical frequency decreases. In association with the higher value of low frequency permeability, the frequency at which resonance occurs appears at a lower frequency. This shows that the high permeability ribbons can be used as core materials only in a limited frequency range. This trend of increase of low frequency permeability is observed up to the annealing temperature of 425°C, beyond which permeability decreases to a very low value.
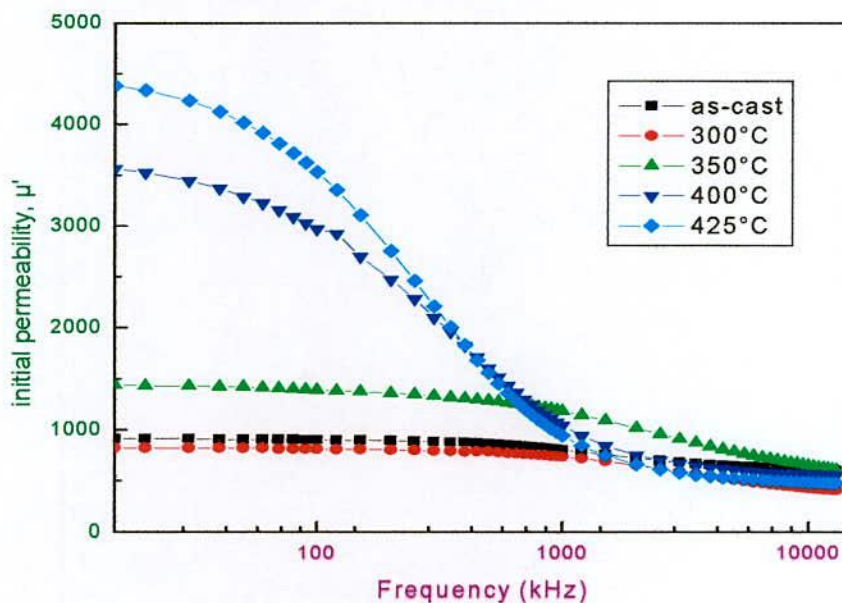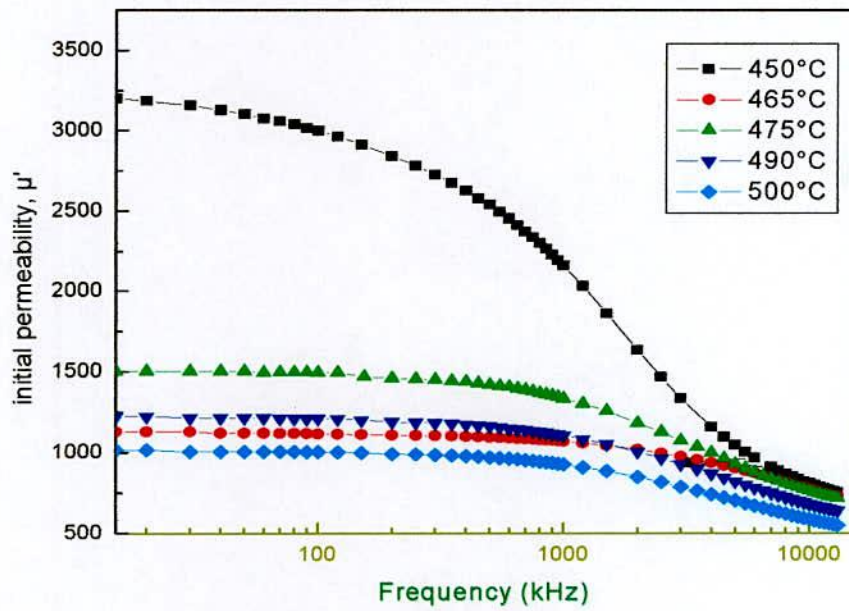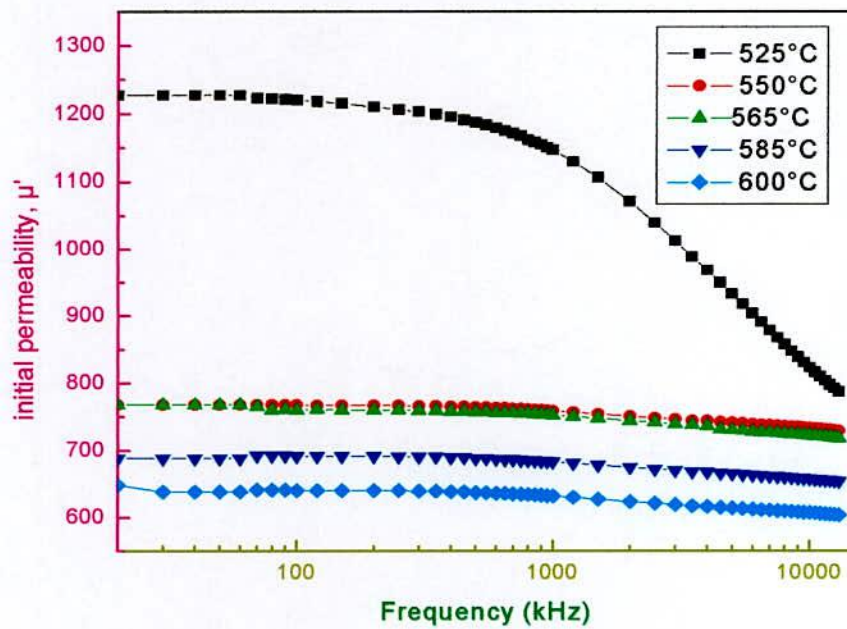

Fig.-6.9 (a)

80

Fig.-6.9 (b)

Fig.-6.9 (c)

Fig.6.9 (a,b,c) Frequency dependence of real component of complex initial permeability at different annealing temperatures for 30 minutes of $Fe_{75.5}Cu_1$ $Nb_1 Si_{13.5} B_9$ alloy

81

From Fig. 6.9 (a) it is seen that μ' changes little with frequency maintains up to average 70 kHz for 425°C annealed samples. Above this critical frequency μ' drops rapidly due to the increase of loss component of complex permeability. From fig 6.9 (b,c) the above mentioned nature is also observed for the samples annealed at 450°C to 525°C, but this critical frequency shifts to higher value of around 700 kHz and above 700 to 800 kHz.

Fig. 6.10 shows the real part of the initial permeability μ' as a function of annealing temperature, T_a at a fixed frequency of 1 kHz. From this graph it is easy to conclude about the strong dependence of initial permeability on annealing temperature. When annealing treatments are performed below the onset of crystallization temperature an increase of initial permeability with annealing temperature was observed due to the stress relaxation of the amorphous matrix i.e. stress relief, increase of packing density of atom by annealing out micro-voids and changing the degree of chemical disorder. This enhancement of μ' primarily stops at 425°C and above 425°C permeability decreases and drops to a low value at 465°C.

This temperature is very close to the crystallization on set temperature (470°C). Sharp fall of μ' is due to stress developed by growing crystallites. These newly grown crystallites serve as pinning centers at which domain walls are pinned and create obstructions for their mobility resulting in a decrease in μ'. Also the growing crystallites are still small in number which cannot be exchange coupled due to large inter grain distance and have high anisotropy energy. A slight rise in μ' is observed above 465°C up to 475°C. But again falls to a low value from 490°C up to 600°C. This means that as soon as crystallization starts at T_{onset} = 470°C grains starts growing very fast with a value of D_g = 17 nm at 475°C to 25 nm at 600°C as seen from Table-6.4. These large grains have high anisotropy. Therefore the μ' could not attain very high value as expected for Finemet family of alloys.

In Fig. 6.11(a,b,c), the effect of annealing temperature on the imaginary permeability (μ'') and its frequency dependence for the sample with composition $Fe_{75.5} Cu_1 Nb_1 Si_{13.5} B_9$. These results are quite complementary to the results of the real part of the complex permeability of the sample. The usefulness of the results of the complex permeabilities lied in the determination of the relative quality factor of the sample which is a merit of any magnetic materials from their applications point of view.
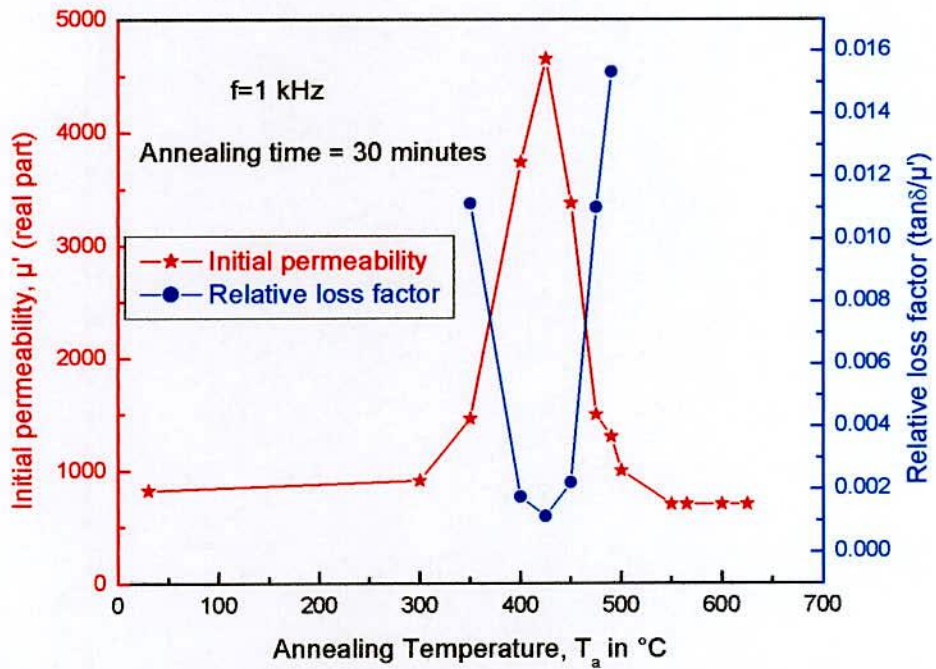
Fig. 6.10 Annealing temperature (T_a) dependence of initial permeability (μ') and relative loss factor (tan δ/μ') for sample $Fe_{75.5} Cu_1 Nb_1 Si_{13.5} B_9$ at room temperature measured at 1 kHz
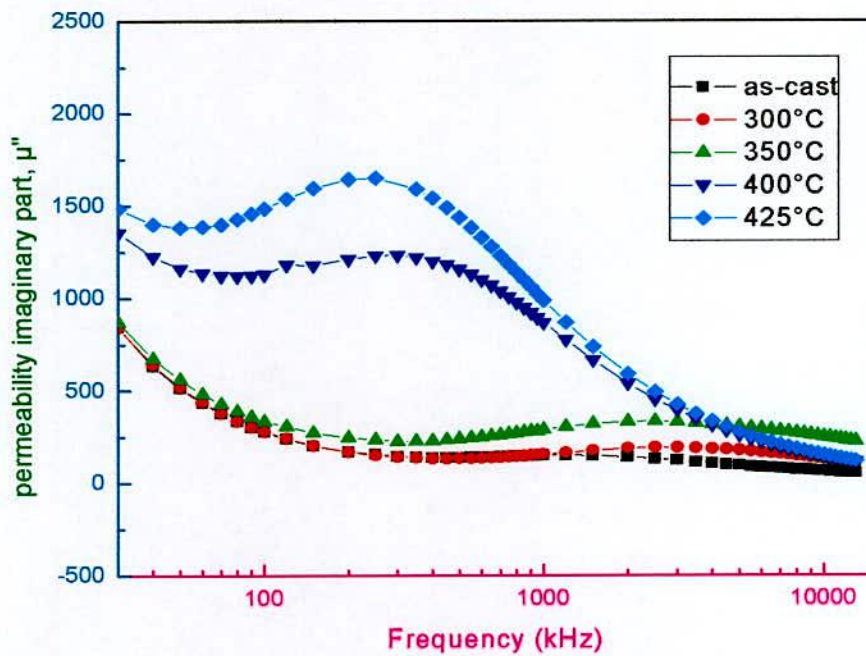
Fig.-6.11 (a)
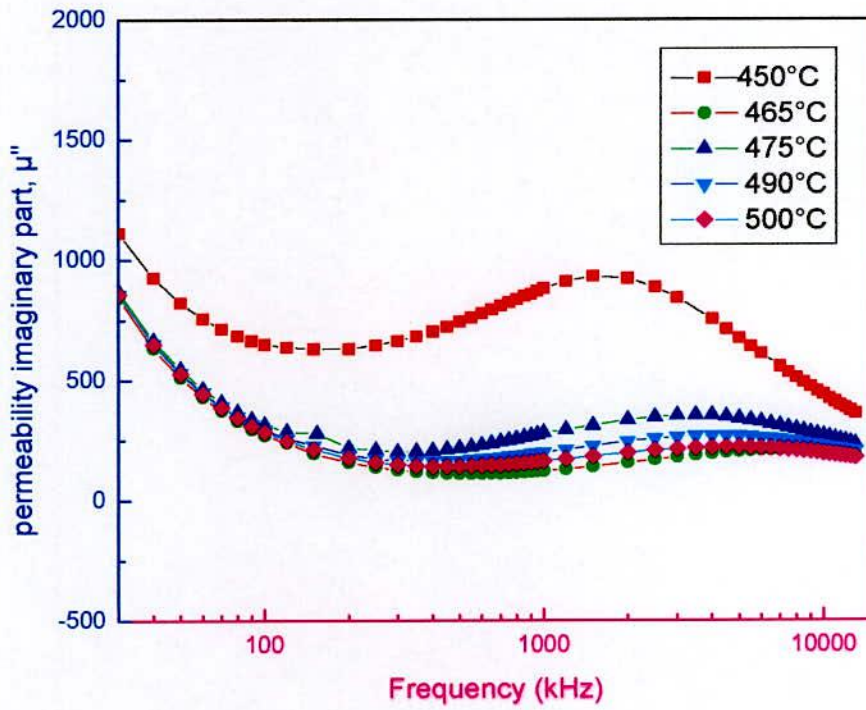
Fig.-6.11 (b)
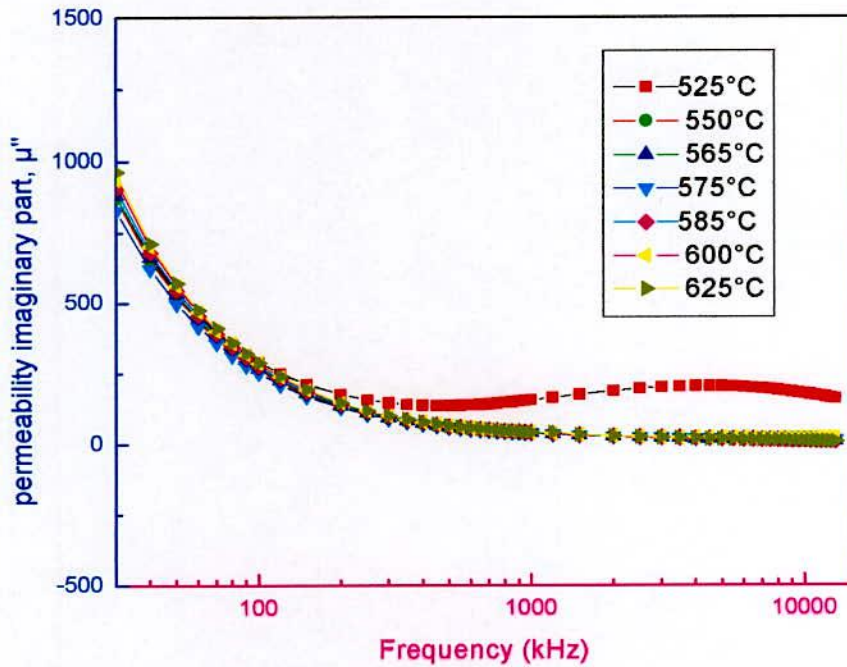
Fig.-6.11 (c)

Fig. 6.11(a,b,c) Frequency dependence of the imaginary part of complex permeability of $Fe_{75.5}Cu_1Nb_1Si_{13.5}B_9$ alloy at different annealing temperature for 30 minutes

84

The complex permeability for all the annealed samples at low frequencies has relatively high value and corresponds to high loss factor and low quality factor. The peak value of μ'' corresponds to resonance frequency which shifts to lower frequency with the increase of μ'.

In fig. 6.12 (a,b,c), the frequency dependence $\left(\dfrac{\mu'}{\tan \delta}\right)$ or $\mu'Q$ with different annealing temperature for 30 minutes. From these two figures [Fig. 6.12 (a) and Fig 6.12 (b)] it is observed that relative quality factor increases with the increase of annealing temperature up to 450°C and above 450°C the quality factor decreases and attains a minimum value at 500°C. In Fig. 6.12 (c), the maximum reduction occurs when the sample above annealed at 550°C, however it is observed that when the quality factor is lower, it is more independent of frequency.

From Fig. 6.12 (a,b) it is observed that the sample annealed at 425°C and 450°C maintains high relative quality factor covering a frequency band of 10 kHz to 100 kHz and 20 kHz to 200 kHz respectively. From the relative quality factor study perfect annealing temperature and frequency band can be identified at which the sample works as soft magnetic material with low loss.
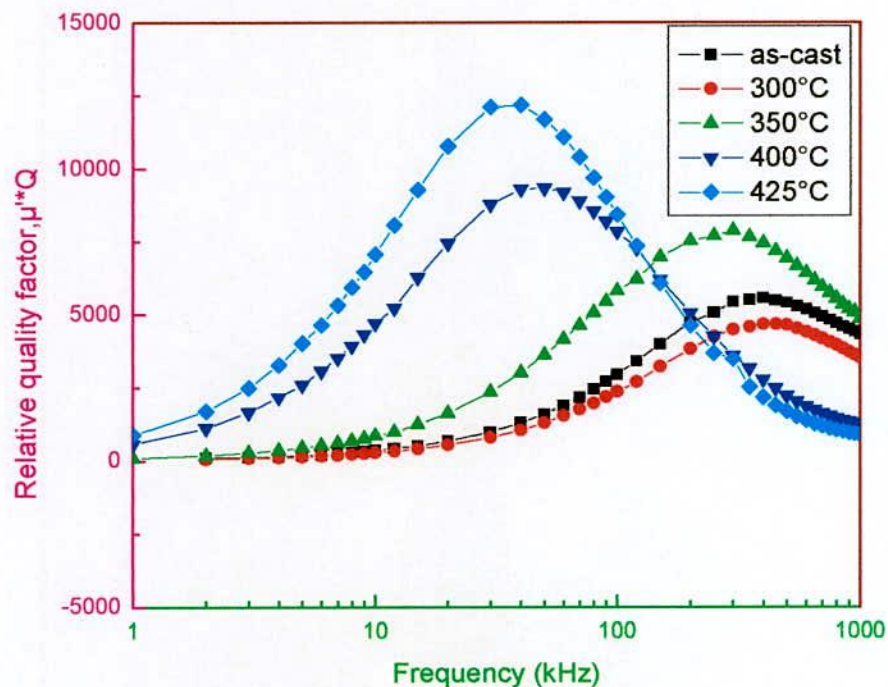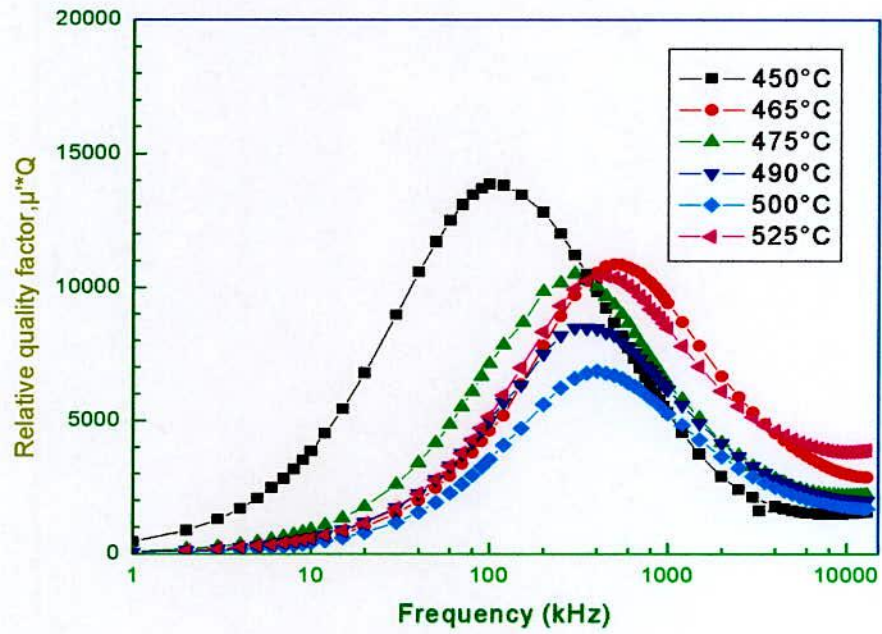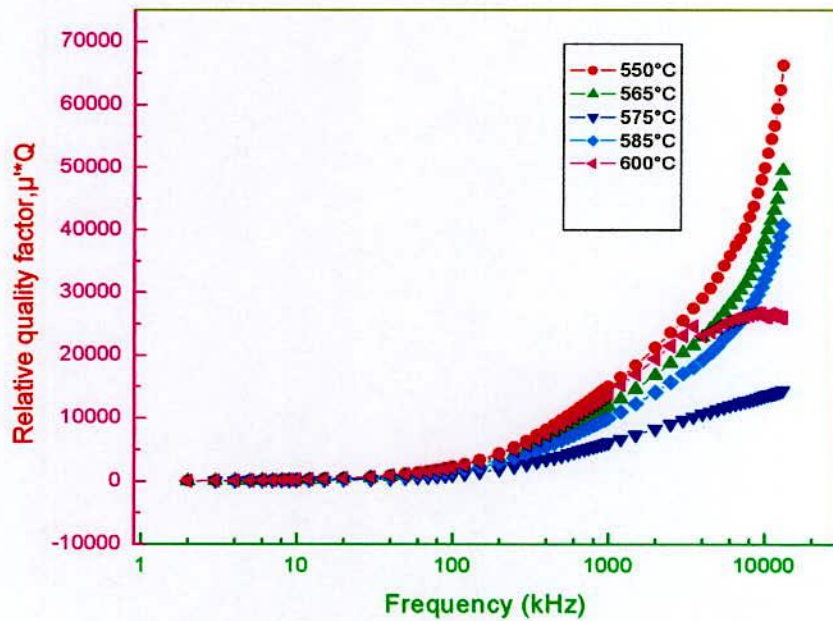

Fig.-6.12 (a)

Fig.-6.12 (b)

Fig.-6.12 (c)

Fig. 6.12 (a,b,c) Frequency dependence of the relative quality factor of $Fe_{75.5}\,Cu_1\,Nb_1$
$Si_{13.5}\,B_9$ alloy at different annealing temperature for 30 minutes

The maximum of relative quality factor with $T_a = 425°C$ and $450°C$, coincides well with the maximum μ' value at the same temperature. This is really what is required for soft magnetic materials from its application point of view i.e. high permeability and simultaneously low relative losses ($\tan\delta/\mu'$) and/or high $\mu'.Q$.

6.3.2 Dynamic magnetic properties of $Fe_{74}\ Cu_{0.5}\ Nb_3\ Si_{13.5}\ B_9$ alloy with different annealing temperature

The measurement has been done on as-cast specimen and also on samples annealed at 300°C to 650°C for 30 minutes. In Fig. 6.13 (a,b) shows the frequency dependence of the real part of the complex initial permeability for as-cast and annealed sample in the temperature range 300°C to 475°C for 30 minutes. It is observed that the initial permeability (μ') increases with the increase of annealing temperature and attains the maximum value at $T_a = 475°C$ when the annealing temperature is higher than 475°C, μ' decreases rapidly. This decrease of permeability may be attributed to the stress developed in the amorphous matrix by growing crystallites. At the temperature of $\approx 500°C$, the initiation of crystallization takes place as found by DTA and XRD.

Fig. 6.13(c) shows the frequency dependence of μ' at the annealing temperatures of 500°C to 650°C for 30 minutes. It is observed that the low frequency values of μ' increase with the increase of annealing temperature and attains the maximum value at $T_a = 575°C$. When the annealing temperature is higher than 575°C low frequency value of μ' decreases rapidly. This spectrum evidences the real change that the nanocrystallization produces in each annealed sample, including the kinetics of structural changes. The trends of increasing low frequency permeability exist up to 575°C, i.e. maximum permeability corresponding to the best soft magnetic properties is observed at this temperature.
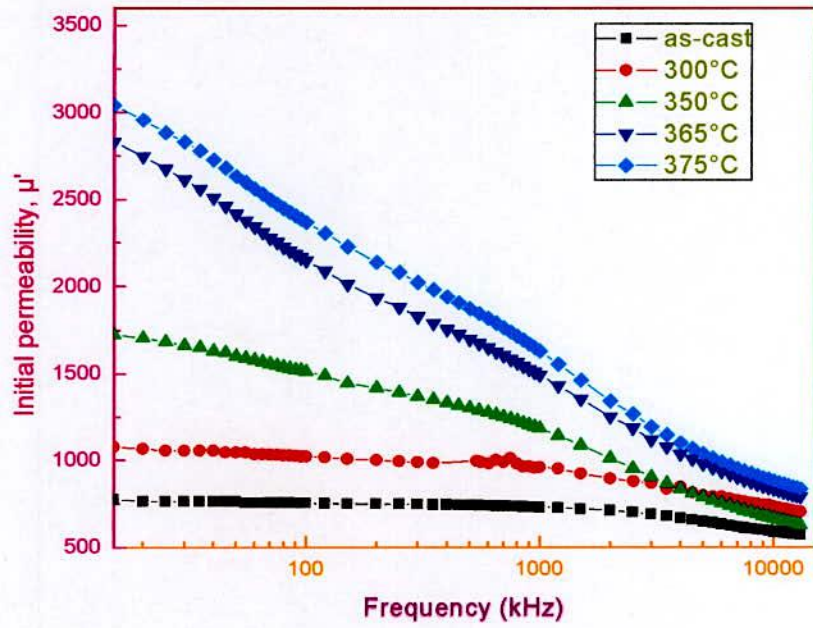
Fig.-6.13 (a)
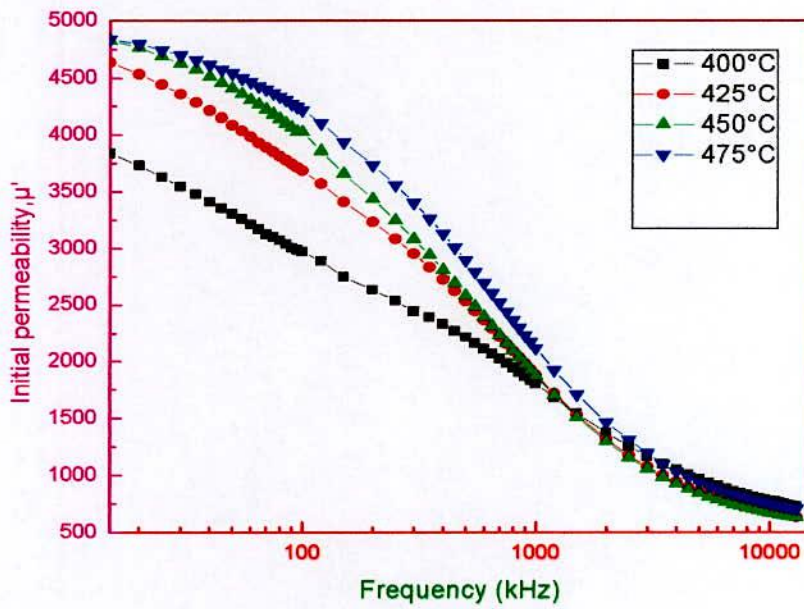
Fig.-6.13 (b)
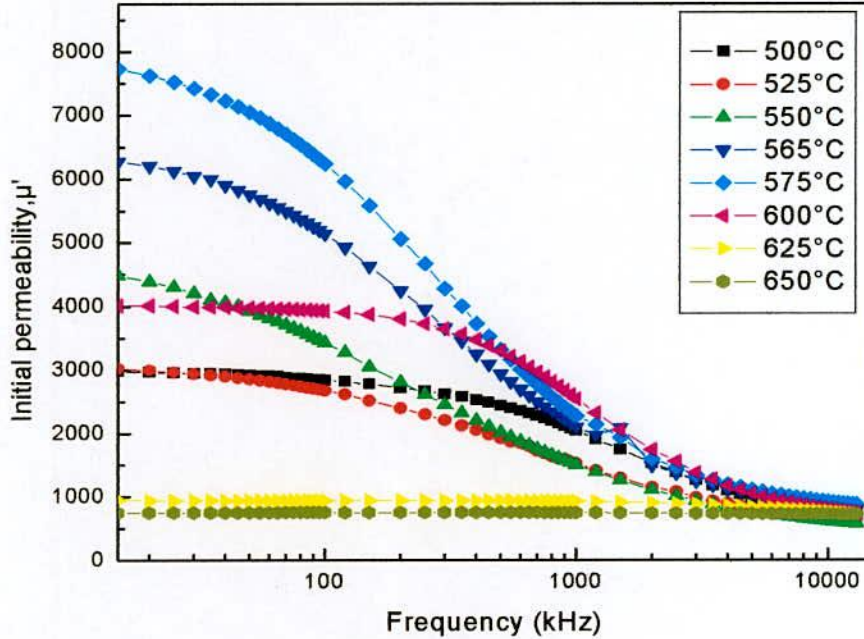
Fig. 6.13 (a,b,c) Frequency dependence of μ' at different T_a for 30 minutes of Fe_{74} $Cu_{0.5} Nb_3 Si_{13.5} B_9$ alloy

In Fig.6.14, μ' has been presented as a function of annealing temperature, T_a at a fixed frequency of 1 kHz. The curve reveals itself strong dependence of initial permeability on annealing temperature, when annealed at temperature below the onset of crystallization. An increase of μ' with T_a from 300°C to 475°C is observed due to irreversible structural relaxation of the amorphous matrix, i.e., stress relief, increase of packing density by annealing out micro-voids and changes in the degree of chemical disorder. At $T_a = 500°C$, the permeability sharply drops to a lower value. This is the temperature around which initiation of crystallization takes place.

The decrease of permeability may be attributed to the new stresses developed in the matrix by the growing crystallites, which act as pinning centers for the domain walls constraining the domain wall mobility as well as weak inter-grain magnetic coupling since the growing crystallites are far apart from each other representing small volume fraction that can not be exchange coupled and the anisotropy cannot be averaged out.

89

Further increase of annealing temperature leads to the increase of permeability due to the increase of volume fraction of α-Fe(Si) nanograins coupled via exchange interaction resulting in a reduction of anisotropy energy. A large enhancement of μ' was observed at the annealing temperature of $T_a = 575°C$.
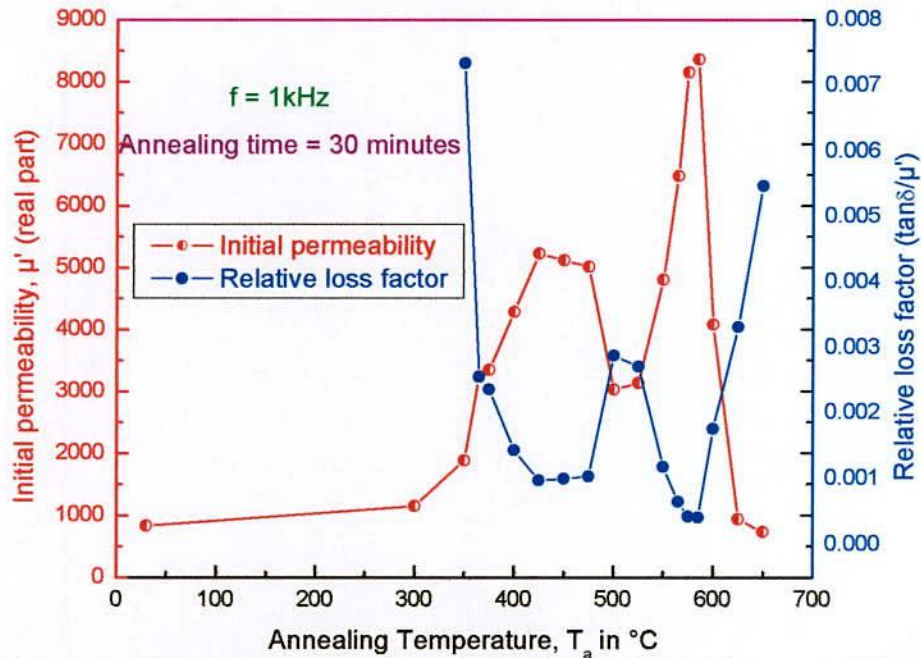
Fig.-6.14 Annealing temperature (T_a) dependence of initial permeability (μ') and relative loss factor ($\tan\delta/\mu'$) for sample $Fe_{74} Cu_{0.5} Nb_3 Si_{13.5} B_9$ at room temperature measured at 1 kHz

For the annealing temperature above 575°C, μ' drops to lower value radically. The probable reason might be the evaluation of boride phase having high anisotropy energy as well as large grain size which attains a value of 21 nm at $T_a = 600°C$. This may leads to the increase of anisotropy energy to a high value, which essentially reduces the local exchange correlation length weakening the intergranular magnetic coupling as a result of which magnetic hardening takes place. The boride phase has been detected by our XRD experiment above 600°C. In Fig. 6.15 (a,b,c), shows the effect of annealing temperature at constant annealing time on μ'' and its frequency dependence for the sample $Fe_{74} Cu_{0.5} Nb_3 Si_{13.5} B_9$ alloy. The complex permeability for all samples at low frequency has relatively high value and corresponds to high loss factor and lower quality factor. The μ'' increases for annealed samples concomitant with the increase of μ'. The peak value of μ'' corresponds to resonance frequency which shifts to lower frequency as the μ' increases.

90

Fig.-6.15 (a)

Fig.-6.15 (b)

91
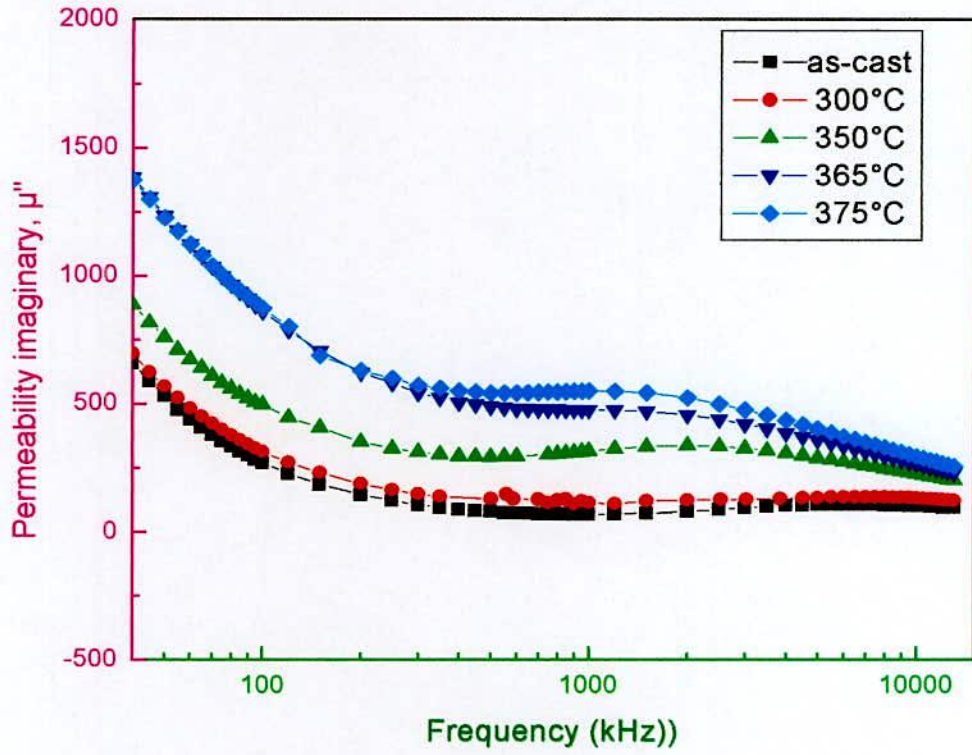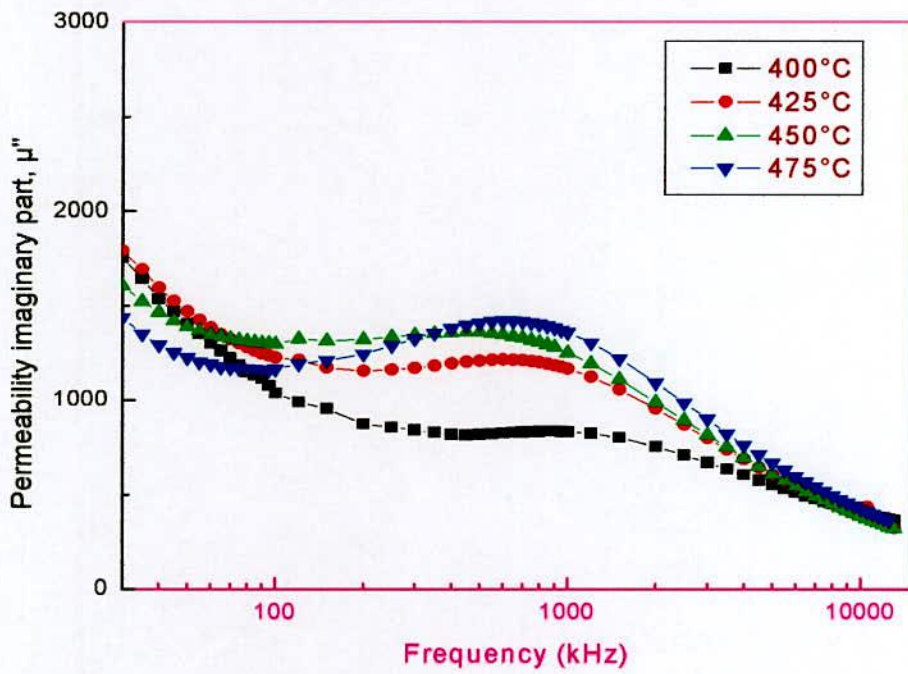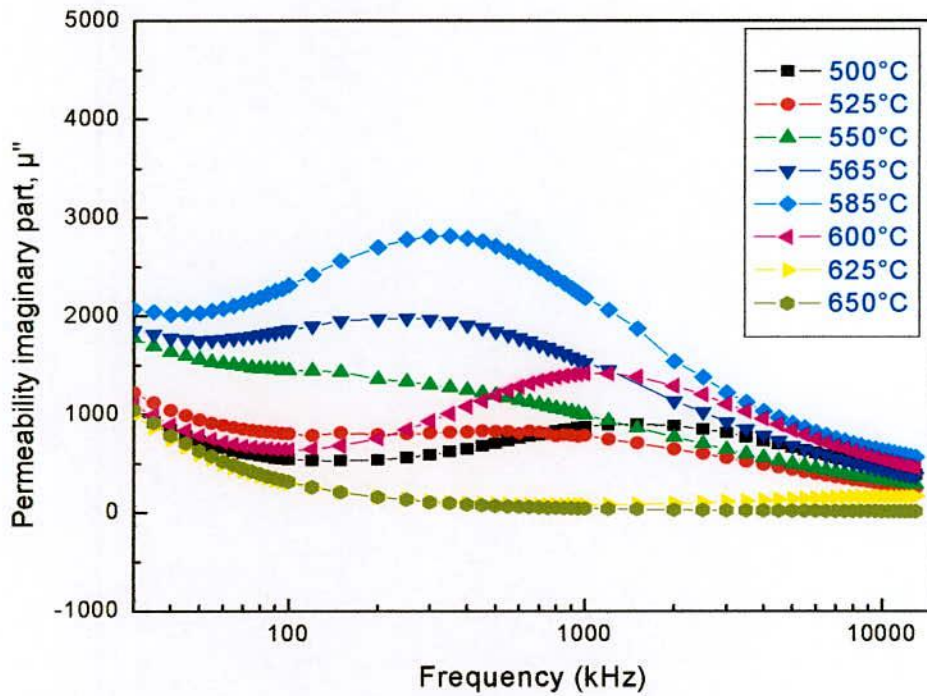
Fig.-6.15 (c)

Fig. 6.15 (a,b,c) Frequency dependence of the imaginary part of complex permeability of Fe_{74} $Cu_{0.5}$ Nb_3 $Si_{13.5}$ B_9 alloy at different annealing temperature for 30 minutes

In Fig. 6.16 (a,b,c) shows the frequency dependence of relative quality factor $\mu'Q$, with different annealing temperature for 30 minutes. Minimum loss factor and maximum relative quality factors are the pre conditions for soft magnetic materials. It is well known that optimal annealing nanocrystalline alloys display minimum loss and very high relative quality factor, $\mu'Q$ of the order of 2×10^4 to 3×10^4. The optimal annealing temperature is determined through successive annealing of the alloys from 300°C to 600°C. In Fig. 6.16 (b,c) shows that the relative quality factor increases with increasing annealing temperature up to 585°C. Above 585°C relative quality factor $\mu'Q$ value decreases, as controlled by μ'' which has very high value at $T_a = 585$°C in the range 100 kHz to 1000 kHz for this nanocrystalline ribbon. At $T_a = 575$ to 585°C, μ' has very high value along with high value of $\mu'Q$ from 5 kHz to 100 kHz frequency range. In these ranges the sample can be useful as a soft magnetic material.

Fig.-6.16 (a)

Fig.-6.16 (b)

93
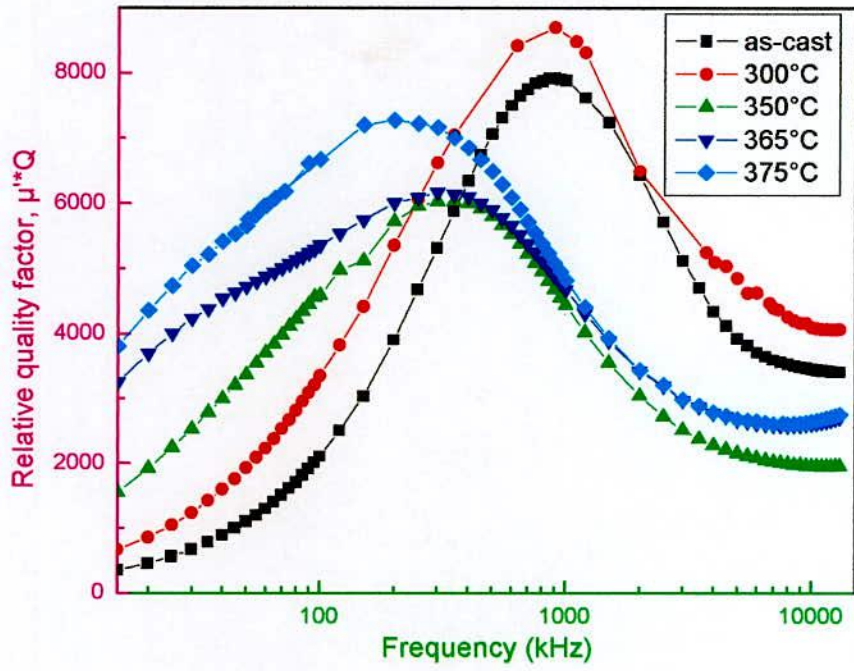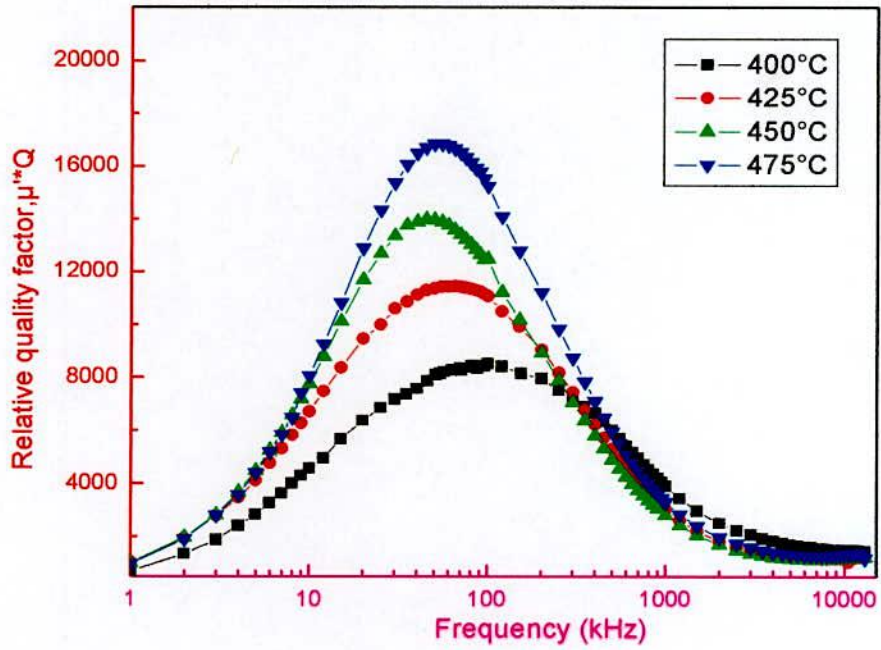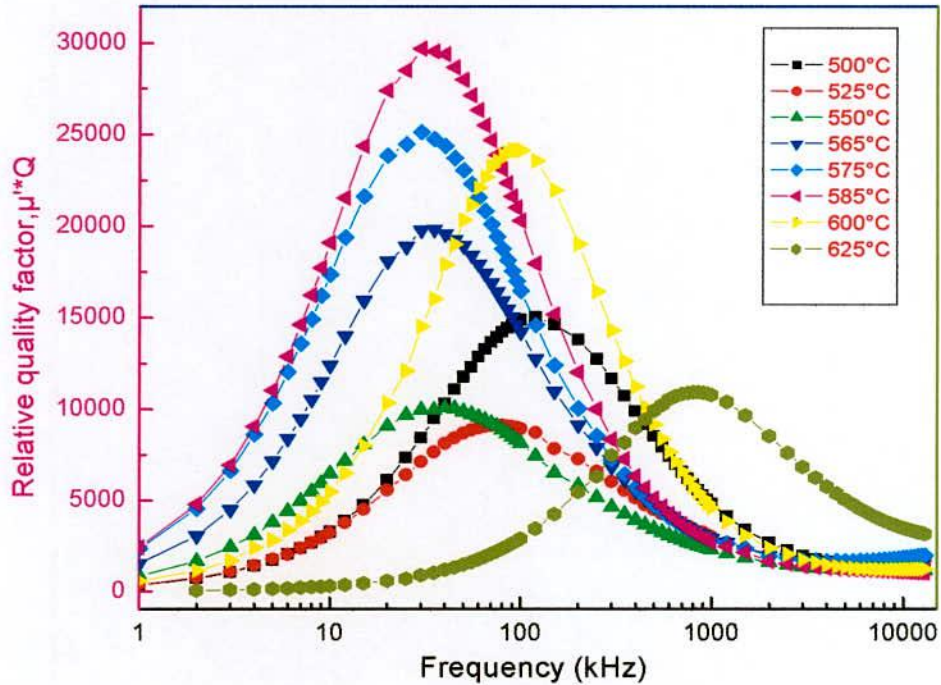
Fig. 6.16 (a,b,c) Frequency dependence of the relative quality factor of $Fe_{74} Cu_{0.5} Nb_3$ $Si_{13.5} B_9$ alloy at different T_a for 30 minutes

6.4 Curie Temperature (T_c) Measurement of Fe-Cu-Nb-Si-B alloys

T_c corresponds to the temperature at which a magnetically ordered material becomes magnetically disordered, i.e. becomes paramagnet. T_c also signifies the strength of the exchange interaction between the magnetic atoms. In general, determination of T_c is not that straight forward as it seems to be from the first principle and the unique volume of T_c can be determined without ambiguity only when the material under study is perfectly homogeneous single phase, defect free and of high purity. The Curie temperature, T_c of amorphous ribbons of composition $Fe_{75.5}$ $Cu_1 Nb_1 Si_{13.5} B_9$ and $Fe_{74} Cu_{0.5} Nb_3 Si_{13.5} B_9$ have been determined using μ vs. T curves. Temperature dependence of ac initial permeability of the sample subjected to a heating rate 5°C/min and the constant frequency of 100 kHz has been used for measuring T_c as shown in Fig. 6.17 and Fig. 6.18. The numerical values of T_c's for the samples are shown in Table-6.6.

94

Table-6.6 Experimental Value of Curie temperature

Amorphous Nanocrystalline sample	Curie Temperature
$Fe_{74} Cu_{0.5} Nb_3 Si_{13.5} B_9$	360°C
$Fe_{75.5} Cu_1 Nb_1 Si_{13.5} B_9$	421°C

From Fig. 6.17 and Fig. 6.18, it is observed that initial permeability increases with the increase of temperature and have the maximum value at a certain point. Beyond this point there is a rapid decrease in the permeability. Well-defined values of T_c obtained from our measurements support the fact that in spite of chemical and structural disorder, ferromagnetic glasses have well defined magnetic ordering temperature.

The sharp fall of the initial permeability are observed at 360°C for sample Fe_{74} $Cu_{0.5} Nb_3 Si_{13.5} B_9$ and 421°C for sample $Fe_{75.5} Cu_1 Nb_1 Si_{13.5} B_9$. From Fig. 6.17 and Fig. 6.18, it is seen that there is no noticeable change in permeability in the glassy materials below 300°C [6.10]. It is interesting to note that the sharp fall of permeability at the T_c enables us to determine T_c unambiguously.

The sharp fall of the permeability at T_c indicates that the material is quite homogeneous from the point to view of amorphousity of materials. It is also observed from this curve that the permeability increases with the temperature and attains maximum value just before T_c, which we consider as Hopkinson [6.11] effect.

The accurate determination of T_c of the amorphous material is really difficult due to irreversible components of the structural relaxation like long-range internal stress, topological and chemical short- range order. Therefore during the measurement of T_c the heating rate should be adjusted in such a way so that no substantial relaxation and crystallization takes place. In our experiment we use heating rate of about 5°C/min that is frequently used for amorphous ribbons.
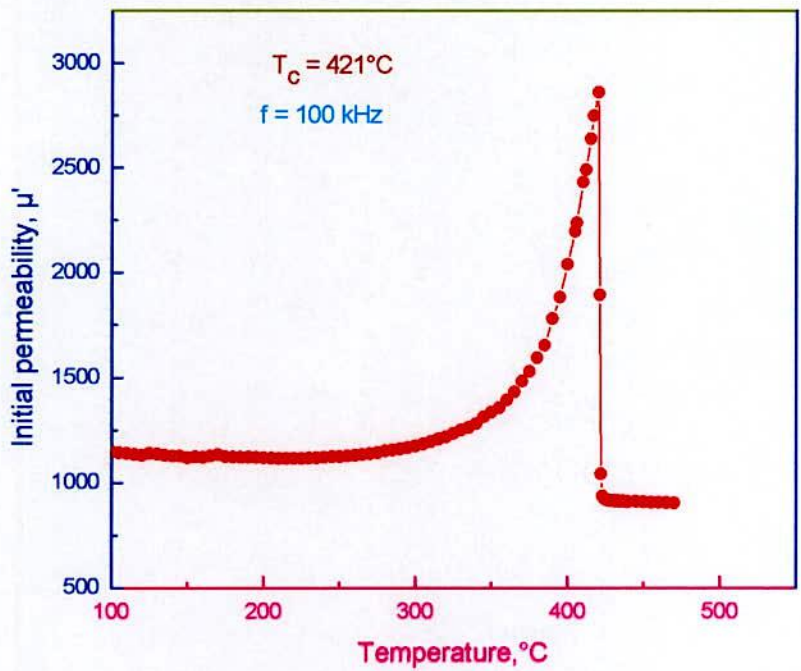
Fig.-6.17 Temperature dependence of initial permeability of as-cast nanocrystalline amorphous ribbon with composition $Fe_{75.5} Cu_1 Nb_1 Si_{13.5} B_9$
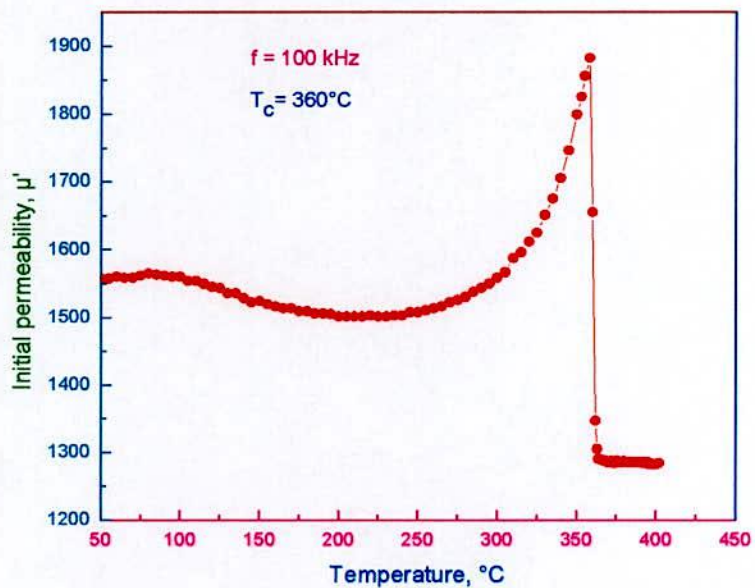
Fig. 6.18 Temperature dependence of initial permeability of as-cast nanocrystalline amorphous ribbon with composition $Fe_{74} Cu_{0.5} Nb_3 Si_{13.5} B_9$

6.4.1 Annealing effects on Curie temperature of $Fe_{75.5} Cu_1 Nb_1 Si_{13.5} B_9$ alloy

In Fig. 6.19, temperature dependence of initial permeability of the as-cast amorphous ribbon and the samples annealed at 425°C to 450°C in the interval of 25°C has been presented. For as-cast and samples annealed at 425°C and 450°C, permeability passes through a maximum just before a sharp fall with the manifestation of Hopkinsons effect characterizing the ferro-paramagnetic transition of the amorphous phase. However, for the sample annealed at 425°C the sharpness of the fall of μ' is relatively weak which might be an indication of initiation of nucleation since no crystalline phase could be detected for this annealing temperature by X-ray diffraction. During the measurement of T_c, the heating rates have been adjusted in such a way that no substantial relaxation takes place. However, the T_c estimated from the curves presented in Fig. 6.19 for the as-cast and annealed samples in the amorphous state has given in Table-6.7.

Table-6.7 Annealing temperature, T_a dependence of the Curie temperature of amorphous matrix T_c of $Fe_{75.5} Cu_1 Nb_1 Si_{13.5} B_9$

Crystalline state	Annealing temperature, T_a in °C	Curie Temperature, T_c in °C
Amorphous state	As-cast	421
	425	427
	450	437
Nanocrystalline state	465	285
	480	268
	500	295
	525	305

From Table-6.7, it can be observed that the T_c of the as-cast sample is 421°C. The T_c increases when the sample is annealed in the temperature range of 425°C to 450°C. Enhancement of T_c during annealing of the amorphous precursor below T_{x_1} is caused by the irreversible structural relaxation of microstructural quantities like long range internal stress, topological and chemical short-range order.

These microstructural effects bring about a change in the inter-atomic distances, which directly affect the strength of the exchange interaction resulting in a change of Curie temperature. Further, from the analysis of the Mössbauer spectra for the quenched and annealed samples below the crystallization temperature, it has been observed that this treatment leads to the increase in packing density of atoms [6.12]. Increase in packing density of atoms might have significant contribution in the enhancement of T_c in amorphous state.
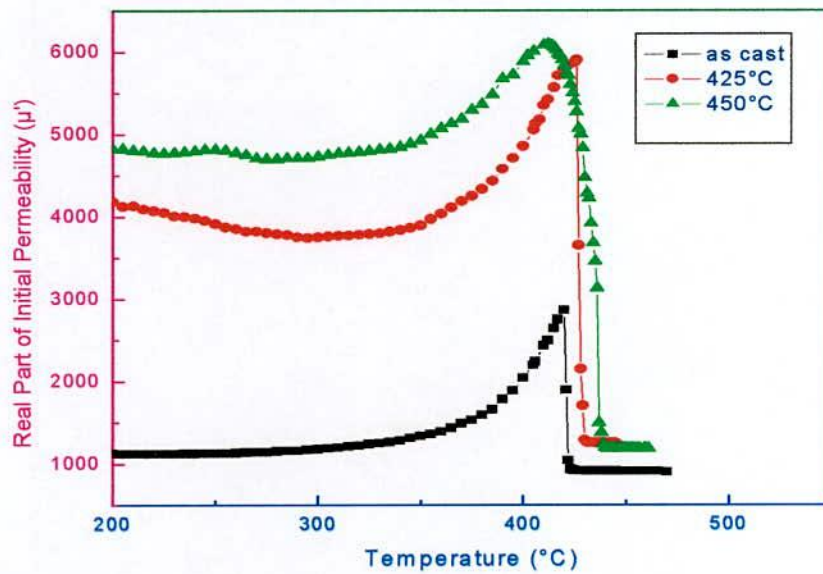
Fig.-6.19 Temperature dependence of μ' of as-cast and annealed sample in the amorphous relaxed state of $Fe_{75.5} Cu_1 Nb_1 Si_{13.5} B_9$ alloy

In Fig. 6.20, the variation of μ' with temperature for the toroid annealed at 465°C ~ 525°C has been presented. It is observed that the sharpness of the fall of μ' is progressively smeared out with the appearance of a tail in the high temperature region. These results are in good agreement with those previously reported for the FINEMET composition [6.13]. Curie temperature of residual amorphous matrix determined from derivative of μ' vs. T curves has been presented in Table-6.7.

T_c of the amorphous matrix decreases significantly when annealed at and above crystallization temperatures. The probable reason of decreasing the T_c of the amorphous phase when annealed at and above the crystallization temperature is that

amorphous matrix is depleted with iron and the relative amount of Nb in the amorphous matrix increases, which weakens the exchange interaction resulting in a decrease of T_c of the amorphous matrix. It is interesting to observe an enhancement of T_c again when samples are annealed at higher temperature. This increase cannot be explained in a straight forward way. Probably redistribution of atomic species, local environment of the matrix and the compositional variance of the residual amorphous matrix as well as the procedure used to determine T_c are the cause of the behavior.

The following discussion can clear some complexity regarding the phase transition temperature of the higher temperature annealed sample. The worthwhile to note that if we look into the graph of μ' vs. T (Fig. 6.20) critically we observe that decrease of μ' with T is quite different from that of μ' - T curves of Fig. 6.19 which is relatively smeared out. It is very difficult to find out a unique value of T_c from such diffused μ' vs. T measurements. The more diffuse character of the ferro-paramagnetic transition in the residual amorphous matrix for the samples annealed at higher temperatures is attributed to the higher degree of compositional and structural disorder in the residual amorphous phase [6.14, 6.15]. Varga et al. [6.16] have interpreted this type of reduction of T_c in FINEMET alloys after annealing at higher temperature as due to compositional gradients within the remaining amorphous phase.

Within the inhomogeneous amorphous phase there is basically no longer a unique Curie temperature, but a distribution of T_c. As a consequence instead of a single $\mu'(T)$ curve, the combination of a family of curves with distributions of Curie temperature is obtained. Therefore the T_c values mentioned in the present study related to the samples annealed at relatively high temperatures should not be taken so seriously. However, the decrease of T_c shown in the Table-6.7 is a general trend of the alloys under investigation since $\dfrac{d\mu'}{dT}$ has been taken to estimate the T_c from these measurements. At higher measuring temperatures above T_C^{am}, permeability value decreases to very low value. Franco et al [6.13] have demonstrated super paramagnetic behavior is a general feature of these nanocrystalline alloys. The practical requisite for observing superparamagnetic relaxation in the nanocrystalline alloys is the absence of interaction between nanograins in the residual matrix.

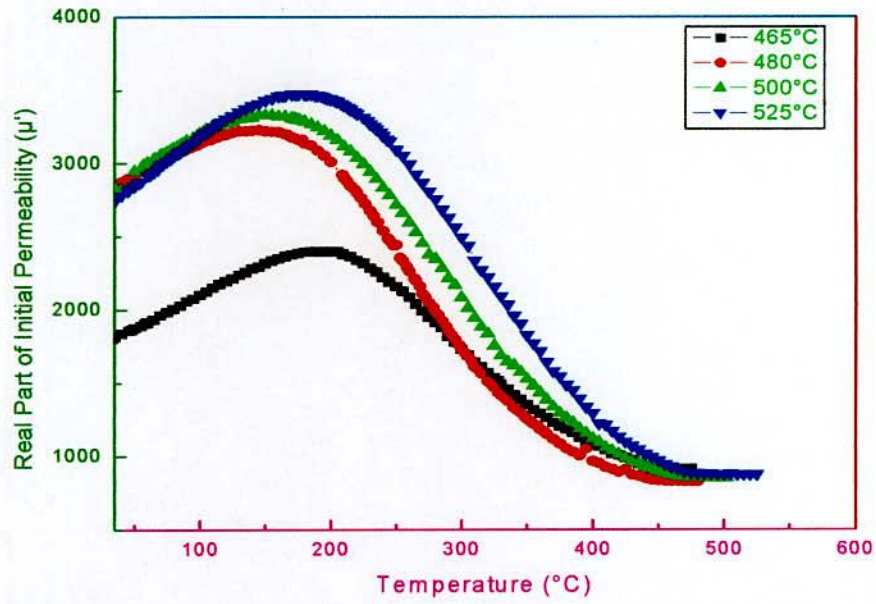Fig. 6.20 Temperature dependence of μ' in the nanocrystalline state of $Fe_{75.5}\,Cu_1\,Nb_1$ $Si_{13.5}\,B_9$ alloy
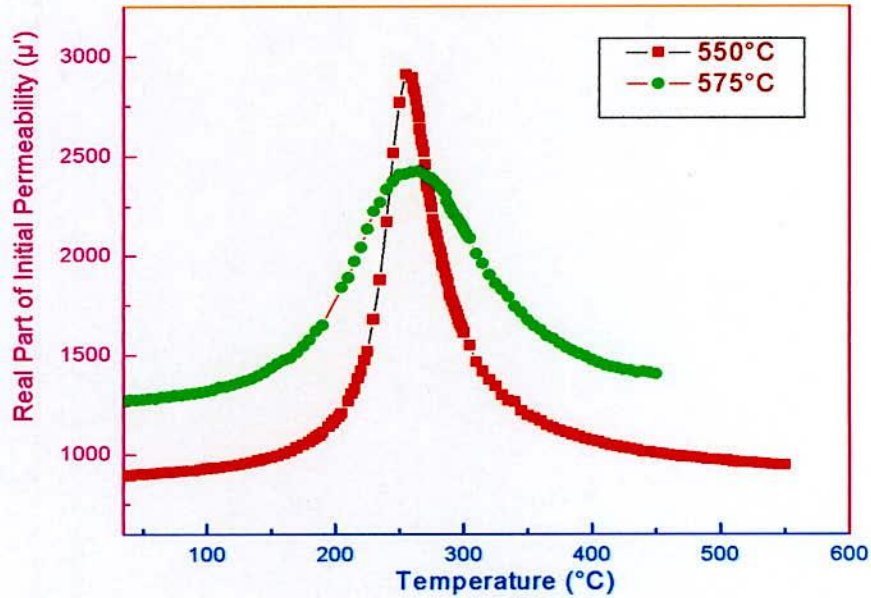
Fig. 6.21 Temperature dependence of μ' after evoluation of Fe_2B in the nanocrystalline state of $Fe_{75.5}\,Cu_1\,Nb_1\,Si_{13.5}\,B_9$ alloy

In Fig. 6.21, the variation of real part of initial permeability μ' with temperature has been presented for samples annealed at 550°C to 575°C. In Fig. 6.10, it has been observed that the value of μ' has dropped to a very low value for the sample with annealing temperature of 550°C. It has been reported earlier that this fall of μ' to a very low value might occur due to the evolution of boride phase at higher temperature. In our experiment the presence of boride phase could not be detected by X-ray diffraction. Since the anisotropy constant K_1 of Fe_2B (430 kJ/m^3) is five order of magnitude higher than the average anisotropy $< K >$ of α-Fe(Si) nanograins (4 J/m^3), presence of small amount of Fe_2B phase can cause a substantial reduction of exchange interaction [6.17]. Temperature dependence of μ' reveals the presence of Fe_2B, which could not be detected by XRD. Since K_1 of Fe_2B passes from negative to positive value at 255°C, a dramatic rise of μ' from 760 at room temperature to 3000 at 255°C for the sample annealed at 550°C is evidenced. However for the sample annealed at 575°C the value of μ' rises from 700 at room temperature to 2300 at 265°C. Such a sharp increase of μ' at around 260 $\pm$ 5°C is only possible if the anisotropy energy approaches zero at this temperature. Therefore μ' vs. T measurement is a powerful technique to find out the boride phase in the FINEMET alloys, which XRD cannot do.

6.5 Specific Magnetization measurement of Nanocrystalline amorphous ribbons

The magnetization of as-cast Fe-Cu-Nb-Si-B amorphous and samples annealed for 30 minutes at varying temperature from 450°C to 600°C has been measured as a function of magnetic field generated by an electromagnet using a Vibrating Sample Magnetometer (VSM). In this type of magnetometer, the sample is vibrated up and down in a region surrounded by several pickup coils. The magnetic sample is thus acting as a time changing magnetic flux, varying inside a particular region of fixed area. The magnetometer was calibrated using a high purity Ni disk considering the saturation magnetization of Ni = 54.75 emu /gm at room temperature. The ribbon samples were cut into small shapes, weighed and glued to a standard sample holder.

6.5.1 Effect of annealing temperature on specific magnetization at room temperature

Specific Magnetization (M_s) at room temperature has been measured on as-cast and annealed samples. The annealing has been carried out for 30 minutes at T_a = 450°C, 500°C, 525°C and 550°C for $Fe_{75.5} Cu_1 Nb_1 Si_{13.5} B_9$ and at $T_a \approx 475°C$, 500°C, 525°C and 600°C for $Fe_{74} Cu_{0.5} Nb_3 Si_{13.5} B_9$. Fig. 6.22 and Fig. 6.23 show the field dependence of specific magnetization for amorphous as-quenched and thermally treated samples measured by VSM. From the curves it is clearly evidenced that the magnetization is saturated for all the samples in the amorphous and annealed states within an applied field of 2000 Oe. It can be seen that with increasing annealing temperature magnetization increases until T_a = 525°C. The maximum saturation magnetization is reached at T_a = 525°C for both the samples. Aranda *et at.* [6.18] have studied the approach to saturation in nanocrystalline FINEMET materials. The magnetization prior to saturation is associated with reversible rotation and has been fitted to the law

$$M(H) = M_s \left[1 - \frac{a_1}{H} - \frac{a_2}{H^2} \right] + bH^{\frac{1}{2}}, \qquad (6.2)$$

where the term $\frac{a_2}{H^2}$ was described as being a direct consequence of the random anisotropy model, and attributable to Fe-Si grains. The co-efficient a_2 reflects the Herzer's predicted effective magnetic anisotropy of the nanocrystalline material, where as in amorphous alloys it is postulated as being caused by local stress and magneto elastic coupling. Saturation magnetization M_s, has been observed to increase from 140 to 163 emu / gm for $Fe_{75.5} Cu_1 Nb_1 Si_{13.5} B_9$ and 128 to 141 emu / gm for $Fe_{74} Cu_{0.5} Nb_3 Si_{13.5} B_9$ with the increase of annealing temperature.

An increase of M_s for the annealed samples at 450°C to 525°C compared with the amorphous state is due to the irreversible structural relaxation, changing the degree of chemical disorder of the amorphous state [6.19] and enhanced volume fraction of Fe(Si) nanocrystals that are exchange coupled. The saturation magnetizations are shown in Table-6.8.
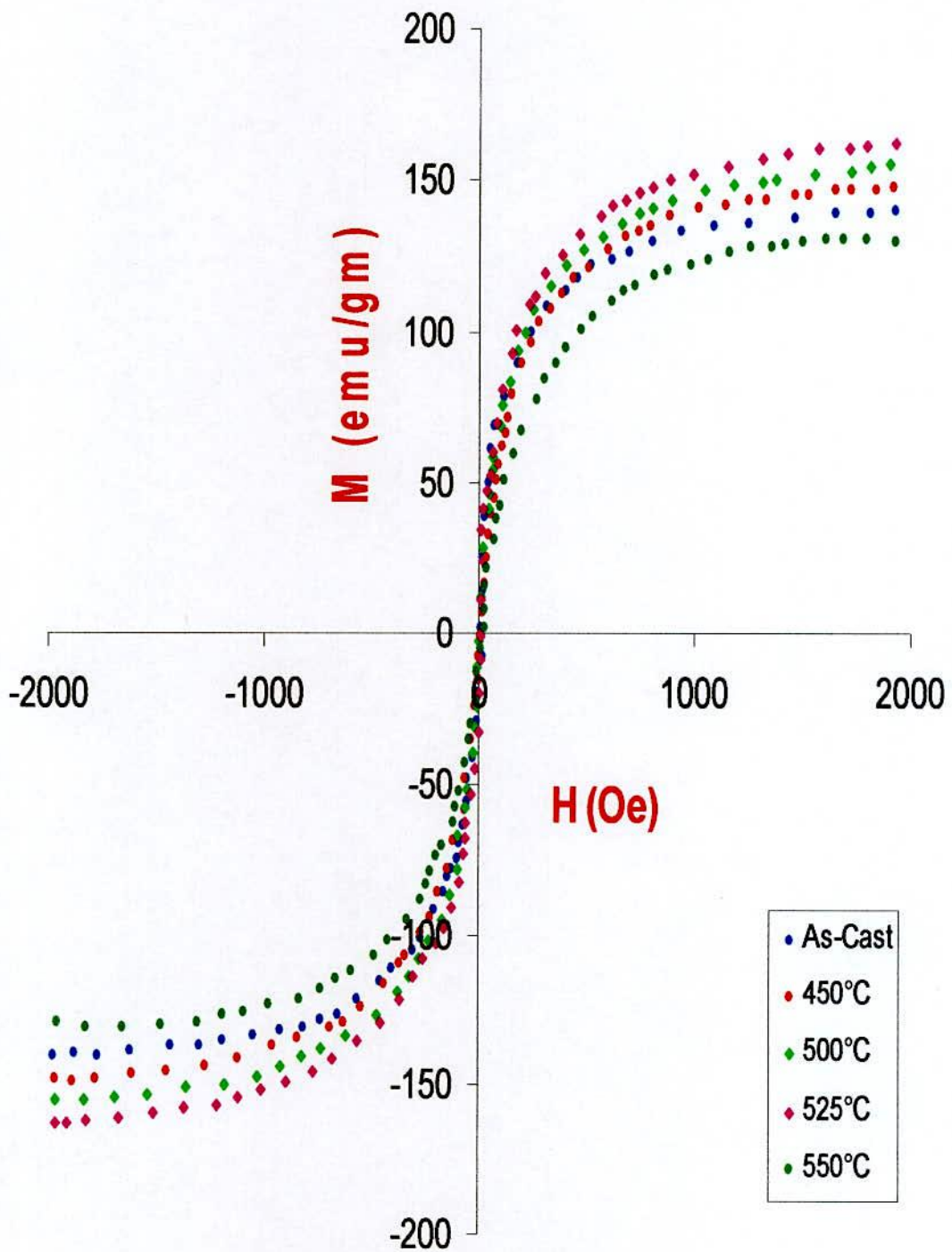
Fig.-6.22 Specific magnetization versus magnetic field of as-cast and annealed samples of $Fe_{75.5}Cu_1Nb_1Si_{13.5}B_9$ alloy
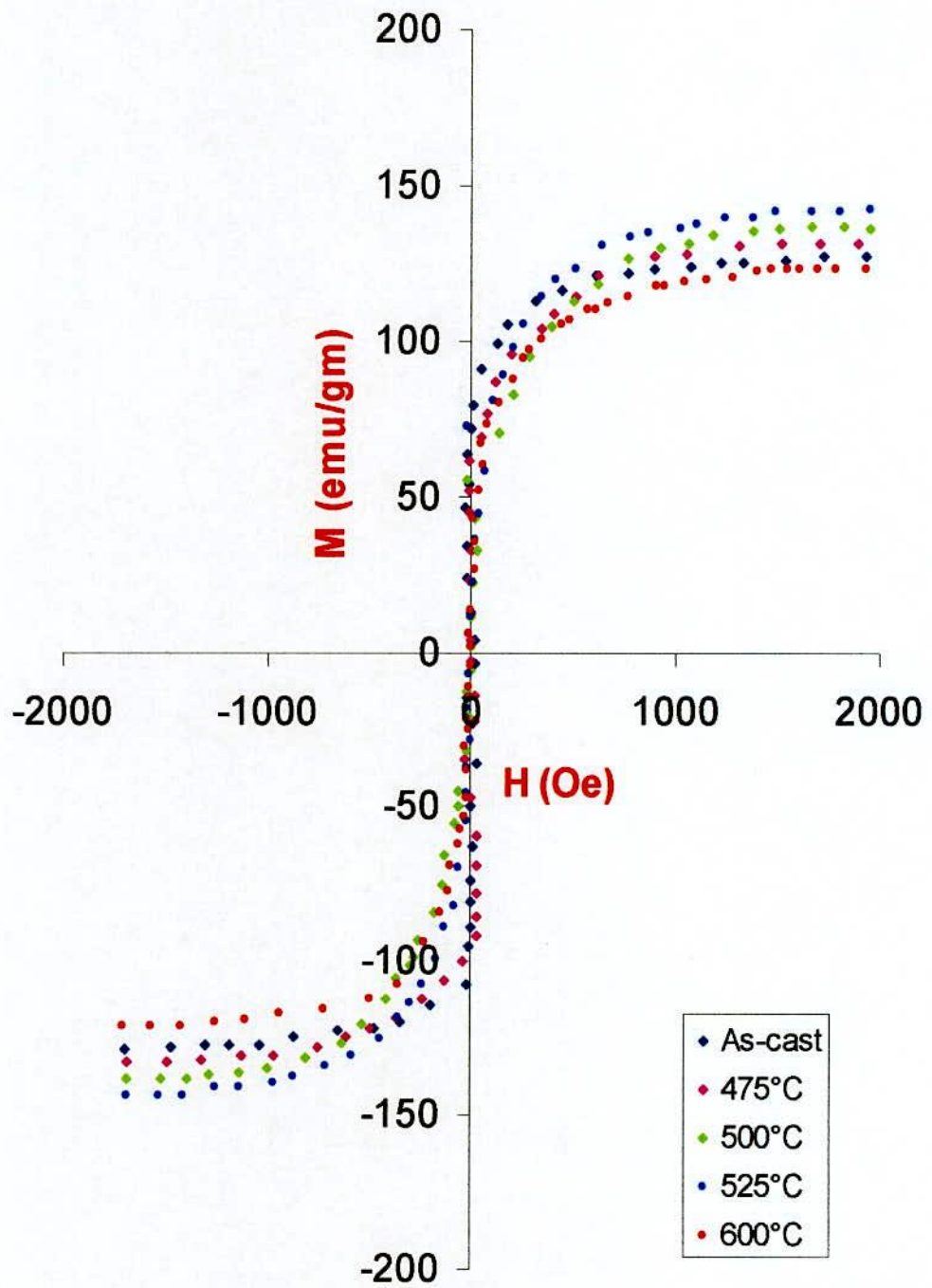
Fig.-6.23 Specific magnetization versus magnetic field of as-cast and annealed samples of $Fe_{74} Cu_{0.5} Nb_3 Si_{13.5} B_9$ alloy

Table-6.8: The values of saturation magnetization of Fe-Cu-Nb-Si-B alloys at different annealing temperature with constant annealing time 30 minutes

Samples	Annealing temperature, T_a in °C	Saturation magnetization, M_s in emu /gm
$Fe_{75.5}Cu_1Nb_1Si_{13.5}B_9$	As-cast	140
	450	148
	500	155
	525	163
	550	130
$Fe_{74}Cu_{0.5}Nb_3Si_{13.5}B_9$	As-cast	128
	475	133
	500	138
	525	141
	600	124

It is to be noted that an increase in M_s due to structural relaxation has also been detected in Fe-based glasses [6.20]. A rapid decrease in M_s has been observed with increasing annealing temperature at 550°C for $Fe_{75.5}$ Cu_1 Nb_1 $Si_{13.5}$ B_9 and at 600°C for Fe_{74} $Cu_{0.5}$ Nb_3 $Si_{13.5}$ B_9. The decreasing of M_s may be connected with the enrichment of the residual amorphous phase with Nb that weakens the coupling between ferro-magnetic nanograins. Also the role of Si diffusion into Fe (Si) nanograins and these local environments also may have effect in decreasing M_s. The decrease of M_s for the sample higher annealing temperature on ordering of Fe_3Si nanograin can not be ruled out.

CHAPTER – 7

CONCLUSIONS

Conclusions

Nanocrystalline amorphous ribbons of the Finemet family with nominal compositions $Fe_{75.5} Cu_1 Nb_1 Si_{13.5} B_9$ (sample-A) and $Fe_{74} Cu_{0.5} Nb_3 Si_{13.5} B_9$ (sample-B) have been studied to find out the correlation between microstructural features and soft magnetic properties dependent on various stages of nanocrystallization during the isothermal annealing around the crystallization temperature of their amorphous precursors. These ribbons were produced by melt spinning technique with 20-25μm thickness. Crystallization behaviour and magnetic properties have been studied by XRD, DTA, an LCR meter and VSM.

The crystallization behavior of the samples was investigated by DTA. The amorphous and annealed samples were examined by XRD. The frequency spectra of the annealed samples were performed by an LCR meter and specific magnetization of the annealed samples as a function of magnetic field were measured by a VSM. From the systematic investigation on the crystallization, structural and magnetic properties, the following conclusions can be outlined.

(i) DTA reveals the primary, Fe(Si) and secondary (Fe-B) crystallization temperatures with the manifestation of two well-defined exothermic peaks. The knowledge of crystallization temperatures has been fruitfully utilized during the isothermal annealing of these amorphous ribbons for nanocrystallization, which ultimately controls the magnetic properties of Finemet alloys. The onset of crystallization temperature T_{x_1} has been found to be 470°C and 504°C for the sample-A and sample-B respectively indicating higher thermal stability of sample-B against nanocrystallization. The temperature difference between the two crystallization peaks $(T_{p_2} - T_{p_1})$ is higher for sample-B (120°C) than that of sample-A (87°C) implying higher thermal stability against boride phase formation, which is detrimental for the soft magnetic properties. This higher value of peak separation temperature for sample-B is important for the stability of the primary crystallization phase Fe(Si) for the fabrication of high quality inductors.

106

(ii) The amorphous stage of the as-cast ribbons has been confirmed by XRD. The evolution of nanocrystallites of bcc Fe(Si) and their sizes have been determined from the line broadening of fundamental peaks (110) from XRD pattern as affected by annealing around the crystallization temperatures. The grain sizes determined for the sample-A varies from 17 nm to 27 nm for the annealing temperature from 475°C to 700°C while that of sample-B varies from 13 nm to 22 nm for T_a from 525°C to 700°C. It means that higher Nb content in sample-B has controlled the grain growth. The crystallization onset temperature found for sample-A is between 450°C and 475°C while for sample-B is between 500°C and 525°C. The value coincides well with the value obtained from DTA. XRD study reveals the boride phase at 650°C for sample-B, while for sample-A it could not be detected by XRD.

(iii) Magnetic initial permeability of nanocrystalline / amorphous ribbon strongly depends on annealing temperature. The improvement in the soft magnetic properties can be ascribed to the much refined grain structure in the range of 10 to 20 nm obtained at various temperatures during annealing. When alloys were annealed for 30 minutes at various temperatures, the maximum initial permeability (μ') were observed at T_a = 425°C for $Fe_{75.5} Cu_1 Nb_1 Si_{13.5} B_9$ and T_a = 575°C for $Fe_{74} Cu_{0.5} Nb_3 Si_{13.5} B_9$ alloys. These temperatures correspond to a maximum initial permeability and lowest high frequency losses. A sharp increase of initial permeability was observed for the optimized annealed sample of $Fe_{74} Cu_{0.5} Nb_3 Si_{13.5} B_9$. The $Fe_{75.5} Cu_1 Nb_1 Si_{13.5} B_9$ sample showed somewhat lower maximum permeability and even at temperature lower than the crystallization onset temperature. Therefore the value of μ' is related to amorphous relaxed state. Further increase of T_a deteriorated the μ'. The high permeability is attributed to the drastic decrease of effective anisotropy due to nanometric grain size effect and strong magnetic coupling. The sample $Fe_{74} Cu_{0.5} Nb_3 Si_{13.5} B_9$ showed magnetic hardening at 500°C to 525°C with very low value of μ' due to stress developed during the initiation of crystallization.

(iv) For technological uses of nanocrystalline materials at elevated temperature and for magnetic stability it is important to look for compositions that give higher values of Curie temperature (T_c). The T_c is 421°C for as-cast amorphous $Fe_{75.5} Cu_1 Nb_1 Si_{13.5} B_9$ alloy and 360°C for $Fe_{74} Cu_{0.5} Nb_3 Si_{13.5} B_9$ alloy. Enhancement

107

of T_c was observed for samples annealed below the crystallization temperature due to structural relaxation. T_c of interfacial amorphous phase has been found to decrease for samples when annealed above the crystallization temperatures due to the depletion of Fe and increase of relative amount of Nb in the residual amorphous phase.

(v) The saturation magnetization for nanocrystalline samples has slightly increased for annealing at temperature around the onset of crystallization. When annealed at higher temperature at which complete crystallization takes place, magnetization decreases again.

There is much scope for further research in controlling the magnetic characteristics by changing composition and heat treatment. Certain important parameters like magnetic anisotropy, temperature dependence of magnetization and magnetostriction can be studied in detail for a better understanding of microstructure property relationship.

REFERENCES

Chapter-1

1.1 H. Gleiter, Progress in Materials Science, (1989) **33** 223.

1.2 H. Gleiter, in Mechanical properties and Deformation Behavior of Material Having Ultra-Fine Micro Structure Eds. M. Nastasi, D. M. Parkin and H. Gleiter, NATO ASI Series E: Applied Science, Kluwer Acad. Pub., Dordrecht, (1993) **233** 3.

1.3 R. Birringer, in Nanophase Materials: Synthesis- Properties- Applications, eds. G.S. Hadjipanayis and R.W. Siegel, NATO ASI Series E: Applied Science, Kluwer Acad. Pub., Dordrecbt, (1994) **260** 157.

1.4 T. Kulik, A. Hernando, M. Vasquez "Correlation between structure and the magnetic properties of amorphous and nanocrystalline $Fe_{73.5} Cu_1Nb_3 Si_{22.5-x}B_x$ alloys", J. Magn. Magn. Mater. (1994) **133** 310.

1.5 Jing Zhi, Kai-Yuan He, Li-Zhi Cheng, Yu-jan Fu, "Influence of the elements Si/B on the Structure and Magnetic Properties of Nanocrystalline (Fe, Cu, Nb) $_{77.5}Si_x B_{22.5-x}$ alloys", J. Magn. Magn. Mater. (1996) **153** 315.

1.6 S. N. Kane, S. Sarabhai, A. Gupta, L.K. Varga, T. Kulit, "Effect of quenching rate on crystallization in $Fe_{73.5}Si_{13.5}B_9Cu_1Nb_3$ alloy", J. Magn. Magn. Mater (2000) **215-216** 372.

1.7 M. El Ghannami, T. Kulit, A. Hernando, L. Fermandez Barquin, J. C. Gomez Sal, P. Gorria, J. M. Barandarian , "Influence of the Preparation Conditions on the Magnetic properties and Electrical resistivity of $Fe_{73.5}Nb_3Cu_1Si_{13.5}B_9$ Nanocrystalline alloys", J. Magn. Magn. Mater. (1994) **133** 314.

1.8 J. Bigot, N. Lecaude, J. C. Perron, C. Millan, C. Ramiarinjaona, J. F. Rialland, "Influence of Annealing Conditions on Nanocrystalization and Magnetic Properties in $Fe_{73.5}Cu_1Nb_3 Si_{13.5}B_9$ alloy", J. Magn. Magn. Mater. (1994) **133** 299.

1.9 M. Hasiak, J. Zbroszczyk, J. Olszewki, W. H. Ciuzynska, B. Wyslocki, A. Blachowicz, "Effect of cooling rate on Magnetic Properties of Amorphous and Nanocrystalline $Fe_{73.5}Cu_1Nb_3 Si_{15.5}B_7$ alloy", J. Magn. Magn. Mater. (2000) **215-216** 410.

1.10 Y.Yoshizawa, S. Oguma, K. Yamauchi, "New Fe-Based Soft Magnetic Alloys Composed of Ultra fine Grains Structure", J. Appl. Phys. (1988) **64** 6044.

1.11 Y.Yoshizawa and K. Yamauchi, IEEE Trans. Magn. **25** (1989), P. 3324; Abstract-INSPEC/ Order Document/ Order Document/ Full Text via Cross Ref / Abstract References in Scopus/ Cited by in Scopus.

1.12 Vacuum schmelze Gmbh, Toroidal Cores of VITROPERM, Data Sheet PW-014 (1993).

1.13 A. Lovas, L. F. Kiss, Varga, P. Kamasa, I. Balong, I. Bakonyi; J. Phys.1V. J. Inst. Met. France (1998) **8** 291.

1.14 Saroaut Noor, S. S. Sikder, D. K. Saha and M. A. Hakim; "Time and temperature Dependence of Nanocrystalline and Initial permeability of finemet alloy", Nuclear Science and Applications, June (2006) **15 No.1** 9-13.

1.15 G. Herzer, "Grain Structure and Magnetism of Nanocrystalline Ferromagnets", IEEE Trans. Magn. (1989) **MAG-25** 3327.

1.16 Le Minh, Bach Thanh Cong, Tran Quoc and Nguyen Chau; Proceeding of the 2nd International Workshop on Materials Science (IWOMS' 95), Hanoi, Oct. (1995).

1.17 E. Estevez Rams, J. Fidler, M. Dahlgren, R. Grossinger, M. Knobel, P. Tiberto, P. Alia and F. Vinal; J. Phys. D; Appl. Phys. (1996) **29** 848-854.

1.18 Y. Yoshizawa, K. Yamauchi, T. Yamane, H. Sugihara, J. Appl. Phys. (1988) **64** 647.

1.19 Saroaut Noor, M. Phil Thesis, Department of Physics, KUET, Khulna, March-2005.

1.20 Y. Yoshizawa and K. Yamachi, "Fe-based soft magnetic alloys composed of ultrafine grain structure", Mater. Trans. JIM. (1990a) **31** 307.

1.21 T. H. Noh, M. B. Lee, H. J. Kim, I. K. Kang, "Reletionship between crystallization process and magnetic properties of Fe-(Cu-Nb)-Si-B amorphous alloys", J. Appl. Phys. (1990) **67** 5568.

1.22 Y. Yoshizawa and K. Yamachi, "Magnetic properties of Fe-Cu-M-Si-B (M = Cr, V, Mo, Nb, Ta, W) alloy", Mater. Sci. Eng. A (1991b) **133** 176.

1.23 M. Muller. and N. Mattern, "The influence of refractory element additions on the magnetic properties and on the crystallization behavior of nanocrystalline soft magnetic Fe-B-Si-Cu alloys", J. Magn. Magn. Mater (1994) **136** 79.

1.24 P. K. Roy, M. Phil Thesis, Department of Physics, KUET, Khulna, May-2007.

1.25 J. D. Ayers, V. G. Harris, J. A. Sprague, W. T. Elan, "On the role of Cu and Nb in the formation of nanocrystals in amorphous $Fe_{73.5}Nb_3Cu_1Si_{13.5}B_9$", Appl. Phys. Lett. (1994) **64** 974.

1.26 G. Herzer, Hand Book of Magn. Mater., (1997) **10** 427.

1.27 O. Kubaschewski, Iron-Binary Phase Diagrams (Springer-Verlag, Berlin, Heidelberg, New York) (1982).

1.28 M. A. Hakim and S. Manjura Hoque; "Effect of structural parameters on soft magnetic properties of two phase nanocrystalline alloy of $Fe_{73.5}Cu_1Ta_3Si_{13.5}B_9$", J. Magn. Magn. Mater. (2004) **284** 395-402.

1.29 S. Manjura Hoque and M. A. Hakim; "Ultra-Soft magnetic properties of devitrified $Fe_{75.5}Cu_{0.6}Nb_{2.4}Si_{13}B_{8.5}$", J. Materials Chemistry and Physics, (2007) **101** 112-117.

1.30 A. Lovas, L. F. Kiss, I. Balong , "Saturation magnetization and amorphous Curie point changes during the early stage of amorphous-nanocrystalline transformation of a FINEMET-type alloy", J. Magn. Magn. Mater. (2000) **215-216** 463.

1.31 A. E. Berkowitz, J. L. Walter, K. F. Wall, "Magnetic Properties of amorphous particles produced by Spark Erosion", Phys. Rev. Lett. (1981) **46** 1484.

1.32 N. Chau, P. Q. Thanh, N. Q. Hoa and N. D. The, "The existence of giant magnetocaloric effect and laminar structure in $Fe_{73.5-x} Cr_x Si_{13.5} B_9 Nb_3 Cu_1$", J. Magn. Magn. Mater. (2006) **304** 36-40.

1.33 Md. Sultan Mahmud, Ph. D. Thesis, Department of Physics, KUET, Khulna, April-2008.

Chapter-II

2.1 Z. Turgut, M. Q. Huang, K. Gallagher, S. A. Mayelich and M. E. Mc Henry; J. Appl. Phys. (1997) **81** 4039.

2.2 Z. Turgut, N. T. Nuhfer, H. R. Pichler and M. E. Mc Henry, J. Appl. Phys., (1999) **85** 4406.

2.3 F. W. A. Dirne and M. Brouha, IEEE Trans. Magn., (1988) **MAG-24** 1862.

2.4 H. J. de Wit, J. Magn. Magn. Mat., (1989) **79** 167.

2.5 Y. Yoshizawa, K. Yamauchi, T. Yamane, H. Sugihara, J. Appl. Phys. (1988) **64** 647.

2.6 P. Duwez, R. H. Willens and W. Klement; J. Appl. Phys., (1960) **31** 1136.

2.7 A. W. Simpson and D. R. Brandley; Phys. Stat. Sol. (b) (1971) **43** 291.

2.8 R.C. O' Handley, J. Megusar, S. W. Sun, Y. Hara, N. J. Grant; J. Appl. Phys. (1985) **57** 3563.

2.9 P. Duwez, J. Am Inst. Metal Eng. (1951) **191** 765.

2.10 P. Duwez, R. H. Willens, W. Klement; J. Appl. Phys., (1960) **31** 1136.

2.11 P. Duwez, Trans. Am SOC Met. (1967) **60** 607.

2.12 P. Duwez, Ann Rev. Mat. Sci. (1976) **6** 83.

2.13 S. Mader, Nowick As. Appl. Phys. Lett. (1965) **7** 57.

2.14 C. C. Tsuei, P. Duwez, J. Appl. Phys., (1960) **37** 435.

2.15 Y. Yoshizawa, S. Oguma and K. Yamauchi, J. Appl. Phys. (1988) **64** 6044.

2.16 Y. Yoshizawa, K. Yamauchi, T. Yamane and H. Sugihara, J. Appl. Phys. (1988) **64** 6047.

2.17 A. Kojima, H. Horikiri, Y. Kamamura, A. Makino, A. Inoue, T. Matsumoto; Mat. Sci. Eng. (1994) **A179/A180** 511.

2.18 T. Mizoguchi, IBM Research report, (1976) **RC 6054**.

2.19 R. Alben, J. I. Budnic and G. S. Gargill; α_{111} Metallic Glasses, "American SOC. for metals" (1978) **PP.304**.

2.20 Y. Yoshizawa and K.Yamauchi, "Fe-based soft magnetic alloys Composed of ultrafine grain structure", Mater. Trans. JIM. (1990a) **31** 307.

2.21 K. Hono and T. Sakuria, "Atom probe studies of nanostructured alloys", Appl. Surf. Sci. (1995) **87/88** 166.

2.22 K. Hono, K. Hiraga, Q. Wang, A. Inoue, T. Sakurai, "The Microstructure Evolution of $Fe_{73.5}$ $Si_{13.5}$ B_9Nb_3 Cu_1 nanocrystalline soft magnetic material", Acta Metal. Mater. (1992) **40** 2137.

2.23 U. Koster, M.. Schoncmann, Blank-Bewersdorff, S. Brauer, M. Sutton and G. B. stephemon; Mat. Sci. Eng. (1991) **A133** 611.

2.24 H. Warliment, Mater. Sci. Eng. (1988) 99.

2.25 G. Herzer; In: Proc of Int. Symp. On 3ab Transition- Semi Metal Thin Flimss. Magnetism and Processing (Japan SOC for the promotion of Science, Committee, Sendia, Japan) (1991) **131** 130.

2.26 A. Makino, A. Inoue, T. Masumoto, Mat. Trans. JIM (1995) **36** 924.

Chapter-III

3.1 Turnbull, IEEE Trans. Magn. (1990) **26** 1397-1402,

3.2 JMD. Coey and H. Sun, J. Magn. Magn. Mater. (1991) **87** L251.

3.3 K. Schnitzke, L. Schultz, J. Wecker and M. Katter; Appl. Phys. Lett., (1990) **57** 2853.

Chapter-IV

4.1 D. Turnbull, Contemp. Phys. (1969) **10** 473.

4.2 W. L. Johnson, Progress in materials science, (1986) **30** PP. 81-134.

4.3 D. Louca, K. Ahn, V. Ponnambalam and S. J. Poon; Mat. Res. SOC. Proc. Vol. 754, PP. CC 7.7.1-CC 7.7.6. (2003).

4.4 J. W. Martin, R. D. Doherty, B. Canter, "Stability of microstructure in metallic systems" Cambridge, UK (1997).

4.5 W. Kauzmann, Chem. Rev., (1948) **43** PP. 219-256.

4.6 The IUPAC Compendium of Chemical Terminology, (1997) **66** 583.

4.7 H. Jones, Rep. Prog. Phys., (1973) **36** 1425.

4.8 D. Turnbull, J. dc physique, (1974) **35** C4-1.

4.9 S. Takayama, J. Materials Sci., (1976) **11** 164.

4.10 J. T. S. Irvine, E. Amano, A. Huanosta, R. Valenzuela, A. R. West; "Solid State should peak at T_c" Ionic (1990) **40/41** 220.

4.11 M. H. Cohen and D. Turnbull; Nature, (1961) **189** 131.

4.12 G. Gargil, III; J. Appl. Phys. (1970) **41** 2248.

4.13 H. S. Chen, Acta Met. (1974) **22** 1505.

4.14 S. R. Nagel and J. Taue, "Nearly-Free-Electron Approach to the Theory of Metallic Glass Alloys" Phys. Rev. Lett. (1975) **35** 380.

4.15 A. E. Berkowitz, J. L. Walter, K. F. Wall, " Magnetic Properties of amorphous particles produced by Spark Erosion" Phys. Rev. Lett. (1981) **46** 1484.

4.16 B. D. Culity, "Elements of X-ray diffraction" Reading, M. A; Addisonwesley, (1978).

4.17 G. Herzer, "Grain Size Dependence of Coercivity and Permeability of Nanocrystalline ferromagnets" IEEE Trans, Magn. (1990) **MAG-26** 1397.

4.18 R. Alben, J. J. Becker, M. C. Chi., "Random Anisotropy in Amorphous Ferromagnets" J. Appl. Phy. (1978) **49** 1653-1658.

4.19 G. Bertotti, E. Ferrara, F. Fiorillo, P. Tiberto; Mat. Sci. Eng. (1997) **A, 226-228** 603.

4.20 JMD Coey, Rare-earth iron permanent magnets. Oxford; Oxford Science Publications, Clearendon Press, (1996).

4.21 G. Herzer, "Nanocrystalline Soft Magnetic Materials" J. Magn. Magn. Mater. (1996) **157/158** 133.

4.22 A. Hernando, M. Vazquez, T. Kulik and C. Prados, "Analysis of the dependence of Spin-Spin correlations on the thermal treatment of nanocrystalline materials" Phys. Rev. B (1995) **51** 3581.

4.23 R. Grossinger, D. Holzer, C. Ksshach, H. Sassik, R. Stao Turtelli, J. P. Sinnecker, E. Witting, J. Magan. Magan. Mater. in press.

4.24 A. Hernando, T. Kulik, "Exchange interactions through amorphous paramagnetic layers in ferromagnetic nanocrystals" Phys. Rev. B (1994) **49** 7064.

4.25 R. Harris, M. Plisehke, M. J. Zuckorman, "New Model for Amorphous Magnetism" Phys. Rev. Lett. (1973) **31** 160.

4.26 R. Bozorth, Ferromagnetism (D. Van Nostrand, Princeton N. J.) (1951) **76**.

4.27 J. S. Kouvel, In: Berkowitz E, Kneller E, editors. Magnetism and Metallurgy; New York, Academic Press, (1969) **Vol. 2A** 523.

4.28 K. Handrich, "Conditions for the Existence of Amorphous Ferromagnets" Phys. Stat. Sol.(b) (1972) **53** k17.

Chapter-V

5.1 H. Le. Chatelier; Bull SOC. France. Mineral, (1887) **10** 204.

5.2 W. B. Pearson, "A Hand book of Lattice spacing and Structures of Metals and Alloys" (Oxford Pergamon) (1958).

5.3   A. Arrott, "Criterion for Ferromagnetism from Observations of Magnetic Isotherms" Phys. Rev. (1957) **108** 1394.

5.4   K. P. Belov, Magnetic transition, Consultants Bureau (New York) (1961)

5.5   J. S. Kouvel and M. E. Fisher, "Detailed Magnetic Behavior of Nickel near its Curie point" Phys. Rev. (1964) **136** A1626.

5.6   S. Foner, Rev. Sci. Instr. (1959) **30** 548.

5.7   S. Foner, Rev. Sci. Instr. (1955) **27** 578.

Chapter-VI

6.1   W. G. Clements and B. Cantor, 1976, in Rapidly quenched metals, Section-1, (eds. N. J. Graut and B. C. Giessen) (MIT Press Cambridge, Mass) P. 267.

6.2   F. E. Luborsky, Materials Sci. Engg-28 (1977), P. 139.

6.3   C. L. Chen and R. S. Hasegawa, ibid (1978) **49** 1721.

6.4   K. Moorjani, S. K. Chatak, K. V. Rao, B. Kramer, H. S. Chen, Int. Conf. on Liquid and amorphous Metals, Grenomle, France (1980).

6.5   G. Herzer, Elsevier hand book of magnetic materials (1997) **10** 427.

6.6   G. Herzer, and H. Warlimont, Nanostructured Mat. (1992) **1** 263.

6.7   K. Hono, A-Inoue, T. Sakurai, Appl. Phys. Lett. (1991) **58** 2180.

6.8   R. M. Bozoroth, Ferromagnetism, D. Van Nostrand Company, Inc., Princeton, NJ, (1964) 74.

6.9   M. Rubinstein, V. G. Harris, P. Lubitz, "Ferromagnetic resonance in nanocrystalline $Fe_{73.5}$ Cu_1 Nb_3 $Si_{13.5}$ B_9 (Finemet)" J. Magn. Magn. Mater.(2001) **234** 306.

6.10   F. E. Luborsky, J. J. Decker and R. O. Mc Cary; IEEE Trans. Mag. (1975) **11** 1644.

6.11   M. Z. Kersten; Angew. Phys. (1956) **7** 313.

6.12   A. Olszewski, J. Zbroszczyk, J. Olszewski, W. H. Ciurzynka, H. Fukunaga, K. Narita, B. Wyslockc, M. Hasiak, "Magnetic softening of nanocrystallineFe_{74} Cu_1 Nb_3 $Si_{12}B_{10}$ alloy obtained by two-step heat treatment" J. Magn. Magn. Mater (2000) **215-216** 422.

6.13 V. Franco, C. F. Conde, A. Conde; "Changes in magnetic anisotropy distribution during structural evolution of Fe_{76} $Si_{10.5}$ $B_{9.5}$ Cu_1 Nb_3" J. Magn. Magn. Mater. (1998) **185** 353-359.

6.14 I. Skorvanek, J. Kovac, J. Kotzler, Phys. Stat. Solidi (b) 236, 303-309 (2003).

6.15 I. Skorvanek, J. Kovac, J. M. Greneche, J. Phys. Condens. Mater. (2000) **12** 9085.

6.16 L. K. Varga, K. V. Rao, Nanostructured Materials., (1999) **12** 1157-1160.

6.17 G. Herzer; "Handbook of Magnetic Materials" Vol. 10, ed. K. H. J. Buschow (Elsevier Science B. V.) (1997) 417.

6.18 G. R. Aranda, J. Gonzalez, K. Kulakowski, J. Appl. Phys. (1998) **83** 6341.

.6.19 A. Lovas, L. F. Kiss, I. Balong, "Saturation magnetization and amorphous Curie point changes during the early stage of amorphous- nanocrystalline transformation of a FINEMET-type alloy" J. Magn. Magn. Mater. (2000) **215-216**, 463.

6.20 A. E. Berkowitz, J. L. Walter & K. F. Wall, "Magnetic properties of amorphous particles produced by Spark Frosion" Phys. Rev. Lett. (1981) **46** 1484.

List of Conference Papers attended by the author:

1. S. K. Nath, **Siba Pada Mondal**, S. S. Sikder, S. Manjura Hoque & M. A. Hakim "Influence of Sintering Temperature on Initial Permeability of $Ni_{1-x}Cd_xFe_2O_4$ Ferrites" National Conference cum Workshop on Materials Science & Technology, held on 2-4 December 2007, BUET, Dhaka, Bangladesh.

2. S. S. Sikder, M. Mahbubur Rahman, **Siba Pada Mondal**, S. Manjura Hoque & M. A. Hakim "Influence of SiO_2 and CaO addition on the Microstructure and Hysteresis parameters of Sr-Haxaferrites using Magnetite from Cox's Bazar Beach Sand in Bangladesh" Abstract accepted for the coming Annual Conference of Bangladesh Physical Society (BPS).

3. **Siba Pada Mondal**, S. S. Sikder, M. A. Hakim & D. K. Saha "Influence of annealing conditions on Nanocrystalline and Ultra soft magnetic properties in $Fe_{75.5}Cu_1Nb_1Si_{13.5}B_9$ alloy" Abstract accepted for the coming Annual Conference of Bangladesh Physical Society (BPS).